Generation and Detection of Low-Frequency Squeezing for Gravitational-Wave Detection

Michael Steve Stefszky

A thesis submitted for the degree of
doctor of philosophy of
The Australian National University

April 2012

Declaration

This thesis is an account of research undertaken between March 2008 and April 2012 at The Department of Physics, Faculty of Science, The Australian National University, Canberra, Australia.

Except where acknowledged in the customary manner, the material presented in this thesis is, to the best of my knowledge, original and has not been submitted in whole or part for a degree in any university.

Michael S. Stefszky
April, 2012

Acknowledgements

The last four years of my life have been amazing and I would like to thank (hopefully) everyone who has contributed and supported me over this time.

These years have been made fruitful and enjoyable by the support of an outstanding supervisory panel. For this, I would like to first give my sincerest thanks to Professor Ping Koy Lam, Doctor Ben Buchler and Doctor Thomas Symul from the Quantum Optics Group (now CQC2T), and Professor David McClelland and Doctor Daniel Shaddock from the Centre for Gravitational Physics.

The foremost thanks has to go to Ping Koy Lam, whom I have studied with for many years now. Much appreciation is given for my acceptance into the quantum optics group many years ago, first for my honours year and then for my PhD. The foresight and sense of direction that Ping Koy has showed over the years, both in individual experiments and for the entire group, has been, and continues to be, invaluable. I am very grateful for the opportunities I have had to travel both locally and overseas for conferences and collaborations. Ping Koy's outstanding abilities as a group leader have been made apparent to me many times and his enthusiasm for his work is very addictive.

My decision to work on the H1 LIGO squeezer project later into my PhD I can now look back and say was most certainly the correct one. For this opportunity I have firstly to thank David. Working on this project meant many things. It meant the support of a second research group, the Centre for Gravitational Physics, the opportunity to collaborate with many institutions and people on a truly international project, and the learning advantages from working in a new group with its own areas of expertise. Working on this project allowed me to work at MIT for nearly 6 months and at LIGO for nearly 3. The experience gained from these travels makes up a large portion of what I consider to be the most valuable training from my studies and for this opportunity I need to thank David. Additionally, David always found time in a busy schedule to help with experimental problems and provide direction when needed.

Sincerest thanks then goes to Ben and Daniel. Together with Ping Koy and David, I cannot imagine a better group of people to have available when a problem arose. Although by no means the limit of their knowledge, Daniel's expertise in electronics and locking loops, combined with Ben's expertise in just about anything related to optics, particularly non-linear optics, meant that solutions to any problem were quickly found. The willingness to help combined with the knowledge and good humour of both Daniel and Ben was both invaluable and greatly appreciated.

Onto my two lab mates, Sheon Chua and Conor Mow-Lowry. If it were not so much fun to work in the lab as it was, then I am sure things would not have progressed as far as they did. The environment in the lab was a relaxed one, where input from each person was valued, and I really appreciate the synergy we had going. Conor's knowledge ensured that progress was smooth and constantly provided alternative solutions to problems that arose. Sheon's problem solving techniques were different to mine and so together we attacked problems from many different angles.

From the ANU still, I need to thank the electronics and mechanical workshops, Shane

Grieves, Neil Hinchey, James Dickson, Paul McNamara, Paul Tant and Neil Devlin. The work these people do is of the highest quality and without their help, I might still be milling steel and soldering circuits. Also to everyone from both the quantum optics group and all of the graviteers, as well as everyone else from the physics department. How enjoyable a particular job is depends on both the work one is doing and the people involved. The people in the physics department have have certainly made the last few years enjoyable. A quick mention to Nicolai Grosse for his aid, wisdom and friendship during my honours year. A big thanks also goes out to Phil Threlfall, Richard Barry, and especially Conor Mow-Lowry and Timothy Lam, who along with Ping Koy, David, Daniel and Ben, drafted various sections of this thesis.

To all the people in the United States, thank you. To Nergis Mavalvala, Daniel Sigg, Lisa Barsotti, Sheila Dwyer and the rest of the LIGO team, thank you very much for the opportunity to visit a new country and work in new places on exciting experiments. Thank you to Nergis and Daniel for allowing me to work at MIT and at LIGO, and thank you to Lisa for her excellent organisational skills in organising both human resources and experiments. Thanks to Sheila for making my stay in Boston as enjoyable as possible and to Dick Gustafson for introducing me to Cognac and ice-cream in Hanford.

Onto the friends and help that I have received from people at the Max Planck Institute for Gravitational Physics. Firstly, thank you to Roman Schnabel, Henning Vahlbruch and Alexander Khalaidovski and Moritz Mehmet. Thank you for the many discussions that were had on detector design, balanced homodyne detection and squeezed light production. Your willingness to share information and aid us in our experiment was invaluable. Thank you to all the people at Hannover who made my short stay there incredibly fun. So much fun that I hope to return to Hannover some time in the near future. Thank you to Moritz for showing me around your home country and institute. I hope I can return the favour soon.

Then there are my friends outside of work. My housemates and friends for many years, Neil, Mitch, Sam, and Jason as well as my friends whom I see the most often; Conor, Andrew, Kieran, Neil and Phil to name but a few. Thank you for providing distractions when I needed it, and sometimes when I did not, and for making my home environment a fun place to be. Thank you for trying to keep me fit with the many mountain bike rides we went on. The ability to unwind and relax after writing for hours on end is not an easy task sometimes but you guys made it easier.

Onto my family. Thank you to Mum, Dad, Michael and Angelina for your never ending support. Thank you to Warren, Tanya, Michael, and Anthony for keeping things real. Finally, the most heartfelt thank you to Jenessa, whose understanding and support has been nothing short of amazing.

Abstract

Gravitational-wave astronomy promises a radically new method of investigating the universe, one that does not detect elementary particles, but rather ripples in space-time itself. One might expect that with this radically new method, our understanding of the universe will make an equally giant leap. One of the most promising methods for the eventual detection of gravitational-waves is that of interferometric gravitational-wave detection.

The sensitivity of these devices is nothing short of amazing, and their sensitivity continues to improve. The next generation of detectors are expected reach a point where increasing the laser power, previously used to increase the sensitivity, is no longer expected to provide any benefit. One of the most promising options for further increasing the sensitivity, through reduction of the quantum noise, is via the application of "squeezed states of light". Squeezed states of light are light fields for which the noise of some observable has been reduced below the quantum noise limit. These states have been shown for many years to offer increased sensitivity in interferometers and recently in interferometric gravitational-wave detectors. One of the most challenging tasks to make suitable squeezed light sources for these detectors is to produce low-frequency squeezing, corresponding to the detection band of these interferometers.

This thesis details the doubly resonant travelling wave bow-tie squeezer as a source of squeezing for interferometric gravitational-wave detection. This squeezer achieves record results of squeezing in the gravitational-wave detection band. For the first time, 10 dB of shot noise suppression at 10 Hz is directly observed and above 200 Hz, 11.6 dB is observed. The work presented in this thesis provides evidence that further substantiates previous progress indicating that squeezed states of light are now ready for full-time integration into interferometric gravitational-wave detectors. The new cavity design, described in detail throughout this thesis, is shown to outperform previous designs and provide benefits when integrating squeezing into these detectors, in particular, isolation to backscattered light from the interferometer.

The noise sources that typically lead to degradation in squeezing measurements are investigated and discussed. Additionally, a modification to the standard locking technique used to control these vacuum squeezed states, *coherent locking*, is presented and discussed. The modified technique reduces the required number of locking loops and provides a larger beat note from which to derive an error signal for one of the remaining loops.

A squeezer using these design philosophies is then constructed and used to inject squeezing into the LIGO gravitational-wave detector. Injection of the squeezed state provides enhancement of the sensitivity of the detector at frequencies around 200 Hz and above. The sensitivity seen was equivalent to approximately 2 dB of shot noise reduction. The enhancement is limited by the loss within the interferometer. Injection of the squeezed state did not show any degradation in the sensitivity of the device below 200 Hz, indicating for the first time that noise couplings between the interferometer and the squeezer could be sufficiently suppressed at these frequencies even for the most sensitive detectors.

Contents

List of Figures

List of Tables

Summary of symbols and acronyms

Symbol	Definition
h_s	Interferometer strain
l	Interferometer arm length
$(\Delta Z)_{rp}$	Interferometer error due to radiation pressure
$(\Delta Z)_{pc}$	Interferometer error due to photon counting or shot noise
S_{Th}	Root power spectral density due to thermal fluctuations on the test mass
M	Mass of interferometer test mass
I	Laser field intensity
i	Photocurrent
k	Optical mode
E	Energy
ω	Optical angular frequency or angular detection frequency
$h\,(\hbar)$	Planck's constant & (reduced Planck's constant)
c	Speed of light in vacuum
b	Bounce number
τ_s	Storage time
τ_m	Measurement time
P	Optical power
$\vec{k}$	Wavevector
Δk	Wavevector mismatch
L_C	Coherence Length
$w(z)$	Beam radius at position z
$w(0)$	Beam waist
z_R	Rayleigh Range
q	Complex beam parameter
M	ABCD Matrix
d	Physical distance
d_{eff}	Crystal Non-linear susceptibility strength
$\hat{n}$	Photon number operator
ϕ	State phase angle
$\hat{D}(\alpha)$	Displacement operator
$\hat{S}(\rho)$	Squeezing operator
r	Squeezing parameter
MM	Mode matching
η_{vis}	Efficiency of spatial overlap from visibility measure

Symbol	Definition
$\hat{a}, (\hat{a}^\dagger)$	Annihilation & (creation) operators of intra-cavity mode
$\hat{A}, (\hat{A}^\dagger)$	Annihilation & (creation) operators of travelling wave
$\check{A}$	Frequency domain annihilation operator of travelling wave
$a_3^{crit}, (A_3^{crit})$	Intra-cavity & (external) field threshold amplitude
P_3^{crit}	External field threshold power
$\delta\hat{a}, (\delta\hat{a})$	First order fluctuating term of annihilation & (creation) operators
$\hat{X}^+, (\hat{X}^-)$	Amplitude & (phase) quadrature operators
$\delta\hat{X}^+, (\delta\hat{X}^-)$	First order fluctuation term of amplitude & (phase) quadrature operators
$\hat{X}^\theta$	General quadrature operator
$\Delta\hat{G}$	Standard deviation of observable $\hat{G}$
$V(\hat{G}) \equiv \Delta^2(\hat{G})$	Variance of the observable $\hat{G}$
α	Classical coherent amplitude
η	Beamsplitter power transmissivity or propagation efficiency
η_{esc}	Escape Efficiency
τ	Cavity round-trip time
δ	Frequency offset
L	Cavity optical path length
κ	Cavity decay rate
$R, (T)$	Power Reflectivity & (Transmittance)
Δ	Cavity detuning
g	Intra-cavity non-linear coupling strength
G	Combined non-linear coupling strength and intra-cavity pump amplitude
λ	Optical field wavelength
n	Refractive index
$\mathcal{V}$	Visibility
$\chi^{(2)}$	Second order non-linear susceptibility
$\mathcal{F}$	Finesse
Δ_ν	Cavity linewidth
$1, 2, 3$	Defines parameters for signal, idler and pump fields, respectively

Acronym	Definition
aLIGO	advanced LIGO
ANU	The Australian National University
AR	Anti-Reflection
AURIGA	Ultracryogenic Antenna for Astronomical Gravitational Investigation
CLL	Coherent Locking Loop
CMRR	Common-Mode Rejection Ratio
CSF	Coherent Sideband Field
DOPA	Degenerate Optical Parametric Amplifier
EOM	Electro-Optic Modulator
EPR	Einstein-Podolsky-Rosen
ETX500	Epitaxx 500 photodiode
FFT	Fast Fourier Transform
FSR	Free Spectral Range
FWHM	Full-Width-at-Half-Maximum
GEO600	British-German Cooperation for Gravity Wave Experiment
GRIIRA	Green Induced Infra-Red Absorption
GSF	Generated Sideband Field
GW	Gravitational-Wave
GWINC	Gravitational-Wave Interferometer Noise Calculator
H1	4km arm length interferometer at enhanced LIGO Hanford site
H2	2km arm length interferometer at enhanced LIGO Hanford site
HD	Homodyne
HR	High Reflectivity
KAGRA	Kamioka Gravitational Wave Detector
KNB	Potassium Niobate
KTP	Potassium Titanyl Phosphate
LIGO	Laser Interferometer Gravitational-wave Observatory
LN	Lithium Niobate
LSC	LIGO Scientific Collaboration
MC	Modecleaner Cavity
MgO:LN	Magnesium Oxide doped Lithium Niobate
MIT	Massachusettes Institute of Technology
MZ	Mach-Zender
NDOPA	Non-Degenerate Parametric Amplifier
Nd:YAG	Neodymium doped Yttrium Aluminium Garnet
NGO	New Gravitational-wave Observatory
OPA	Degenerate Optical Parametric Amplifier
OPO	Optical Parametric Oscillator
PDH	Pound-Drever-Hall Locking Technique
PPKTP	Periodically Poled Potassium Titanyl Phosphate
PZT	Lead Zirconate-Titanate piezo/electric ceramic
RBW	Resolution BandWidth
RMS	Root Mean Square
RoC	Radius of Curvature
RP	Radiation Pressure
SHG	Second Harmonic Generation
SN	Shot Noise
TEM	Transverse Electro-Magnetic
VIRGO	Italian-French Laser Interferometer Collaboration

Chapter 1

Introduction

Our understanding of the universe around us, from subatomic particles to the vast cosmos, shapes the way we live our lives. As precision measurements improve and we unravel more about how the world works, we are constantly transforming society in ways that are nearly impossible to predict. A perfect example is that of light amplification by stimulated emission of radiation, or the laser [1]. In a mere fifty years, the laser has become a building block of modern society. From entertainment, to beauty treatments, to surgery and probing of the fundamental laws of our universe, the usefulness of lasers has shaped the way our modern world works [2]. Our understanding of things on the opposite side of the size-scale have arguably had just as large an impact. Many years ago, astronomy led to the realisation that the earth is indeed round and not the centre of the universe, contrary to prior beliefs. This type of knowledge impacts significantly on theological ideas and in turn, on society itself.

Arguably, the advent of the telescope was the catalyst for the evolution of astronomy as a modern science. Early in the 17^{th} century, Galileo was the first to utilise their potential in observing details of the surface of the moon and the motions of the planets and the stars. Whilst telescopes evolved, becoming larger and providing more precise images, all early telescopes were restricted by the same fundamental limitation. Detections were made with the user's eye, and thus the information gathered was limited to the visible spectrum of light. Visible light, however, is a very small portion of the electromagnetic spectrum. Astronomy progressed, and the advantages obtained by widening the detection band were revealed. In the 1800's infra-red radiation was discovered by Herschel and was later used to study properties of the moon [3]. The detection band has continued to increase over time, such that we now routinely observe many orders of wavelengths of electromagnetic radiation, from gamma rays to radio waves [4, 5]. However, these forms of astronomy are all founded upon a common principle, the detection of electromagnetic waves. As such they all share similar advantages, and of course, similar disadvantages. Their detection can be hampered by various complications; they are prone to absorption, and follow the local space-time trajectory. One example of particular importance is that this means that direct detections of black holes cannot be made using electromagnetic observations. For many of the most violent, massive and arguably interesting phenomenon, another measurement method is required to complement the often limited information that electromagnetic waves can provide.

This is the role that gravitational-wave detection is hoped to fulfil in the near future. This thesis presents work that aims to improve the sensitivity of current interferometric gravitational-wave detectors via the integration of squeezed optical states. With the enhanced sensitivity that squeezed states are to offer, along with other improvements to current detector designs, we are nearing the era of gravitational-wave astronomy.

1.1 Thesis Structure

The thesis is structured as follows;

- Chapter 2 - Background

  The exciting realm of ground based gravitational-wave astronomy is introduced. Noise sources in current and next generation detectors are detailed and in particular the role of quantum noise sources is highlighted. Methods for reducing quantum noise are discussed and optical squeezing is introduced as an exciting new method of reducing the quantum noise in future detector designs.

- Chapter 3 - Quantum States of Light

  The mathematical description of the states of light used in this work is presented in this chapter. The ball-on-stick representation and the sideband representation for visualising the states of light are detailed. Using these representations, the properties of squeezed states, vacuum states, and coherent states are all introduced.

- Chapter 4 - Generation of Squeezed States

  In this chapter the generation of squeezed states is introduced. The various methods available are first discussed before detailing the production of squeezing from the second order non-linearity. Second harmonic generation, non-degenerate optical parametric amplification and optical parametric oscillation are introduced as modes of operation for the second order non-linearity.

- Chapter 5 - Optical Cavities

  The properties of optical cavities are introduced in this chapter. The cavity equations of motion are first introduced and then used to derive the classical and quantum response of an empty cavity. The finesse, free spectral range, linewidth and circulating power are defined. The cavity equations of motion are then investigated for an optical cavity containing a non-linear medium. From this work, the escape efficiency, non-linear gain, and expected squeezing from such a cavity are investigated.

- Chapter 6 - The Doubly Resonant Bow-Tie Optical Parametric Oscillator

  The methods and philosophies for designing a travelling wave cavity cavity are detailed in this chapter. The available non-linear mediums, techniques for overcoming intra-cavity dispersion and the choices involved when deciding all remaining parameters are discussed. The effect that variation of the cavity parameters has is illustrated.

- Chapter 7 - The ANU Squeezer

  The details of the ANU squeezer are given in this chapter. All of the chosen cavity parameters are stated before the methods for accurately measuring threshold and intra-cavity loss are introduced. A layout of the optical and electronic components is given. The coherent locking scheme used to control the angle of the squeezed state is investigated and a modified coherent locking scheme is introduced as a means for simplifying and improving the original scheme. This work was jointly undertaken with Sheon Chua and Conor Mow-Lowry at the ANU under the supervision of David McClelland, Ping Koy Lam, Ben Buchler and Daniel Shaddock, with much appreciated input from Kirk McKenzie and which utilised a cavity design originally devised by Nicolai Grosse. Improvements to the squeezer were also made by Sheila Dwyer, who was involved for a number of months on the project. The later measurements of the squeezing produced by this squeezer were taken using a homodyne detector supplied by Roman Schnabel and Henning Vahlbruch.

- Chapter 8 - Detection of Squeezed States

  This chapter details an investigation into understanding the low-frequency performance of the homodyne detector setup used to measure the squeezed states. Many noise sources are investigated and methods for detecting and overcoming these noise sources are presented. The homodyne detector supplied by Roman Schnabel and Henning Vahlbruch plays a large role in this work. A short history of the squeezing produced by the ANU squeezer illustrates the various improvements made in order to improve the squeezing over a timespan of nearly 3 years. The work on detecting low-frequency noise sources as presented in this chapter was primarily undertaken with Conor Mow-Lowry, with some input from Sheon Chua, and the modified coherent locking scheme was devised by Conor-Mow Lowry and Kirk McKenzie. The modified coherent locking scheme was implemented by Sheon Chua.

- Chapter 9 - The LIGO Injection

  In this chapter the details of the LIGO squeezed light source are introduced. The cavity properties, including threshold and intra-cavity loss are given. The squeezing produced by the LIGO cavity is presented and the results are discussed. The integration of the squeezer into LIGO is briefly discussed but greater detail pertaining to the integration of the squeezer will be presented in the PhD theses of Sheon Chua and Sheila Dwyer as well as future papers. The squeezer was constructed and tested by myself, Sheon Chua, Conor Mow-Lowry, Alexander Khalaidovski and Sheila Dwyer at MIT. The LIGO squeezed light injection project was a large collaborative project, with too many people involved to mention them all, but particular mention is made to Nergis Mavalvala, Daniel Sigg, Keita Kawabe, Sheila Dwyer and Lisa Barsotti, who I worked most closely with during my time on this project. A number of months were personally spent aiding in the integration of the squeezer with the LIGO detector.

- Chapter 10 - Conclusions and Further Work

  The conclusions from the work presented in this thesis are summarised. The future work on integration of squeezed light into interferometric gravitational-wave detectors that needs to be undertaken, in light of the work presented in this thesis, is then discussed.

1.2 Publications

- M. Stefszky, C. Mow-Lowry, K. McKenzie, S. Chua, B. Buchler, T. Symul, D. McClelland and P. K. Lam, "An investigation of doubly-resonant optical parametric oscillators and nonlinear crystals for squeezing," J. Phys. B: At. Mol. Opt Phys. **44**, (2011).

- M. S. Stefszky, C. M. Mow-Lowry, S. S. Y. Chua, D. A. Shaddock, B. C. Buchler, H. Vahlbruch, A. Khalaidovski, R. Schnabel, P. K. Lam, and D. E. McClelland, "Balanced Homodyne Detection of Optical Quantum States at Audio-Band Frequencies and Below," Clas. Quantum Grav. (submitted), (2012).

- S. Chua, M. Stefszky, C. Mow-Lowry, B. Buchler, S. Dwyer, D. Shaddock, P. Lam, and D. McClelland, "Backscatter tolerant squeezed light source for advanced gravitational-wave detectors," Opt. Lett. **36**, 4680 (2011).
- The LIGO Scientific Collaboration, "A gravitational wave observatory operating beyond the quantum shot-noise limit," Nat. Phys. **2083**, DOI:10.1038 (2011).
- The LIGO Scientific Collaboration, "Implementation and testing of the first prompt search for gravitational wave transients with electromagnetic counterparts," ArXiv:1109.3498v2 (2011).
- The LIGO Scientific Collaboration, "Search for Gravitational Wave Bursts from Six Magnetars," Astrophys. J. **734**, (2011).
- The LIGO Scientific Collaboration, "Beating the Spin-Down Limit on Gravitational Wave Emission from the Vela Pulsar," Astrophys. J. **737**, (2011).
- S. Chua, M. Stefszky, C. M. Mow-Lowry, B. C. Buchler, K. McKenzie, D. A. Shaddock, P. K. Lam, and D. E. McClelland, "Quantum Squeezing in Advanced Gravitational Wave Detectors" IJMPD **20**, 2043 (2011).
- The LIGO Scientific Collaboration, "Enhancement of the astrophysical reach of a gravitational wave observatory using squeezed states of light," Unpublished Manuscript.

Chapter 2

Background

In this chapter, gravitational-waves are introduced. The properties of gravitational waves are briefly discussed and two methods for their detection, resonant bar detectors and interferometric detectors, are detailed. The noise sources in interferometric detectors are then listed and squeezed light is introduced as a solution to reducing the quantum noise in interferometric detectors.

2.1 Gravitational-Waves

Since the advent of general relativity it is now common to consider the three space dimensions and one time dimension as part of a single manifold, known as space-time. It was postulated by Albert Einstein early in the 20^{th} century that accelerating masses should release energy in the form of gravitational-waves, or ripples in space-time [6, 7]. These gravitational-waves oscillate perpendicular to the direction of propagation and act to shrink space in one direction, whilst simultaneously expanding in the perpendicular direction, as shown in Figure 2.1. The magnitude of these oscillations is incredibly small. An extensive review of the various sources and the characteristics of these waves is given in [8, 9]. By the time these waves propagate from their original sources and reach the Earth, we might expect the largest gravitational-wave sources to have a strain amplitude, h_s, on the order of 10^{-20} [10], where strain is defined as the change in length, Δl, over the length, l, in question

$$h_s \equiv \frac{\Delta l}{l}. \tag{2.1}$$

Many searches have been made [11, 12, 13], but direct detection of gravitational-waves has yet to be achieved. However, strong evidence for their existence has been identified. The binary pulsar system PSR 1913+16 was observed for many decades by Russell Hulse and Joseph Taylor [14]. The point of closest approach between these two pulsars, the periastron, was seen to decrease over the measurement time of 30 years. The decrease seen agreed with the change in periastron predicted by Einstein's theory of general relativity with startling accuracy. The challenge now is to directly detect these waves and retrieve from them the information that they carry about the systems from which they originated, thus opening to door into gravitational-wave astronomy.

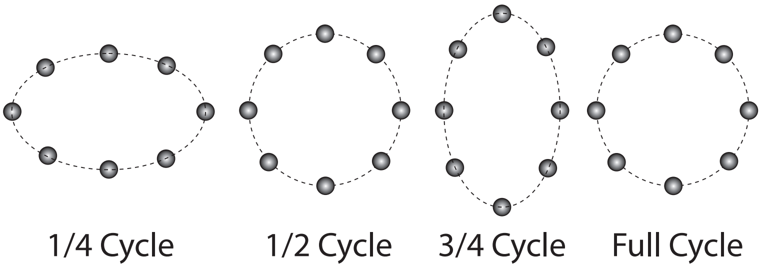

Figure 2.1: The effect of a gravitational-wave passing through a ring of free falling test masses. As the wave passes (into the paper), space-time is stretched along one axis and compressed in the orthogonal axis. This action oscillates at the frequency of the passing gravitational-wave.

2.2 Detecting Gravitational-Waves

The incredibly small amplitude of gravitational-waves makes their detection an overwhelmingly challenging task. When Albert Einstein first postulated their existence early in the 20^{th} century, there was conjecture, even from Einstein himself, as to whether these waves were mathematical artefacts or whether they would theoretically able to be detected [15]. However, it was not long before people were devising various methods that should, in theory, be capable of detecting the largest gravitational-waves here on Earth [16, 17].

2.2.1 Resonant Bar Detectors

Figure 2.2: AURIGA, cryogenically cooled resonant bar detector [18].

The first attempts at observing gravitational-waves were made by Joseph Weber in the 1960's [16]. Weber's design was that of a resonant bar. Resonant bars work on the principle that a gravitational-wave passing through it, with sufficient magnitude and the correct frequency, will excite a resonance mode within the bar. The resonance frequency of Weber's bar was tuned to a frequency of around 1660 Hz with a strain sensitivity of approximately $10^{-17}\frac{1}{\sqrt{Hz}}$ [19, 20]. The chance of detecting events with this detector was incredibly small, due to its very narrow bandwidth, of 10s of millihertz [19] and limited sensitivity. Even now, the sensitivity of resonant bar detectors is limited to strains of approximately $10^{-21}\frac{1}{\sqrt{Hz}}$, which is believed to be enough to detect only the strongest, and as such the rarest, of sources. Bandwidths of a few hertz are typical in current resonant bar detectors and up to a few kilohertz is attainable in resonant sphere systems, with resonance frequencies typically in the kilohertz region or above [21].

2.2.2 Interferometric Detectors

An alternative method of detecting these waves, proposed by Thorne, Drever and Weiss [22], began construction in 1992 [23], after many years of research into design choices and various noise sources [24, 25, 26]. This new class of detector would use a laser interferometer design to increase both sensitivity and bandwidth over resonant bar designs. The geometry was to resemble that of a typical Michelson interferometer with arm lengths of 4 km. The effect of a passing gravitational-wave on a Michelson interferometer is shown in Figure 2.3. This interferometer is incredibly sensitive to path length differences in the two arms and it is this property that would be used to detect gravitational-waves. The two end mirrors are suspended such that they act as free falling test masses. A gravitational-wave passing through the plane of the detector acts to increase the length of one arm by displacing one of the test masses, whilst decreasing the length in the other. An overview of interferometric gravitational-wave detector design is given in [27].

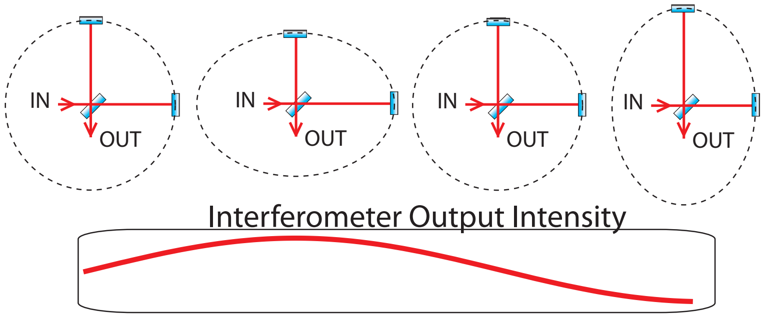

Figure 2.3: The effect of a passing gravitational-wave on a Michelson interferometer operating in the middle of an interference fringe. A gravitational-wave passing through the interferometer causes the length of the two arms to oscillate. This changes the relative phases of the laser fields from the two interferometer arms, 1 and 2, resulting in modulation of the intensity of the output field.

The detector shown in Figure 2.4, the Laser Interferometer Gravitational-wave Observatory (LIGO), is more sensitive and has a much larger bandwidth than current resonant bar detectors. LIGO's full detection band is from 10 Hz to 10 kHz, which is also known as the *audio detection band*. However, the the sensitivity of LIGO varies over this band. The device is currently undergoing upgrades but during its last science run, the device had a strain sensitivity of approximately $10^{-23}\frac{1}{\sqrt{Hz}}$ at around 100 Hz and greater than 10^{-22} from around 60 Hz up to approximately 1 kHz [28]. The device in this state was known as enhanced LIGO, further improvements are currently under way, with the next generation to be known as aLIGO [29]. Looking for gravitational wave sources at frequencies higher than these is not useful due to the fact that there is a limit as to how fast the massive bodies producing these waves can move. In LIGO's full detection band, the most promising source of gravitational-waves are the inspiral of massive bodies, such as black holes and neutron stars, as well as the burst signature from supernovae, gravitational radiation background and pulsars [10, 8]. A comprehensive overview of the properties of these sources and how their magnitudes relate to the various detectors is given by Schutz in [30] and the expected detection rates are presented in [31].

A network of detectors is necessary for both triangulation and increasing the confidence of events [10]. The device in Figure 2.4 is one of two 4 km interferometers situated in the United States. There is also a 3 km detector in Italy known as VIRGO [32] and another one in Germany with an arm length of 600 m known as GEO600 [33]. Together, these make up the current network (although not all are currently in operation) of interferometric gravitational-wave detectors.

Figure 2.4: The Laser Inteferometric Gravitational-wave Observatory (LIGO) in Livingston, Louisiana.

2.3 aLIGO Noise Sources

Interferometric gravitational-wave detectors are sensitive to noise sources that either directly change the position of one of the test masses or noise sources that mimic such a change. The aLIGO noise budget, as illustrated in Figure 2.5, shows that the expected major contributing noise factors below approximately 100 Hz are; thermal noise, seismic noise and quantum noise. At these frequencies, the quantum noise is dominated by radiation pressure noise. Above 100 Hz, the dominant quantum noise source is shot noise, resulting from photon counting error at the detector readout.

2.3.1 Low-frequency Noise Sources

Radiation Pressure Noise

It is expected in the next generation of interferometric gravitational-wave detectors that seismic and thermal noise will be so small in the region from around 10 Hz to 100 Hz that quantum noise will become the dominating source in this frequency regime. This is shown in Figure 2.5. The quantum noise source in this frequency band is known as *radiation pressure noise*. Photons reflecting off the end mirrors, or test masses, will impart

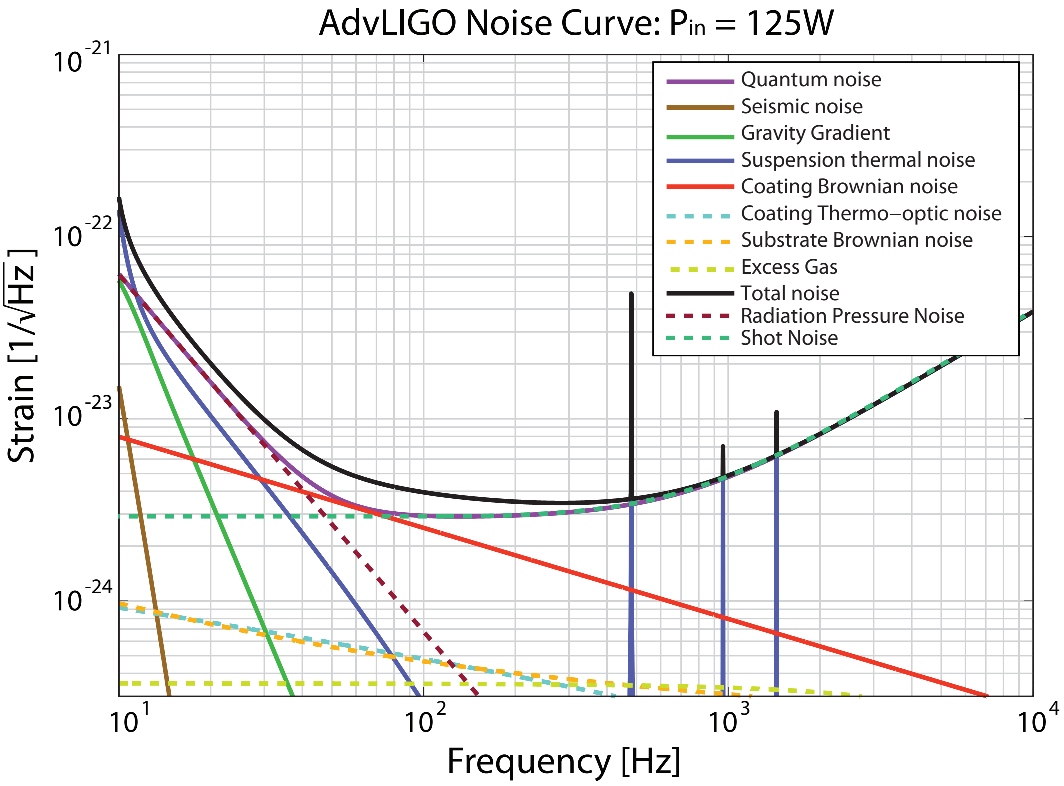

Figure 2.5: The expected aLIGO sensitivity. Plot produced using GWINC, developed by the LSC community.

a momentum kick to the mirror, conserving momentum in the collision. The momentum imparted is proportional to the number of photons, and hence proportional to the intensity of the incident field. If the intensity of the field were constant, then the constant stream of photons hitting the mirror would impart momentum that would simply alter the free resting position of the mirror. However, as the intensity of the field fluctuates, the position of the mirror will also fluctuate. If the intensity noise were classical, then the radiation pressure force felt by each test mass would be identical and this effect could be optically subtracted at the beamsplitter. However, due to the quantum mechanical nature of light, uncorrelated vacuum noise will be incident on each test mass. One can regard these fluctuations as vacuum fluctuations entering the empty input port of the interferometer beamsplitter [25], the same port where the interferometer output typically exits as in Figure 2.3. This uncorrelated noise cannot be subtracted and will be detected, masking the gravitational-wave signal. The radiation pressure error is written [34]

$$(\Delta Z)_{rp} \simeq \frac{b\hbar 2\pi f \tau_m}{mc} \left(\frac{P\tau_m}{\hbar 2\pi f} \right)^{\frac{1}{2}} e^r, \tag{2.2}$$

where $(\Delta Z)_{rp}$ is the radiation pressure error, or uncertainty due to radiation pressure, b is the number of bounces at each end mirror, τ_m is the measurement time, P is the optical power, f is the frequency of the laser light and $\hbar$ and c are the reduced Planck constant and speed of light respectively. The squeezing factor, r, introduced in detail in § 3.5.3, is a measure of the magnitude and angle of a squeezed state injected into the second input port of the beamsplitter of the interferometer. By convention, a positive squeezing factor implies the use of a phase squeezed state. Therefore, radiation pressure error is reduced through injection of an amplitude squeezed state, with a negative r value, into the second input port of the interferometer.

Radiation pressure noise is reduced by either decreasing the number of photons hitting the mirror, decreasing the velocity imparted to the mirror by each photon, or by directly reducing the uncorrelated noise. The number of photons can be reduced by decreasing the circulating power by varying the parameters P, τ_m and b, the velocity imparted to the mirror by individual photons is reduced by increasing the mirror mass, m, or reducing the energy of the photons, f. The uncorrelated quantum noise can be reduced via the introduction of an amplitude squeezed state. The effect of radiation pressure on a test mass is shown in Figure 2.6. In Figure 2.6, the case where no laser field is incident, i), shows the test mass hanging freely. In the case of the completely noiseless laser, ii), which cannot physically exist, the photons impart momentum to the mirror resulting in a constant force. In the final case, there is a quantum noise limited laser source, a so called coherent state, incident on the test mass. The incident laser field no longer has a constant intensity, but rather fluctuates, a direct consequence of Heisenberg's uncertainty principle. The varying intensity imparts a varying force and the position of the mirror fluctuates. The forces imparted to the test masses in the two arms are uncorrelated due to the vacuum noise entering the second input port of the interferometer, resulting in a noise source which cannot be subtracted.

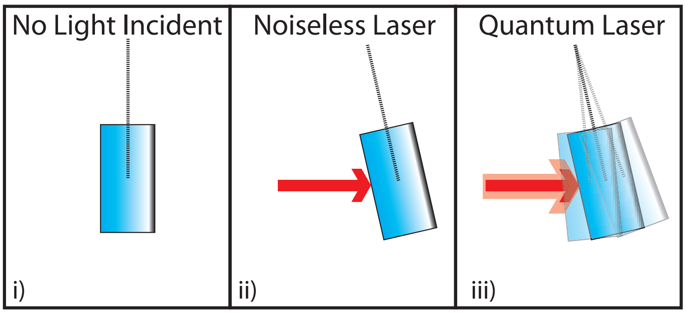

Figure 2.6: The effect of radiation pressure on a test mass for three cases: i) with no light incident; ii) with a theoretical incident laser that has no classical or quantum noise; and iii) with a laser that has quantum noise.

Thermal Noise

Thermal noise causes mechanical expansion and contraction that changes the length of the interferometer arms relative to one another. There are a few main sources of thermal noise; the suspension wires or fibres that hold the test masses in place [35], the internal motion of the test masses [36] and the thermal motion of the coatings on the optics [37, 38]. Using the fluctuation-dissipation theorem [39], the root power spectral density of thermally induced fluctuations on the test mass as read by the interferometer is written [37]

$$S_{Th} = \frac{k_B T}{\pi^2 \Omega^2} \mathrm{Re}\{\mathbb{Y}(\Omega)\}, \tag{2.3}$$

where k_B is Boltzmann's constant, T is the temperature of the test mass, Ω is the frequency of the fluctuations and $\mathrm{Re}\{\mathbb{Y}(\Omega)\}$ is the mechanical admittance of the test mass to a cyclic pressure distribution that has the same form as the intensity profile of the interferometer beam. This term can be calculated with knowledge of the mechanical loss angle of the test mass response to the applied cyclic Gaussian pressure distribution [36].

One method of overcoming this noise source is to cool the masses. A new detector, to be built in Japan, known as KAGRA (previously called LCGT) [40, 41], is planning to use precisely this technique in order to minimise their thermal noise contribution, cooling their test masses and fibre suspensions to tens of Kelvins [42]. The other method for reducing thermal noise is to increase the quality factor and reduce the intrinsic loss of the materials involved. In aLIGO, the thermal noise in the test masses is decreased through the use of high quality factor fused silica test masses, the replacement of steel wires with silica fibres, and the use of advanced coatings [43, 28, 37].

Seismic Noise

Below frequencies of tens of hertz, seismic noise limits the performance of ground based detectors [44]. The magnitude of seismic noise increases rapidly at lower frequencies. Seismic noise causes motion in the test masses, resulting in interferometer noise.

Significantly improved seismic isolation systems have been produced for aLIGO that will reduce the coupling of seismic noise to test mass motion [45], but ultimately seismic noise will limit the very low-frequency performance of ground based gravitational-wave detection, below 10's of hertz. One method of reducing seismic noise is to build a detector underground, where seismic noise is reduced [46]. KAGRA is planned to be built underground for this purpose and is expected to have a sensitivity of 10^{-23} or greater down to 50 or 60 Hz depending upon the operating conditions [40]. Seismic noise can be bypasses altogether operating a gravitational-wave detector in space. This is the goal of what was originally called the Laser Interferometer Space Antenna (LISA) but is now known as the New Gravitational-Wave Observatory (NGO) [47, 48]. The operational band of this detector is expected to be from approximately 0.1 mHz up to around 1 Hz.

2.3.2 High Frequency Sensitivity

Shot Noise

In the high frequency region of the spectrum, frequencies above 100 Hz, the noise is almost entirely quantum in origin [49], as shown in Figure 2.5. All of the classical and technical noise sources drop off as the frequency increases. The photons arrive at the photodetector with a Poissonian distribution in the mean number of photons per unit time. The Fourier transform of this distribution is white noise across the entire spectrum. The optical response of the arm cavities shapes this noise source into that seen in Figure 2.5. The photon counting error, or error due to shot noise, of a Michelson interferometer is given by [25],

$$(\Delta Z)_{pc} \simeq \frac{c}{4b\pi f} \left(\frac{\hbar 2\pi f}{P\tau_m} \right)^{\frac{1}{2}} e^{-r}, \tag{2.4}$$

where $(\Delta Z)_{pc}$ is the photon-counting error, or uncertainty due to shot noise, b is the number of bounces at each end mirror, τ_m is the measurement time, P is the optical power, f is the frequency of the laser light, r is the squeezing factor, and $\hbar$ and c are the reduced Planck constant and speed of light respectively. As with Equation 2.2, a positive squeezing factor, which in this case will result in a negative exponent, implies the use of a phase squeezed state.

The strain sensitivity can be improved by increasing the values of b, f, l, P, or r. However, for each of these variables, increasing their values will eventually reach a practical limit. Perhaps the simplest method of reducing the photon counting error is to increase the optical power, P. However, increased power will eventually lead to thermal heating issues [50] and, as shown in § 2.6, increases the radiation pressure noise. Likewise, increasing the laser frequency requires investigation into new low loss materials and coatings and the development of high-power laser sources at these frequencies.

Equation 2.2 shows that most of the processes that reduce the shot noise increase the radiation pressure noise. This can be understood with a very simple principle. Error due to shot noise is reduced with increased power, whereas error due to radiation pressure noise increases with higher powers. Of note is that the same squeezing used to decrease the photon counting noise, a positive squeezing factor, will act to increase the radiation pressure noise. This is because squeezing in the phase quadrature results in anti-squeezing in the amplitude quadrature, conserving Heisenberg's uncertainty principle. The anti-squeezing increases the noise in the amplitude quadrature, resulting in an increase in the radiation pressure noise. Dependent upon the frequency band of interest and the dominating noise sources at these frequencies, phase squeezing, amplitude squeezing, or some squeezing angle between the two might be optimal. This is not made clear in the presented equations for the error due to radiation pressure noise and shot noise. It is shown in Figure 2.5 that radiation pressure noise dominates at low frequencies, and shot noise dominates at high frequencies. Progress has been made on producing frequency dependent squeezed states, which are squeezed in the amplitude quadrature at low frequencies, and squeezed in the phase quadrature at high frequencies [51]. In this way, squeezing can reduce the error due to both radiation pressure noise and shot noise in an interferometer simultaneously.

Increasing Laser Power

Equation 2.4 shows that the effect of shot noise can be reduced by increasing the laser power. The shot noise scales as the square root of the power of the optical field, whereas the signal scales as the power, therefore, an increase of the laser power by a factor of 4 will increase the signal to noise ratio of a shot noise limited system by 3 dB. However, increasing the laser power comes at a cost. Increased laser power results in larger radiation pressure noise and increased thermal effects. First, thermal lensing [43], and eventually parametric instabilities [52], will arise in the interferometer as the laser power is increased. These unwanted effects will reduce the efficiency and perhaps even more importantly, the stability of the detector.

The next generation of detectors will have the ability to operate at circulating powers of up to 0.5 MW. The original LIGO design had circulating powers of approximately 10 kW. The laser power in the initial LIGO setup was already large enough to require compensation for thermal effects [53]. With increased laser power, aLIGO is expected to require more sophisticated thermal compensation systems to ensure stable, reliable operation [54, 50, 43]. Eventually a limit will be reached where the laser power cannot be increased, whilst maintaining reliable interferometer operation. It will then be necessary to decrease the shot noise of the device through other means.

2.4 Quantum Enhancement

In order to improve the sensitivity of ground based gravitational-wave detectors for and beyond the next generation, methods will need to be introduced that are capable of reducing the quantum noise in the interferometer without increasing the operational power. Many such methods have been proposed, such as variational readout, quantum non-demolition measurements and the use of squeezing [49]. Perhaps the simplest method is through the use of squeezed states due to the fact that it is fully compatible with current detector designs (See Chapter 8. Some of the other quantum enhancement techniques require complete redesigns of current interferometers.

2.5 Optical Squeezing

Optical squeezing is a means of reducing the quantum noise in a laser field, under certain conditions, below the standard limit. The usefulness of these states has been proven in various applications such as spatial displacement measurements [55] and atomic spectroscopy measurements [56]. In 1981 Caves showed that the introduction of squeezing to a Michelson interferometer was theoretically capable of improving the sensitivity of the system [25]. However, squeezed states had not yet been produced, let alone ones that were suitable for such an application. The first squeezed state, exhibiting a mere 7 % reduction in the shot noise at a measurement frequency of 422 MHz, was observed in 1985 by Slusher *et al.* using a four wave mixing process [57]. For many years thereafter, a multitude of systems were used to produce varying levels of squeezing [58]. A goal was set by some members of the squeezing community to produce squeezed states with 10 dB of quantum noise reduction down to frequencies as low as 10 Hz [59, 49, 60]. Squeezing with these properties would provide a substantial sensitivity enhancement to interferometric detectors and would display squeezing across the entire detection band of ground based detectors, marking a time when squeezing had matured to a point where the production of squeezed states was a solved problem. This thesis presents the first measurements that have achieved this 10 dB at 10 Hz goal for squeezed light production.

2.5.1 Low-frequency Squeezing

Early squeezed states could not be used for interferometric gravitational-wave detection due to the fact that they degraded at frequencies below a few MHz [61]. Recall that Figure 2.5 shows that ground based detectors require squeezing in the audio-band, from tens of hertz up to ten kilohertz. The majority of experiments aimed at producing low-frequency squeezing have utilised the second order non-linearity in crystalline materials placed in optical cavities to generate these states. Attempts were made in one of these systems to recover the squeezing at low-frequencies by building two identical squeezers and subtracting excess noise, and while it did improve the low-frequency performance, this technique still only resulted in squeezing down to approximately 200 kHz [62].

The breakthrough was made when McKenzie *et al.* determined that the presence of a bright seed field, traditionally used to control the phase of the squeezed state, was coupling noise into the state [63]. It was determined that removing the bright seed, resulting in what is known as a vacuum squeezed state, should allow for the production of squeezed states in the audio-band. However, new control techniques would need to be introduced to control the phase of these squeezed states, which lack a coherent amplitude to use as a phase reference. Using a technique called "quantum noise locking", McKenzie *et al.* observed squeezing down to frequencies of a few hundred hertz [63]. Below these frequencies it was believed that beam pointing [64] and dust [65] were reducing the measured squeezing.

Progress was made regarding the control of these states. A new locking technique, later called "coherent locking", was developed in order to more stably control the vacuum squeezed states [66, 67]. However, degradation in the squeezing was still seen at frequencies below a couple of hundred hertz. In 2007 Vahlbruch *et al.* managed to measure large levels of squeezing, up to 6.5 dB, down to frequencies as low as tens of Hertz. The improvement was attributed to the reduction of parasitic interference (see § 8.3.4. A squeezing source had now been produced that was able to deliver a reasonable magnitude of squeezing that covered the complete frequency range of large scale interferometers. The demonstration of more squeezing, particularly at lower frequencies, was still desirable and additionally, the integration of squeezing into the detectors was a challenge that still needed to be addressed.

2.5.2 Squeezing Enhancement of Interferometers

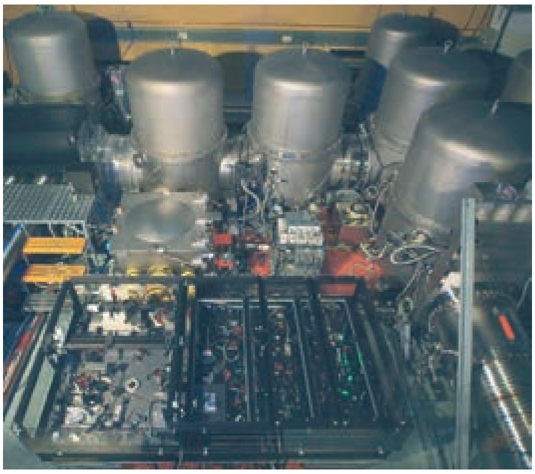

Figure 2.7: The squeezing experiment on the GEO interferometer. The squeezing is produced on the table at the bottom of the picture and injected into the interferometer located inside the vacuum chambers [68].

In the absence of low-frequency squeezing, the first experiments showcasing the improvement in sensitivity offered by squeezed states was demonstrated at higher frequencies. In 1987 Xiao *et al.* showed sensitivity improvement in a squeezing enhanced interferometer at a frequency of 1.6 MHz [69]. In 2002, McKenzie *et al.* showed a sensitivity improvement in a power-recycled squeezing enhanced Michelson interferometer at 5.5 MHz. In 2008 Goda *et al.* [70] showed a 3 dB improvement in a prototype gravitational-wave detector down to frequencies of tens of kilohertz. Only very recently has broadband improvement been demonstrated in a large scale interferometer, GEO600 [68], the experimental setup of which is shown in Figure 2.7. Reduction in the shot noise of up to 3 dB was achieved across the entire shot noise limited region, from frequencies of a couple of hundred of hertz up to ten kilohertz. A duty cycle of 99 % was achieved and the squeezing did not degrade the performance of the detector at frequencies below hundreds of hertz. The squeezing table is modular in design, meaning it can be switched off and the interferometer is able to function as normal. This landmark achievement showed that squeezing is viable in large scale interferometers to improve the high frequency sensitivity of the device. However, a more sensitive device was needed to demonstrate the effect of squeezing on the lower frequency region.

2.5.3 Squeezing in LIGO H1

The work presented in this thesis was part of an international collaboration, involving the ANU, Caltech, the Max Planck Institute for Gravitational Physics and MIT, to inject squeezing into the LIGO detector situated in Hanford, Washington State, in the United States of America. Enhanced LIGO had just finished its sixth science run and the squeezed light injection occurred as upgrades towards aLIGO were beginning [71, 29]. The enhanced LIGO Hanford detector had two interferometers within its beam tubes, H1 and H2. H2 was a shorter detector with arm lengths of 2 km and H1 had arm lengths of 4 km, which, along with the LIGO Louisiana site, had the longest arm lengths of any current detector. These two LIGO detectors were the most sensitive interferometers ever made. In particular, their low-frequency sensitivity surpassed the performance of any other interferometer [72]. Figure 2.8 shows a picture of the squeezing table at the LIGO Hanford site.

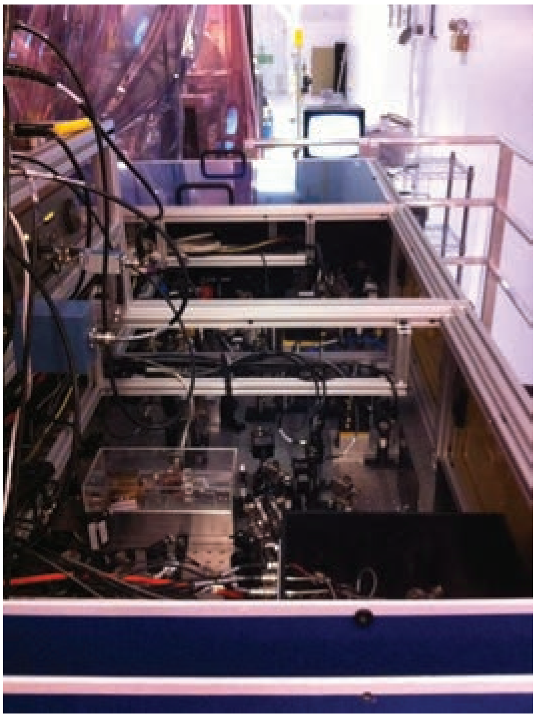

Figure 2.8: The squeezing experiment at the LIGO site.

It was previously noted that squeezing has already been shown to be viable in the GEO600 interferometric gravitational-wave detector [68]. The differentiating factors between this experiment and the LIGO injection are that the squeezer itself was to be a very different design (discussed in Chapter 6), and that the improved sensitivity of the LIGO H1 interferometer at lower frequencies would allow for the investigation of noise couplings at these frequencies. With the injection of squeezed light, it was also expected that the sensitivity of the device would exceed that previously seen by any gravitational wave detector.

Chapter 3

Quantum States of Light

This chapter introduces the formal description of the quantised electromagnetic field. This will form the basis for an investigation into squeezed states and their application in gravitational-wave detectors. First, the quadrature operators of the light field and their uncertainty relation are introduced. From here the necessary properties of these states of light and various methods of visualising these states are detailed. The effect of loss on squeezed states is investigated and the standard method for detecting these states of light, balanced homodyne detection, is analysed.

3.1 The Quantum Mechanical Electromagnetic Field

A quantum mechanical picture of light begins with quantization of the electromagnetic field. The details of this procedure are not described here but can be found in [73]. The result is that we can describe an optical mode, k, in terms of the annihilation and creation operators, $\hat{a}_k$ and $\hat{a}_k^\dagger$ respectively, in much the same way that one can describe a quantum harmonic oscillator [74]. As with the quantum harmonic oscillator, vacuum energy is present for every optical mode k, which is this case is given by $E = \frac{1}{2}\hbar\omega_k$. A classical description of the electromagnetic field does not include a description of these vacuum modes, and as such they are a defining feature of the quantum mechanical description. These vacuum fluctuations are the lowest energy state of the field and can be regarded as the instantaneous creation of particle and anti-particle pairs. In order to measure quantum mechanical states of light, including the vacuum state, it is first necessary to develop a framework for describing them.

3.1.1 Quadratures

Electric fields are often written in complex form, given by $E = Ce^{i\omega t}$, where C is the amplitude of the wave, ω is the angular frequency and E is the electric field [75]. In this form, equations are often compact and easy to manipulate. However, in some situations, this is not the most useful representation. The quadrature representation of the electromagnetic field is an alternative method of describing the electromagnetic field. The operators arising form this description are Hermitian, and therefore observable in the lab, providing a method by which quantum mechanical theories can be tested.

3.1.2 Quadrature Operators

The annihilation and creation operators, $\hat{a}$ and $\hat{a}^\dagger$ respectively, can be used to describe the electromagnetic field but they are not Hermitian, and are therefore not observable. In order to relate measurements in the lab to the theory it is necessary to introduce Hermitian operators. This is the role that the amplitude, $\hat{X}^{+}$, and phase, $\hat{X}^{-}$, quadrature operators fulfil, they can be written [76]

$$\hat{X}^{+} = \hat{a} + \hat{a}^{\dagger} \tag{3.1}$$

$$\hat{X}^{-} = i(\hat{a}^{\dagger} - \hat{a}). \tag{3.2}$$

By definition, the amplitude quadrature operator is chosen to have an angle that aligns with the coherent amplitude of the state. Under certain circumstances this can complicate issues because the chosen reference frame may rotate. We can also write a more general form of these operators

$$\hat{X}^{\theta} = \hat{a}e^{-i\theta} + \hat{a}^{\dagger}e^{i\theta}, \tag{3.3}$$

where θ is the angle of the field relative to a second field. The amplitude and phase quadrature operators are particular cases of the general quadrature operator. For $\theta = 0$ Equation 3.3 results in the amplitude quadrature operator and for $\theta = \frac{\pi}{2}$ it returns the phase quadrature operator. Provided that they are orthogonal to one another, which is to say that there is a $\frac{\pi}{2}$ difference between the angles, θ, of the operators, any pair of quadrature operators can be used to describe the various states of light.

3.2 The Heisenberg Uncertainty Principle

The uncertainty relation between the phase and amplitude quadrature operators can now be determined. Heisenberg's uncertainty principle for a pair of non-commuting observables is given by

$$\Delta(\hat{G})\Delta(\hat{H}) \geq \frac{1}{2i}\langle[\hat{G},\hat{H}]\rangle, \tag{3.4}$$

where $\Delta(\hat{G})$ and $\Delta(\hat{H})$ are the standard deviation in the observables $\hat{G}$ and $\hat{H}$ and $\langle[\hat{G},\hat{H}]\rangle$ is the expectation value of the commutation relation of the Hermitian operators $\hat{G}$ and $\hat{H}$. The commutation relation between the two operators, $\hat{G}$ and $\hat{H}$, is defined by

$$[\hat{G},\hat{H}] = \hat{G}\hat{H} - \hat{H}\hat{G}. \tag{3.5}$$

Using the boson commutation relations, $[a, a^{\dagger}] = 1$ and $[a, a] = [a^{\dagger}, a^{\dagger}] = 0$ [73], we can now calculate the uncertainty relation for the any pair of orthogonal quadrature operators,

$$\Delta(\hat{X}^{\theta})\Delta(\hat{X}^{\theta+\frac{\pi}{2}}) \geq 1. \tag{3.6}$$

Equation 3.6 is integral to the work presented in this thesis. In fact, it is direct manipulation of this equality that describes much of the work presented.

3.2.1 State Variance

It is typically the variance of the observable in question which is measured in the lab and not the standard deviation, as will be discussed in § 3.7.2. We define the variance, Δ^2, of an arbitrary operator $\hat{G}$ as,

$$\begin{aligned} V(\hat{G}) &= \Delta^2(\hat{G}) \\ &= (\Delta(\hat{G}))^2 \\ &= \langle\hat{G}^2\rangle - \langle\hat{G}\rangle^2. \end{aligned} \tag{3.7}$$

Notice that this also defines a relationship between the variances of the operators as set by the Heisenberg uncertainty relationship,

$$\Delta^2(\hat{X}^+)\Delta^2(\hat{X}^-) \geq 1. \tag{3.8}$$

3.2.2 Minimum Uncertainty States

A minimum uncertainty state is defined as any state where Equation 3.8 is a strict equality. A minimum uncertainty state can thus be written

$$\Delta^2(\hat{X}^+)\Delta^2(\hat{X}^-) = 1. \tag{3.9}$$

A minimum uncertainty state is one in which no classical noise is present. It is not uncommon to produce these states under certain conditions. For example, solid-state lasers are often in this minimum uncertainty state at frequencies where the low-frequency technical noise has rolled off. This typically occurs above a few megahertz. For example, a typical Nd:YAG system might be in a minimum uncertainty state at 20 MHz or lower [77]. Another way of saying this is that above these frequencies, the performance of many lasers is governed by Heisenberg's uncertainty principle.

3.2.3 Squeezing Purity

Imperfect processes, such as loss, will result in an output state that is not a minimum uncertainty state. We can define the squeezing purity, henceforth simply known as the purity, of a state, P as a means of quantifying this loss (the effect of loss is shown in §3.6. This value is not to be confused with the traditional quantum state purity [78], which is not used in this thesis. The purity is written as

$$\Delta^2(\hat{X}^+)\Delta^2(\hat{X}^-) = P. \tag{3.10}$$

A pure state will have a purity of $P = 1$, as does the vacuum. The value P, as described here, increases as loss is introduced but will eventually begin to decrease as the state approaches the vacuum state with very large losses [76]. This value is particularly important for squeezed states, as it is a measure of the efficiencies of the processes used to produce and measure the state. Excess noise in particular systems reduces Einstein-Podolsky-Rosen (EPR) entanglement [79] and as such is a limitation to many entanglement experiments [80, 81].

3.2.4 The Number Operator

The number operator, $\hat{n}$, is defined by

$$\hat{n} = \hat{a}^\dagger\hat{a}. \tag{3.11}$$

When operated upon a mode, $\langle\hat{\alpha}|\hat{n}|\hat{\alpha}\rangle$, returns the average number of particles in the mode. This operator is particularly useful when describing number, or Fock states. A Fock state is a state of light where the number of photons in the state is well known. It is particularly relevant to states with very small numbers of photons, such as the single photon state. The number operator can be used when determining the power in a state because the power is proportional to the number of photons.

3.3 Linearisation

Linearisation of the creation and annihilation operators can be used, under appropriate circumstances, to simplify calculations. The first order linearisation of the annihilation operator is written

$$\hat{a}(t) = \alpha + \delta\hat{a}(t), \tag{3.12}$$

where α is the complex classical coherent amplitude and $\delta\hat{a}(t)$ is the first order fluctuating term. The same process can be repeated for the creation operator. Linearisation requires that the average of the fluctuations in the field is zero and that the coherent amplitude of the state of light is much larger than the first order fluctuation term. These requirements are written

$$\begin{aligned} \langle \delta\hat{a}(t) \rangle &= 0 && (3.13) \\ |\, \delta\hat{a}(t) \,| &\ll |\, \alpha \,| \,. && (3.14) \end{aligned}$$

It is also useful to linearise the number operator

$$\begin{aligned} \hat{n} &= \hat{a}^\dagger \hat{a} \\ &= (\alpha^* + \delta\hat{a}^\dagger)(\alpha + \delta\hat{a}) \\ &= \alpha^2 + \alpha(\delta\hat{a} + \delta\hat{a}^\dagger) + \delta\hat{a}^\dagger\delta\hat{a} \\ &\approx \alpha^2 + \alpha(\delta\hat{X}^+) && (3.15) \end{aligned}$$

where the second order fluctuation term has been removed.

3.4 Representing the States of Light

In this section the *ball-on-stick* and *sideband* representations of the states of light are introduced. These tools provide an intuitive way of visualising the various states of light.

3.4.1 Ball-on-Stick Representation

The ball-on-stick figure is the phase space diagram of the states of light. At a glance, the coherent amplitude, α, the standard deviation of the quadratures on the axes, $\Delta(\hat{X}^\theta)$ and $\Delta(\hat{X}^{\theta+\pi/2})$, and the phase of the state, ϕ, can be identified. Figure 3.1 shows the ball-on-stick representation for a coherent state, the details of which will be introduced in § 3.5.2. The ball-on-stick representation can be regarded as an ensemble of measurements of the amplitude and phase of the state. Each measurement of the state is plotted against the two quadratures and eventually, as many measurements are made, leads to the ball-on-stick diagram. The noise in the state will produce the ball and the stick is drawn from the origin to the average of these measurements. The length of the stick then defines the coherent amplitude and the angle of the stick, the phase of the state.

3.4.2 Sideband Representation

The sideband represenation is complementary to the ball-on-stick representation. Any modulation on some carrier field at some frequency, Δ, can be represented as sidebands around the carrier field at a frequency separation of Δ from the carrier. In this representation we move into the reference frame of the carrier. This means that when the sideband

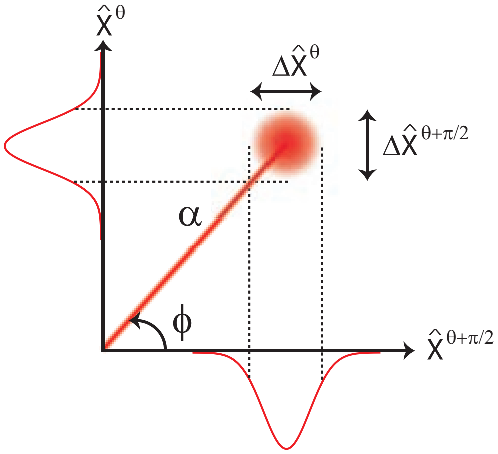

Figure 3.1: The ball-on-stick representation of a coherent state with coherent amplitude, α, and phase, ϕ. The projection of the uncertainty ball onto the two axes indicates the standard deviations, $\Delta(\hat{X}^{\theta,\theta+\pi/2})$ of the two quadrature operators.

representation of a state is drawn, this figure is of a snapshot in time. If one were to draw the representation at some later time, the figure will have evolved. Sidebands above the carrier frequency rotate in one direction and sideband fields below the carrier rotate in the opposite direction. These sidebands add together to modulate the carrier field and as such it is the relative alignment of the sidebands at frequencies Δ and $-\Delta$ that determine the dynamics of the carrier at the frequency Δ. Figure 3.2 shows the sideband representation for a coherent state.

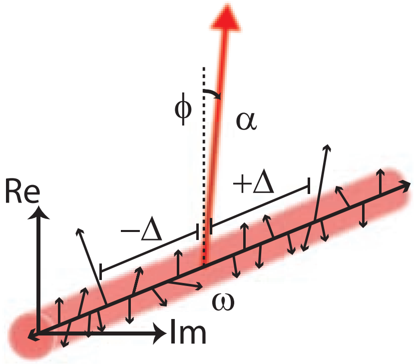

Figure 3.2: The sideband representation of a coherent state with coherent amplitude, α, and phase, ϕ. Quantum noise in the state is represented by a cylinder of quantum sidebands spanning the entire spectrum. The sideband pair at $\pm\Delta$, which are above the quantum noise level, define the motion of the carrier at the frequency Δ.

The quantum sidebands around the carrier frequency are equal in magnitude at all frequencies and beat with the carrier field. This causes the length and phase of the carrier field to fluctuate. If one were to take a slice of the sideband representation at a single frequency, the ball-on-stick diagram could be constructed from this information.

3.5 Introducing the States of Light

Now that the framework for describing and visualising various states of light has been constructed, we can introduce the relevant states of light; the coherent state, the vacuum state, the squeezed state and the squeezed vacuum state.

3.5.1 Vacuum State

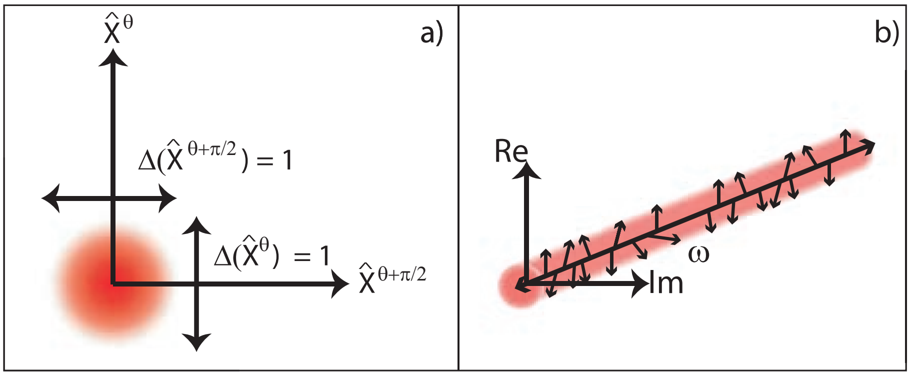

Figure 3.3: The ball-on-stick a) and sideband b) representations of the vacuum state of light.

The vacuum state has no coherent amplitude, determined by operating on this state with the number operator,

$$\langle 0 \mid \hat{n} \mid 0 \rangle = 0. \tag{3.16}$$

Even though there is no coherent amplitude, the vacuum state is not free from fluctuations. It is a minimum uncertainty state with equal noise in all quadratures,

$$\Delta(\hat{X}^{+}) = \Delta(\hat{X}^{-}) = 1. \tag{3.17}$$

These fluctuations are a consequence of the non-zero ground state energy of the quantum harmonic oscillator. It is commonly referred to as zero-point energy or vacuum fluctuations and can also be regarded as virtual particles. These fluctuations occur in every possible optical mode and this has important ramifications when considering optical loss, on squeezed states in particular.

3.5.2 Coherent State

The coherent state, $|\alpha\rangle$, can be produced through application of the displacement operator, $\hat{D}$, on the vacuum state

$$\hat{D}(\alpha)|0\rangle = |\alpha\rangle, \tag{3.18}$$

where the displacement operator is defined by

$$\hat{D}(\alpha) = e^{(\alpha\hat{a}^{\dagger} - \alpha^{*}\hat{a})}. \tag{3.19}$$

The representations of the coherent state are shown in Figure 3.4.

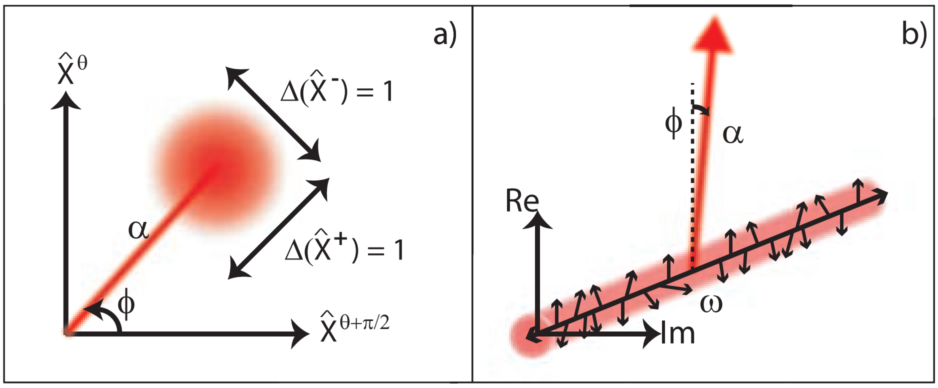

Figure 3.4: The ball-on-stick a) and sideband b) representations of a coherent state of light with phase θ and coherent amplitude α.

The coherent state is a minimum uncertainty state, and has the same noise properties as the vacuum state,

$$\Delta(\hat{X}^{+}) = \Delta(\hat{X}^{-}) = 1. \tag{3.20}$$

The coherent state is also defined as having a coherent amplitude that is greater than zero. An ideal laser source would produce a coherent state at all measurement frequencies. However, technical limitations in the low-frequency regime tend to add additional classical noise to the state. As mentioned in § 3.9, the lasers used in this work tend to be shot noise limited above a couple of megahertz. This is analogous to saying that these lasers produce coherent states above these frequencies.

3.5.3 Squeezed State

Squeezed states can be generated through the use of the squeeze operator, $\hat{S}(\rho)$, and the displacement operator,

$$\hat{D}(\alpha)\hat{S}(\rho)|0\rangle = |\alpha, \rho\rangle. \tag{3.21}$$

The squeezing operator is defined by

$$\hat{S}(\rho) = e^{\frac{1}{2}(\rho^{*}\hat{a}\hat{a} - \rho\hat{a}^{\dagger}\hat{a}^{\dagger})} \tag{3.22}$$

$$\rho = re^{i\varphi}, \tag{3.23}$$

where $r \geq 0$ is known as the squeezing parameter and ψ is the angle of the squeezing.

The squeezing operator reduces the noise in some quadrature by a factor or e^{-r} and increases it by a factor of e^r in the conjugate observable. The noise in the conjugate quadrature is necessarily increased such that the Heisenberg uncertainty relation between the two observables is not violated. A squeezed state of light is shown in Figure 3.5.

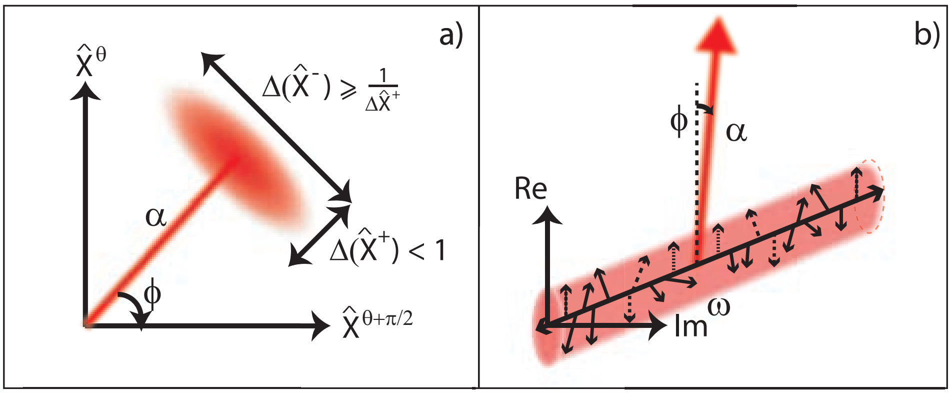

Figure 3.5: The ball-on-stick a) and sideband b) representations of a squeezed state of light with phase θ and coherent amplitude α. Correlated sideband pairs are represented by matching dashed and/or dotted lines in b)

Note that squeezed states need not be minimum uncertainty states. In fact, any real state will have some loss from any number of sources, such as scattering or absorption. This loss will reduce the purity of these states, as discussed in § 3.6.

For an amplitude squeezed state, application of the number operator will yield

$$\langle \alpha, \rho \mid \hat{a}^{\dagger}\hat{a} \mid \alpha, \rho \rangle = \sinh^2(r) + |\alpha|^2. \tag{3.24}$$

The variance of the quadrature is found to be

$$\Delta^2(\hat{X}^{+}) = e^{-2r} \tag{3.25}$$
$$\Delta^2(\hat{X}^{-}) = e^{2r}. \tag{3.26}$$

Inspection of the squeezing operator, Equation 3.22, shows that this operator acts to create or destroy photons in pairs. In fact it is these pairs of photons that are the source of squeezing.

Squeezed Vacuum States

Squeezed vacuum states are simply squeezed states with no coherent amplitude. However, Equation 3.24 shows that the squeezing operation produces photons. The photons produced are correlated photon pairs. The angle of the squeezing is determined by how these photon pairs align in the sideband representation. Whilst squeezed vacuum states have no coherent amplitude, they are still sensitive to loss because the removal of these correlated sidebands leaves more noisy vacuum fluctuations in its place. The various representations of the squeezed vacuum state are shown in Figure 3.6.

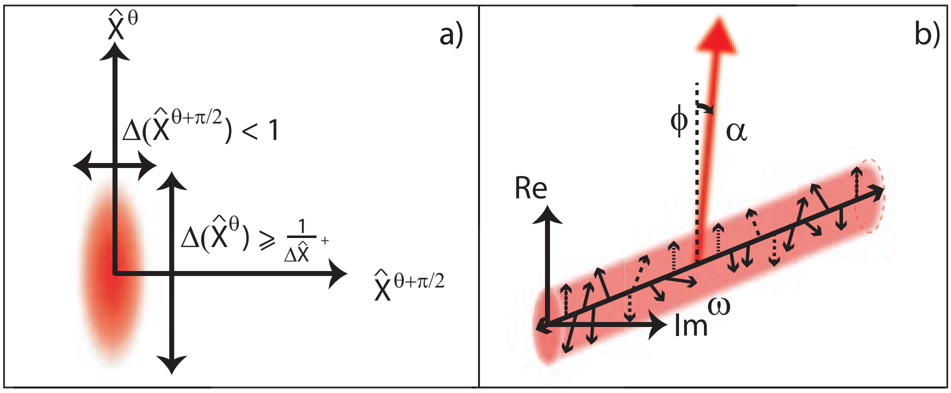

Figure 3.6: The ball-on-stick a) and sideband b) representations of a squeezed vacuum state of light. Correlated sideband pairs are represented by matching dashed and/or dotted lines.

3.6 Squeezed State Loss

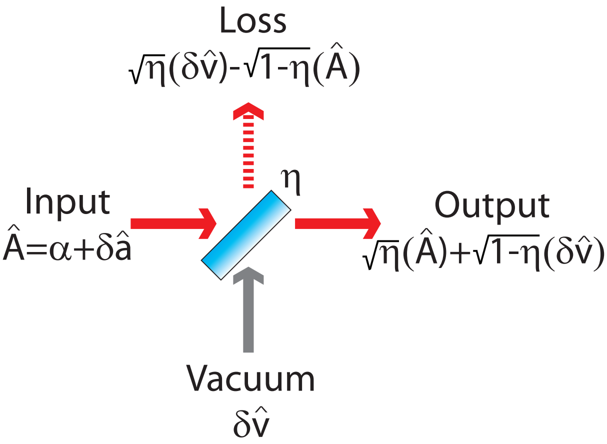

Figure 3.7: Modelling loss on an optical state. The power transmissivity of the beamsplitter, η, can be regarded as the efficiency of propagation of the field.

Optical loss can occur from many different processes such as absorption, scattering and transmission. Due to the presence of vacuum fields, the effect of loss on quantum states can have a large impact. To understand loss, we model the process as a beamsplitter with a power transmissivity of η, as shown in Figure 3.7. In this way, η can also be considered as a measure of the efficiency of some process. An η value of 1 corresponds to no state loss and the noise properties of the output of the process is equal to the input. The beamsplitter can be regarded as having two input ports and two output ports. One of the input ports has a bright field, $\mathrm{A} = \alpha + \delta a$, and the second input port is the vacuum field, $\delta\hat{v}$. The output field is then the field that has passed through the beamsplitter and has been attenuated by a factor of $\sqrt{\eta}$. The remaining field, labelled loss, is considered to be removed from the system and is unmeasurable, thus representing loss. The output field, $\hat{A}_{out}$ is written

$$\hat{A}_{out} = \sqrt{\eta}\hat{A} + \sqrt{1-\eta}\delta\hat{v} \tag{3.27}$$

If η is not unity then we couple noise from the vacuum field, δv, into the output via beamsplitter power transmissitivity, η. In many situations this vacuum field is of little consequence because the noise of the vacuum field is either identical to, or much less than, the noise on the original input field. However, if the input field is squeezed then, by definition, the noise on the vacuum field is greater. The squeezing measurable at the output will now be less than the amount of squeezing that was measurable at the input due to the added noise from the vacuum field. This effect is extremely important as the loss of a system will set a hard upper bound on the improvement that squeezing can offer.

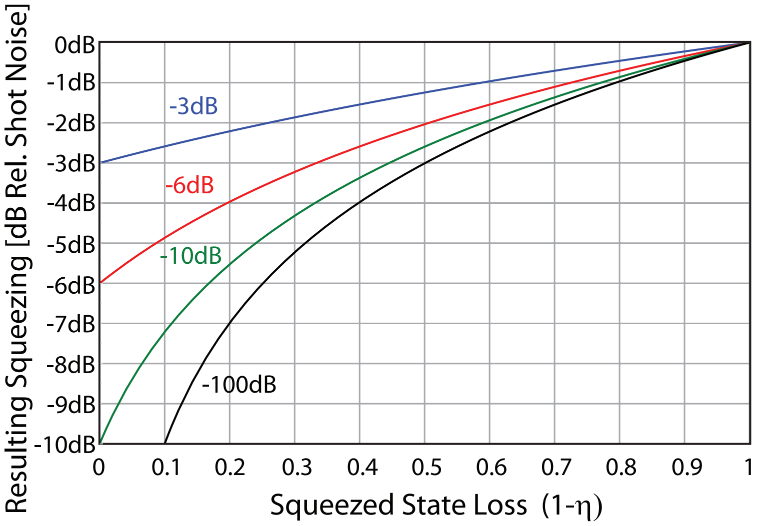

Figure 3.8: The effect of loss on various initial squeezed states.

It is important to have an intuition of the effect of loss on squeezed states. Figure 3.8 shows the resulting squeezing from four different initial squeezed states after having undergone various losses, $(1-\eta)$. The four initial squeezed states have 3, 6, 10, and 100 dB suppression of the quantum noise when compared to a field with equal intensity. Along the y-axis it can be seen that, as expected, a value of $\eta = 1$, or no loss, results in squeezing equal to that of the initial state. It can also be seen that with total loss of the initial squeezed state, $\eta = 1$, all traces converge to 0 dB, or the vacuum shot noise set by Heisenberg's uncertainty principle. The 100 dB state, although currently impossible to produce, illustrates the point that even with infinite squeezing, for a given loss there is a maximum amount of squeezing that can still be measured. With a 50% loss, we can only ever hope to measure 3 dB of squeezing, even if our original input state is infinitely squeezed. At higher losses, the dependence on the initial amount of squeezing also tends to be less important. With a 70% loss, a 6 dB initial state will result in a squeezing level of just over 1.1 dB, whereas a 100 dB initial state will result in approximately 1.5 dB.

Another way of looking at this is to consider what happens to a pure squeezed state after undergoing various levels of loss. The ball-on-stick representation of this situation is illustrated in Figure 3.9. The resulting states after a pure, 10 dB squeezed state has undergone power losses of 25, 50, 75 and 100 percent are shown. Figure 3.9 shows that loss results in degradation of the squeezing, and also gives a feeling for the rate at which the squeezing and anti-squeezing degrades.

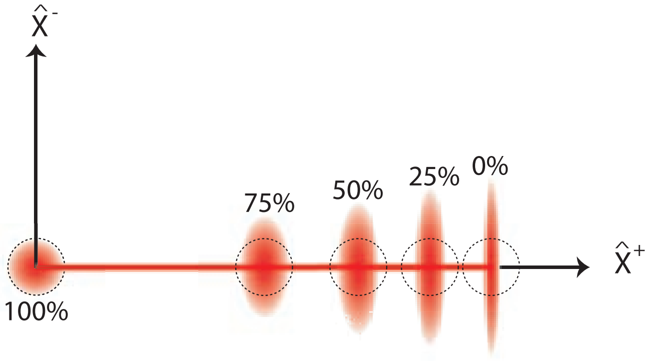

Figure 3.9: The effect of power losses of 25, 50, 75 and 100 percent on an initial pure 10 dB squeezed state are shown.

3.7 State Measurement

States of light are typically measured using a photodetector, consisting of a photodiode and a trans-impedance gain stage, and the resulting signal is then observed on either a spectrum analyser or an oscilloscope. The photodetector is shown in Figure 3.10.

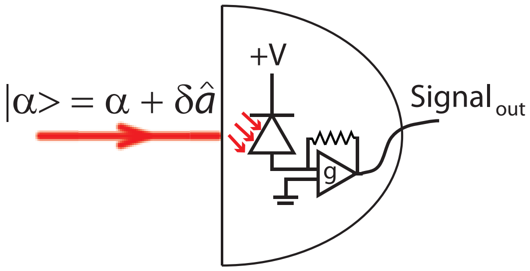

Figure 3.10: Detection of a an optical state, $|\alpha\rangle$, with a photodetector. This simple photodetector consists of a photodiode and a trans-impedance gain stage.

Ideally, the photodiode provides a one-to-one conversion of photons into electrons. Due to this, the photocurrent, i, immediately after the photodiode follows the intensity of the input field. The gain stage then converts this current signal into a voltage signal, with an amplification factor of g Ohms, resulting in

$$\begin{aligned} \text{Signal}_{out} &= gi \\ &= g(\alpha + \delta a)(\alpha^* + \delta a^\dagger) \\ &\approx g(\alpha^2 + \alpha(\delta \hat{X}^+(t))). \end{aligned} \tag{3.28}$$

3.7.1 Oscilloscope Measurements

Oscilloscopes are a means of measuring voltages in the time domain. Equation 3.28 is a voltage signal and hence oscilloscopes directly measure this value. The signal consists of a DC term proportional to the intensity, α^2, and a scaled fluctuation term, $\alpha(\delta\hat{X}^+)$.

3.7.2 Spectrum Analysers

In contrast to the oscilloscope, a spectrum analyser provides measurements in the frequency domain. It measures the variance of the input voltage signal for the frequency band in question. This variance in the voltage is proportional to the intensity spectrum of the incident laser field. For the output of our photodetector, given by Equation 3.28, we find

$$\begin{aligned} V(\mathrm{Signal}_{\mathrm{out}}) &\approx g(\alpha^2 + \alpha(\delta\hat{X}^+(t)) \\ &= g^2\alpha^2 V(X^+(t)), \end{aligned} \tag{3.29}$$

which is found making use of the identity,

$$V(aX + b) = a^2 V(X). \tag{3.30}$$

We can then transform this into the frequency domain to determine the signal measured with the spectrum analyser.

$$V(\mathrm{Signal}_{\mathrm{out}}(\omega)) = g^2\alpha^2 V(\check{X}^+(\omega)), \tag{3.31}$$

where the caron, or inverted hat, is used to signify operators in the frequency domain. The final step is to then determine the variance of the amplitude quadrature operator in the frequency domain. Using linearisation we can write

$$\begin{aligned} V(\check{X}^+(\omega)) &\equiv \Delta^2(\check{X}^+) \\ &= \langle(\check{X}^+)^2\rangle - \langle\check{X}^+\rangle^2 \\ &= \langle(\check{a} + \check{a}^\dagger)^2\rangle - \langle\check{a} + \check{a}^\dagger\rangle^2 \\ &= \langle(\alpha + \delta\check{a} + \alpha^* + \delta\check{a}^\dagger)^2\langle - \langle\alpha + \delta\check{a} + \alpha^* + \delta\check{a}^\dagger\rangle^2 \\ &= \langle(\delta\check{a} + \delta\check{a}^\dagger)^2\rangle \\ &= \langle(\delta\check{X}^+)^2\rangle. \end{aligned} \tag{3.32}$$

The variance for the phase quadrature operator is found in much the same way

$$\begin{aligned} V(\check{X}^-(\omega)) &\equiv \Delta^2(\check{X}^-) \\ &= \langle(\check{X}^-)^2\rangle - \langle\check{X}^-\rangle^2 \\ &= \langle(i(\delta\check{a}^\dagger - \delta\check{a}))^2\rangle \\ &= \langle(\delta\check{X}^-)^2\rangle. \end{aligned} \tag{3.33}$$

3.8 Balanced Homodyne Detection

Loss is one limitation to the measurement of many of these quantum states of light but the measurement itself is also a complicated issue. Measuring the quantum noise in these states requires that all classical noise terms, such as laser intensity noise and electronic noise, are reduced to a level well below the noise level of interest (This is discussed in detail in § 8.3.1). In the case of squeezed light, where the noise in some quadrature may have been reduced by even more than one order of magnitude below the shot noise limit, achieving the required suppression of classical noise is non-trivial. A measurement system that allows for the detection of any general quadrature, including the amplitude and phase quadratures, is also necessary in order to fully characterise the measured states. All of these conditions can be met using the balanced homodyne detector [82], illustrated in Figure 3.11.

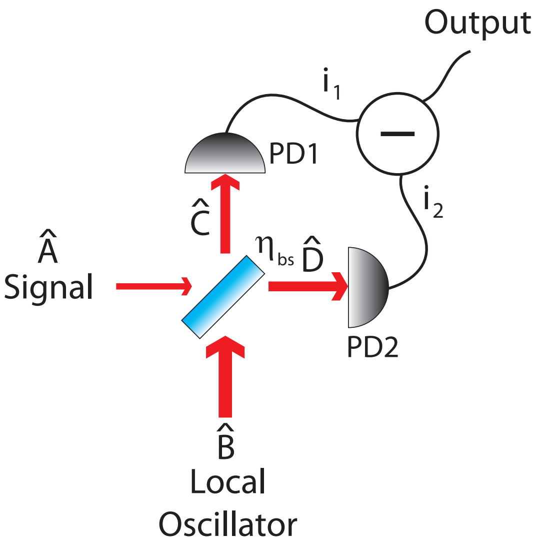

Figure 3.11: The idealised balanced homodyne detector. The signal and the local oscillator (LO) fields are both incident on the beamsplitter, of power transmissivity $\eta_{bs} = 0.5$, and the two output fields are detected on separate photodetectors, PD1 and PD2.

In the balanced homodyne detector the weak *signal field*, whose noise properties one wishes to measure, and a bright *local oscillator* (LO) field, used to amplify and probe the signal field, interfere on a beamsplitter with a power transmissivity of $\eta_{\rm bs}$, which is ideally 50 %. Using linearisation (§ 3.3) the signal field is labelled as $\hat{A} = \alpha_a + \delta\hat{a}$ and the local oscillator field as $\hat{B} = \alpha_b + \delta\hat{b}$, where the subscripts a and b on the coherent amplitudes, α, are used to distinguish between amplitudes of the signal and local oscillator fields respectively.

The fields incident on the two photo-detectors, $\hat{C}$ and $\hat{D}$, are written

$$\hat{C} = \sqrt{1-\eta_{bs}}\hat{A} + \sqrt{\eta_{bs}}\hat{B} \tag{3.34}$$
$$\hat{D} = \sqrt{\eta_{bs}}\hat{A} - \sqrt{1-\eta_{bs}}\hat{B}. \tag{3.35}$$

Here we will ensure that the coherent amplitude terms of the fields are real by separating the relative phase between the two fields into a phase term, $\hat{B}$, where $\hat{B} = \hat{B}e^{i\theta}$. We can now write

$$\hat{C} = \sqrt{1-\eta_{bs}}\hat{A} + \sqrt{\eta_{bs}}\hat{B}e^{i\theta} \tag{3.36}$$
$$\hat{D} = \sqrt{\eta_{bs}}\hat{A} - \sqrt{1-\eta_{bs}}\hat{B}e^{i\theta}. \tag{3.37}$$

Assuming that the photodetectors are perfect, every photon hitting the detectors will result in an electron at the output of the detector. The photocurrent produced by PD1 is equal to $\hat{C}^\dagger\hat{C}$ and the photocurrent from PD2 is equal to $\hat{D}^\dagger\hat{D}$. The two photocurrents, i_1 and i_2 can then be written,

$$\begin{aligned}
\mathrm{i}_1 &= \hat{C}^\dagger\hat{C} \\
&= (1-\eta_{bs})\hat{A}^\dagger\hat{A} + \eta_{bs}\hat{B}^\dagger\hat{B} + \sqrt{\eta_{bs}(1-\eta_{bs})}(\hat{A}^\dagger\hat{B}e^{i\theta} + \hat{B}^\dagger\hat{A}e^{-i\theta}) \qquad (3.38)\\
\mathrm{i}_2 &= \hat{D}^\dagger\hat{D} \\
&= \eta_{bs}\hat{A}^\dagger\hat{A} + (1-\eta_{bs})\hat{B}^\dagger\hat{B} - \sqrt{\eta_{bs}(1-\eta_{bs})}(\hat{A}^\dagger\hat{B}e^{i\theta} + \hat{B}^\dagger\hat{A}e^{-i\theta}). \qquad (3.39)
\end{aligned}$$

As shown in Figure 3.11, the output of the homodyne detector is then the resulting signal when these two photocurrents are subtracted. The result is

$$\mathrm{i}_1 - \mathrm{i}_2 = (1-2\eta_{bs})\hat{A}^\dagger\hat{A} + (2\eta_{bs}-1)\hat{B}^\dagger\hat{B} + 2\sqrt{\eta_{bs}(1-\eta_{bs})}(\hat{A}^\dagger\hat{B}e^{i\theta} + \hat{B}^\dagger\hat{A}e^{-i\theta}). \quad (3.40)$$

Utilising the linearisation technique described in § 3.3 allows for simplification of some of the terms in Equation 3.40. We begin by recalling that the problem was constructed such that the coherent fields are real, and we choose to drop terms of second order. Using these simplifications we can write

$$\begin{aligned}
\hat{A}^\dagger\hat{A} &\approx (\alpha_a^* + \delta\hat{a}^\dagger)(\alpha_a + \delta\hat{a}) \\
&\approx \alpha_a^2 + \alpha_b\delta X_A^+ \qquad (3.41)\\
\hat{B}^\dagger\hat{B} &\approx (\alpha_b^* + \delta\hat{b}^\dagger)(\alpha_b + \delta\hat{b}) \\
&\approx \alpha_b^2 + \alpha_b\delta X_B^+. \qquad (3.42)
\end{aligned}$$

where $\delta X_A^+ = \delta\hat{a} + \delta\hat{a}^\dagger$ is the amplitude quadrature operator for the field $\hat{A}$, and $\delta X_B^+ = \delta\hat{b} + \delta\hat{b}^\dagger$ is the amplitude quadrature operator for the field $\hat{B}$. Making use of Equations 3.41 and 3.42 we can now simplify Equation 3.40, resulting in

$$\begin{aligned}
\mathrm{i}_1 - \mathrm{i}_2 \approx\ & (1-2\eta_{bs})(\alpha_a^2 + \alpha_a\delta X_A^+) + (2\eta_{bs}-1)(\alpha_b^2 + \alpha_b\delta X_B^+) + \\
& 2\sqrt{\eta_{bs}(1-\eta_{bs})}[(\alpha_a^* + \delta\hat{a}^\dagger)(\alpha_b + \delta\hat{b})e^{i\theta} + (\alpha_b^* + \delta\hat{b}^\dagger)(\alpha_a + \delta\hat{a})e^{-i\theta}].
\end{aligned} \quad (3.43)$$

This can be rewritten (using various trigonometric identities on the exponential terms) as

$$\begin{aligned}
\mathrm{i}_1 - \mathrm{i}_2 \approx\ & (1-2\eta_{bs})(\alpha_a^2 + \alpha_a\delta X_A^+) + (2\eta_{bs}-1)(\alpha_b^2 + \alpha_b\delta X_B^+) + 2\sqrt{\eta_{bs}(1-\eta_{bs})}\ \times \\
& \left[2\alpha_a\alpha_b\mathrm{Cos}\theta + \alpha_a\left(\delta\hat{X}_B^+\mathrm{Cos}\theta - \delta\hat{X}_B^-\mathrm{Sin}\theta\right) + \alpha_b\left(\delta\hat{X}_A^+\mathrm{Cos}\theta + \delta\hat{X}_A^-\mathrm{Sin}\theta\right)\right].
\end{aligned} \quad (3.44)$$

It is typically required that the local oscillator field strength, α_b, is much brighter than the signal field in order to suppress the noise from the local oscillator. For most of the work presented in this thesis the signal field is a vacuum squeezed state, with no coherent amplitude, and hence this condition is easily met. This condition allows us to remove all terms that do not contain the coherent amplitude of the LO field, α_b, resulting in

$$\begin{aligned} \mathrm{i}_1 - \mathrm{i}_2 &\approx (2\eta_{bs} - 1)(\alpha_b^2 + \alpha_b \delta X_B^+) + \\ & 2\sqrt{\eta_{bs}(1-\eta_{bs})}\left[2\alpha_a\alpha_b \mathrm{Cos}\theta + \alpha_b\left(\delta\hat{X}_A^+\mathrm{Cos}\theta + \delta\hat{X}_A^-\mathrm{Sin}\theta\right)\right]. \end{aligned} \tag{3.45}$$

If we now assume that our beamsplitter ratio is exactly 50 % we completely subtract the contributions from the local oscillator field and Equation 3.45 simplifies to

$$\mathrm{i}_1 - \mathrm{i}_2 \approx 2\alpha_a\alpha_b \mathrm{Cos}\theta + \alpha_b\left(\delta\hat{X}_A^+\mathrm{Cos}\theta + \delta\hat{X}_A^-\mathrm{Sin}\theta\right). \tag{3.46}$$

It is worth taking a moment and considering the ramifications of this equation. The first term, $2\alpha_a\alpha_b\mathrm{Cos}\theta$, is a DC term that describes the interference between the two fields as the phase of the local oscillator, θ, is varied. If the two fields are in exactly the same spatial mode then this term will completely vanish, given an appropriate value for θ. In practice, however, the two fields are never perfectly matched in shape and size and hence this term will not completely vanish. The overlap between the two fields can be quantified using the *visibility* of the balanced homodyne detector, which will be introduced in § 3.8.1.

The remaining terms are the quantum noise terms. The quantum noise terms have been "amplified" by the coherent amplitude term of the LO field, which we see occurs without adding any noise from the LO field in the case of perfect subtraction. This gain factor allows us to measure vanishingly small quantum noise terms on the signal field. It is also evident that as the phase of the LO field is varied, the noise seen at the output is some mixture of amplitude and phase quadratures. The balanced homodyne detector, by varying the phase of the LO, works as a measuring device for any general quadrature operator that we wish to measure, allowing us to fully characterise the noise characteristics of any state.

3.8.1 Balanced Homodyne Detector Fringe Visibility

The visibility of the homodyne detection system is a measure of the overlap between the signal and local oscillator fields. In order to achieve complete destructive or constructive interference the waist size and waist position of the two fields must be exactly the same. If this is not the case then the wavefronts will not match and the same phase relationship will not be kept over the entire beam. The visibility is a way of quantifying the spatial mode mismatch between the signal and LO fields and is given by

$$\mathcal{V} = \frac{I_{Max} - I_{Min}}{I_{Max} + I_{Min}}. \tag{3.47}$$

I_{Max} is the maximum intensity seen as the phase is varied, which corresponds to constructive interference, and I_{Min} is the minimum intensity measured, corresponding to destructive interference. The values are determined by ensuring that the power of the local oscillator and signal fields are first equal. The phase of the local oscillator is then swept whilst examining the output DC term on an oscilloscope.

It can be shown that the fringe visibility is equivalent to optical loss on the signal field [83]. If the equivalent loss due to an imperfect fringe visibility is given by η_{vis}, it can be defined as

$$\eta_{vis} = \mathcal{V}^2. \tag{3.48}$$

It is perhaps not surprising that an inefficient spatial overlap between these two fields is equivalent to a loss on the signal field. Equation 3.46 shows that the noise terms from the signal field are amplified by the coherent amplitude of the LO field. If some part of the signal field does not overlap then it will not receive this gain and will be unmeasurable, thus acting as a loss source.

Chapter 4

Generation of Squeezed States

This chapter begins by discussing the various methods for producing squeezed states and from there looks at a brief history of squeezing results from cavity systems utilising the second order non-linearity from various materials. The second order process is then described in detail. First, the photon interaction in second harmonic generation is detailed, followed by the optical parametric amplifier and optical parametric oscillator systems. From there, some of the technical issues present in these systems are discussed such as phase matching and intra-cavity dispersion.

4.1 Methods of Squeezed State Production

The first observation of squeezed states was achieved by Slusher *et al.* using a four wave mixing process involving Na atoms in a gas cell [57]. Since then, optical squeezing has been produced in many systems, such as vapour cells [84] and fibres [85]. For many years there was no system that clearly outperformed the others [58], however, one of the stronger performers over the years has been the below threshold optical parametric oscillator (OPO) [58]. Additionally, the parameters of the optical cavity can be tuned for the specific application, providing flexibility. As opposed to three wave mixing processes such as those present in fibre or vapour squeezing, the strength of the second order non-linear interaction, $\chi^{(2)}$, utilised in the OPO is very strong. These properties result in the OPO being a versatile, reliable source of squeezing and currently holds the record for squeezing magnitude, of 12.7 dB [86], and low-frequency performance, 10 dB at 10 Hz [87]. These low-frequency results are presented in Chapter 8. However, squeezing results generated with four-wave mixing experiments are also progressing [88, 89].

4.1.1 History of Optical Parametric Oscillator and Amplifier Performance

A short list of relevant landmark squeezing results from optical cavity systems and some of the details of the systems used to produce these results are shown in Table 8.14.

Table 8.14 shows that the highest level of squeezing measured to date is 12.7 dB at a measurement frequency of 5 MHz [86]. This was achieved in a singly resonant monolithic Periodically Poled Potassium Titanyl Phosphate (PPKTP) cavity. The largest magnitude of squeezing at the lowest frequency is 10 dB at 10 Hz and was achieved in 2012 in a doubly resonant bow-tie cavity also using PPKTP. This work is presented in § 8.4.5. The same work, presented in this thesis showed squeezing of 11.6 dB down to 200 Hz. Two of the most influential results were the first to observe squeezing at audio frequencies, and the first to achieve a suppression of the shot noise by an order of magnitude. The first

Year	Group	Mag.	Freq.	Cavity	λ [nm]	Material
1986	Wu *et al.* [90]	3 dB	1.8 MHz	Linear	532 & 1064	MgO:LN
1992	Polzik *et al.* [91]	6.0 dB	1.4 MHz	Bow-Tie	856	KNB
1992	Ou *et al.* [92]	3.6 dB	1.1 MHz	Bow-Tie	540 & 1080	KTP
1996	Schneider *et al.* [93]	4.3 dB	5 MHz	Hemilithic	1064	MgO:LN
1998	Schneider *et al.* [94]	6.5 dB	6.5 MHz	Hemilithic	1064	MgO:LN
1999	Lam *et al.* [95]	7.1 dB	3 MHz	Monolithic	1064	MgO:LN
2002	Bowen *et al.* [62]	2.5 dB	220 kHz	Hemilithic	1064	MgO:LN
2004	McKenzie *et al.* [63]	2.0 dB	500 Hz	Hemilithic	1064	MgO:LN
2006	Suzuki *et al.* [96]	7 dB	1 MHz	Bow-Tie	860	PPKTP
2007	Takeno *et al.* [97]	9 dB	1 MHz	Bow-Tie	860	PPKTP
2007	Goda *et al.* [60]	7.4 dB	2 kHz	Linear	1064	PPKTP
2007	Vahlbruch *et al.* [98]	10 dB	5 MHz	Monolithic	1064	MgO:LN
2010	Mehmet *et al.* [99]	11.5 dB	5 MHz	Monolithic	1064	MgO:LN
2010	Eberle *et al.* [86]	12.7 dB	5 MHz	Monolithic	1064	PPKTP
2011	Khalaidovski *et al.* [100]	9.5 dB	3 kHz	Hemilithic	1064	PPKTP
2011	Mehmet *et al.* [101]	12 dB	60 kHz	Hemilithic	1550	PPKTP
2011	Chua *et al.* [102]	8.6 dB	10 Hz	Bow-Tie	1064 & 532	PPKTP
2012	Stefszky *et al.* [87]	10 dB	10 Hz	Bow-Tie	1064 & 532	PPKTP

Table 4.1: A brief list of relevant squeezing results, pioneering squeezing in terms of magnitude, frequency, cavity design and/or wavelength. The magnitude of the squeezing given (Mag.) is the directly observed squeezing level, with no corrections for imperfect detection efficiencies. The λ column indicates the wavelengths resonant in the squeezer, where finesses greater than 5 are considered resonant. The materials used by the various groups are labelled; Magnesium Oxide doped Lithium Niobate (MgO:LN), Potassium Niobate (KNB), Potassium Titanyl Phosphate (KTP) and Periodically Poled Potassium Titanyl Phosphate (PPKTP).

audio frequency squeezing was achieved in 2004 by McKenzie *et al.* in a singly resonant hemilithic cavity using MgO:LN [63]. The first directly observed 10 dB of squeezing below the shot noise level was achieved by Vahlbruch *et al.* in 2007 using a singly resonant monolithic MgO:LN cavity [98].

4.2 The Second Order Non-linearity

The OPO utilises the relatively strong second order non-linear interaction, $\chi^{(2)}$, in order to produce squeezing. We can write the induced polarisation, $\vec{P}$, in a non-linear dielectric medium due to an external electromagnetic wave, $\vec{E}$, as

$$\vec{P} = \varepsilon_0(\chi\vec{E} + \chi^{(2)}\vec{E}^2 + \chi^{(3)}\vec{E}^3 + \dots), \tag{4.1}$$

where the $\chi^{(x)}$ terms are the various orders of the non-linear susceptibility and ε_0 is the electric permittivity of free space. The third order susceptibility, $\chi^{(3)}$, is typically orders of magnitude lower than the second order term. It is responsible for four-wave processes such as the Kerr effect, third harmonic generation and self phase modulation [103]. The second order interaction can be used to drive processes such as second harmonic generation (SHG), optical parametric amplification (OPA) and optical parametric oscillation (OPO).

4.3 Second Harmonic Generation

The simplest of these processes is second harmonic generation, or SHG, and as such is a good introduction to the other non-linear processes. Here, only the photon interactions, and as such the energy conservation requirements, are investigated. Consideration of momentum conservation is left until § 4.5. SHG is an up-conversion process, meaning that photons at a lower frequency, ω, combine to produce photons at a higher frequency, in this case at 2ω. It was first experimentally achieved in 1961 by Franken *et al.* [104]. We can write

$$\omega_{sh} = \omega + \omega, \tag{4.2}$$

where ω_{sh} is the frequency of the second harmonic field and ω is the angular frequency of the fundamental field. This process is shown in Figure 4.1. These systems are often placed inside a resonator such that the fundamental field undergoes many passes through the material, substantially improving the conversion efficiency.

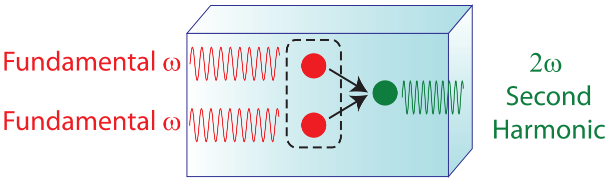

Figure 4.1: The SHG system. Two photons at frequency ω combine to produce one photon at frequency 2ω.

4.4 Downconversion Processes

Downconversion processes are ones in which pump photons are converted into lower energy photons. Although the basic setup is similar, we can identify three different downconversion modes of operation for our system, depending upon how the process is seeded. These are the degenerate optical parametric amplifier, the non-degenerate optical parametric amplifier, and the optical parametric oscillator. These various modes of operation are integral in squeezed state production from a second order system.

4.4.1 The Degenerate Optical Parametric Amplifier

It is often easier to first consider the more intuitive case of the DOPA before moving onto describing the processes in the OPO. The difference between the two, as shall soon be made clearer, is the presence of a bright seed field. The OPA is capable of producing exotic quantum states of light but in this instance we will only investigate the classical behaviour. The quantum behaviour will follow in the treatment of the OPO.

Figure 4.2 depicts the DOPA and the processes involved. The presence of the seed field, also known as the signal field, can be thought of as a catalyst for the reaction of the pump photon downconversion. In the DOPA these two frequencies are equal. We write

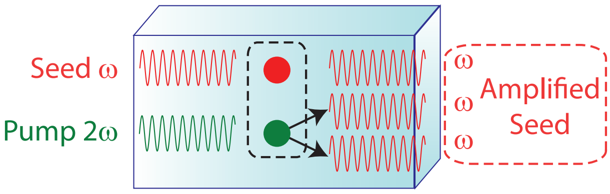

Figure 4.2: The degenerate optical parametric amplifier (DOPA). The system is driven with a pump field at frequency 2ω and a seed field at frequency ω. Inside the non-linear medium, the presence of a seed photon causes the pump photon to split into two photons of frequency ω, thus amplifying the seed field.

for the energy, E, of the process,

$$E \propto \omega_{pump} = \omega + \omega. \tag{4.3}$$

An idealised picture of the process is shown. In reality, only a portion of the pump photons will undergo the downconversion process. The remaining light will exit the system and is known as the residual pump. In many applications, the portion of the pump that is converted is very small due to the relative magnitude between the seed and pump fields, and an approximation is made that the power of the pump field is constant. Conservation of momentum must also be achieved and this is done through a technique known as phase matching, introduced in § 4.5.

Explicitly writing the origin of the two incident fields at angular frequencies of ω and 2ω as ω_{pump} and ω_{seed} respectively, the combined field present on the non-linear dielectric, $\vec{E}_{inc}(t)$, can thus be written

$$\vec{E}_{inc}(t) = \vec{E}_{seed}e^{-i\omega_{seed}t} + \vec{E}_{pump}e^{-i\omega_{pump}t} + \vec{E}^*_{seed}e^{i\omega_{seed}t} + \vec{E}^*_{pump}e^{i\omega_{pump}t}. \tag{4.4}$$

If we look at only the second order term from Equation 4.1 then we can investigate the second order processes involved. Dropping the vector notation on assumption that the two fields are co-propagating we can write

$$\begin{aligned}\chi^{(2)}E^2_{inc}(t) \quad = \quad & \chi^{(2)}[E_{seed}E^*_{seed}e^{-i2\omega_{seed}t} + E_{pump}E^*_{pump}e^{-i2\omega_{pump}t} + \\ & 2E_{seed}E_{pump}e^{-i(\omega_{seed}+\omega_{pump})t} + \\ & 2E_{seed}E^*_{pump}e^{-i(\omega_{pump}-\omega_{seed})t} + \\ & 2(|E_{seed}| + |E_{pump}|)].\end{aligned} \tag{4.5}$$

In the DOPA, the term we are interested in is the difference frequency generation term

$$2E_{seed}E^*_{pump}e^{-i(\omega_{pump}-\omega_{seed})t}, \tag{4.6}$$

which describes the process of amplifying the field at ω_{seed} as seen in Equation 4.3.

4.4.2 The Non-Degenerate Optical Parametric Amplifier

The NDOPA can be used to create exotic states of light, particularly in cases where one might wish to separate the two output modes, such as separable entangled states [105, 106].

Here we only investigate the classical behaviour of the NDOPA. In this case, the frequency of the seed field is shifted from half of the pump frequency by an amount δ.

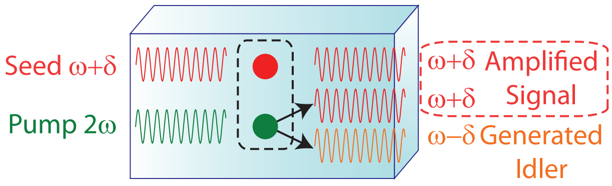

Figure 4.3: The non-degenerate optical parametric amplifier (NDOPA). The system is driven with a pump field at frequency 2ω and a seed field at frequency $\omega+\delta$. Inside the non-linear medium the presence of a seed photon causes the pump photon to split into two photons of frequency $\omega+\delta$ and $\omega-\delta$. This amplifies the seed field but also creates a second field, the idler or generated sideband field.

We see that the defining feature is the generation of the idler field. This field is generated much in the same way as in the DOPA 4.6. The idler field has the same frequency separation as the signal from the carrier, δ, but with a negative sign. This results in a beat signal at the frequency 2δ.

$$E \propto \omega_{pump} = \omega + \delta + \omega - \delta. \tag{4.7}$$

The classical behaviour of the NDOPA is important to the work presented in this thesis because it describes the coherent locking scheme, introduced in § 7.4. This scheme is used to control the vacuum squeezed states produced. In contrast to the DOPA, it is also shown in § 7.4 that the phase of the pump in this system does not affect the output field at the seed frequency, but instead alters the phase of the generated idler field relative to the seed.

4.4.3 The Optical Parametric Oscillator

The optical parametric oscillator can be regarded as an OPA with no bright seed field, or perhaps more informatively, as having a vacuum seed. The OPO is driven by this vacuum seed and by the pump field at 2ω. Vacuum fluctuations can be thought of as the spontaneous production of particle and anti-particle pairs that come into existence and swiftly annihilate. We can imagine that one of these particles seeds the OPO in exactly the same way as the classical seed does, resulting in the downconversion of a pump photon into a photon at the virtual particle frequency, δ, and a photon into the corresponding frequency necessary to conserve energy.

$$E \propto \omega_{pump} = \delta + (2\omega - \delta). \tag{4.8}$$

If we look at the non-linear response of the system then the relevant term is again the difference frequency generation

$$2E_{vacseed}E^*_{pump}e^{-i(\omega_{pump}-\omega_{vacseed})t} \tag{4.9}$$

where the seed field is now replaced with a vacuum seed term, $E_{vacseed}$. It has previously been mentioned that vacuum fluctuations can be regarded as the creation and annihilation of virtual particle pairs. It has also been mentioned that vacuum fluctuations exist at all frequencies and all spatial modes. What this means is that the vacuum seed frequency term, $\omega_{vacseed}$, in Equation 4.9 is constantly changing as a consequence of quantum mechanics. At some point in time the vacuum fluctuation will cause the pump photon to down-convert to a photon pair with some random frequency separation from the carrier. At the next instant in time, the photon pair will be created with a different frequency separation, but always conserving energy. In this way, the vacuum seed acts to populate all frequencies with these photon pairs. These photon pairs, seeded by the vacuum itself, reduce the quantum noise in the output field and are the source of squeezing.

A list is made detailing the important properties of this system that define the production and the spectral shape of the squeezing that exits the OPO system.

- Squeezing originates from the production of these sideband pairs. These pairs replace the vacuum fluctuations and tend to align in some quadrature and cancel in the orthogonal one. The quadrature where they cancel, and hence where the noise is reduced, is the squeezed quadrature.

- The alignment of the generated sidebands from these photon pairs is a function of the phase of the pump. Hence, relative to a carrier field, we can rotate our squeezing quadrature by rotating the phase of the pump.

- The squeezing as it is produced is equal at all frequencies, limited only by the phase matching range of the material. This is because the vacuum fluctuations are white, existing at all frequencies with equal magnitude. However, the OPO consists of a non-linear medium inside an optical cavity and the optical cavity will shape the squeezing through its spectral response.

- Squeezing is centred around the fundamental frequency. This is because the photon pairs are centred about half of the pump frequency due to conservation of energy.

Figure 4.4 shows the conceptual process of the OPO. Comparison with Figure 4.2 shows that the two systems share similarities.

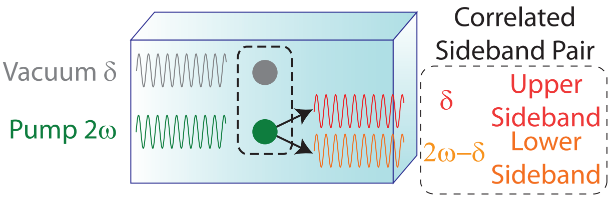

Figure 4.4: The optical parametric oscillator (OPO). The system is driven with a pump field at frequency 2ω and seeded by the vacuum field. Inside the non-linear medium the presence of a virtual photon causes the pump photon to split into two photons of frequency δ and $2\omega - \delta$. This process creates photon pairs across all frequencies.

4.5 Phase Matching

In the previous section, the various non-linear systems and the photon interactions which take place were introduced. Energy conservation was introduced but another quantity also has to be conserved, momentum. The technique of conserving the momentum is known as *phase matching*. The origin of phase mismatch is dispersion within the non-linear medium. In order for phase matching to occur, the wave vector of the pump field must be equal to twice the wave vector of the seed field, which can be written

$$\vec{k}_{pump} = 2\vec{k}_{seed}, \tag{4.10}$$

where $\vec{k}_{pump}$ is the wave vector of the pump field and $\vec{k}_{seed}$ is the wave vector of the seed field. The process typically occurs in a non-linear medium that has been placed inside an optical cavity. The two fields are thus co-propagating and the directional information is not important. We can then write

$$\frac{n_{pump}\,\omega_{pump}}{c} = 2\frac{n_{seed}\,\omega_{seed}}{c}, \tag{4.11}$$

where n_{pump} and n_{seed} are the refractive indices experienced by the pump and seed fields respectively and c is the speed of light in a vacuum.

Using Equation 4.2 we can simplify this to indicate that in order for phase matching to occur, the refractive index of the pump and seed fields must be equal. We can write

$$n_{pump} = n_{seed}. \tag{4.12}$$

The refractive index of the pump field is typically not equal to the refractive index of the seed field and so the phase relationship between the two fields varies, reducing the efficiency of the non-linear processes. Clever techniques are used to ensure that phase matching is satisfied. Figure 4.5 shows the phase relationship between a fundamental wave and its harmonic for the phase matched case and the phase mismatched case, respectively. In the phase matched case, a), the waves have a constant phase relationship whilst in the case where they are not phase matched, b), the waves do not maintain a constant relationship.

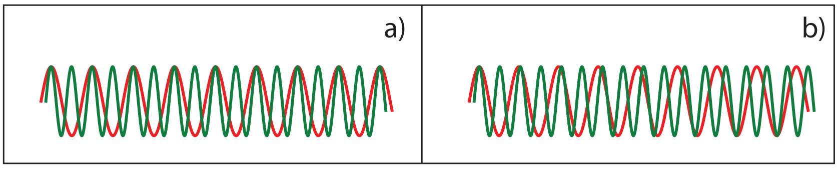

Figure 4.5: Two waves at ω, red, and 2ω, green, when the waves are phase matched a) and phase mismatched b).

We can also illustrate phase matching using a simple phasor diagram. Figure 4.6 shows the resultant second harmonic field in an SHG setup for the phase matched a), quasi-phase matched b) and phase mismatched c), cases. In the phase matched case, a), the wave vectors of the second harmonic and fundamental fields match (See § 4.5.1. In the quasi-phase matched case, b), the wave vectors do not match but periodic poling, marked by the dotted lines, ensures that the process does not reverse (See § 4.5.2). In the final case, c), where the waves are phase mismatched, the energy oscillates between the second harmonic and fundamental fields.

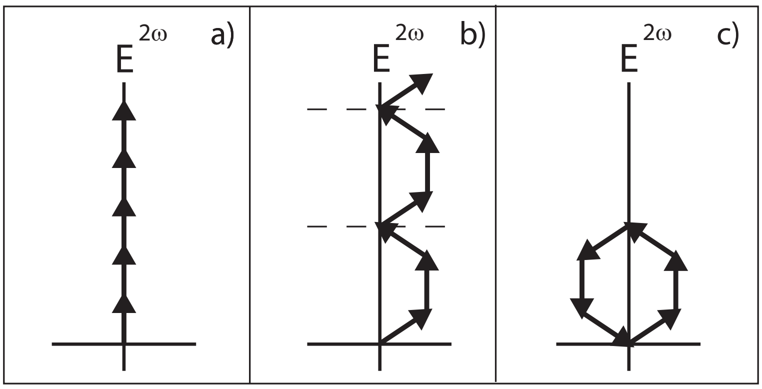

Figure 4.6: Phasor diagrams showing the generated second harmonic field, $E^{2\omega}$ in the phase matched, a), quasi-phase matched, b), and phase mismatched cases in an SHG setup.

4.5.1 Birefringent Phase Matching

One technique commonly used to achieve phase matching is *birefringent phase matching*, illustrated in Figure 4.6. The non-linear mediums used in these non-linear systems are often birefringent. This is in part due to the fact that the crystal has to lack inversion symmetry in order to exhibit the second order non-linearity [75]. The two fields will ordinarily experience non-equal refractive indices depending upon which crystal axis they are polarised along. Rotating the angle of polarization can give any refractive index between the refractive index of the ordinary and the extraordinary axis. These values can be altered by increasing the temperature of the crystal as described by the Sellmeier equation for the material. A crystal cut is then found where varying the angle of the input fields and the temperature of the crystal, will result in an operating regime where their refractive indices match.

The disadvantage to birefringent phase matching is that the angle where phase matching occurs is typically not in the direction of the strongest $\chi^{(2)}$ coefficient. For example, in lithium niobate the non-linear coefficient is 27 pm/V in the d_{33} crystal direction but at the birefringent phase matching angle, which lies along the d_{31} plane, the coefficient is 4.3 pm/V [107]. The conversion efficiency is proportional to the square of the non-linear coefficient for typical applications. Clearly, the birefringent phase matching technique is not harnessing the full potential of this material. Another disadvantage to the birefringent phase matching technique, particularly in this material, is that the temperature at which phase matching occurs cannot be tailored under most circumstances. This leaves lithium niobate with a phase matching temperature of typically around 100 degrees Celsius for a pump field of 532 nm, [108]. It is technically challenging to provide such a temperature environment for the material which is stable.

4.5.2 Quasi-Phase Matching and Periodic Poling

Periodic poling is an alternative method for achieving momentum conservation, one in which the phase matching temperature can be tailored and the largest non-linear coefficent strength of the material can be utilised. This technique does not achieve a phase matching condition within the material, but instead compensates for dispersion by flipping the crystal structure at specific intervals, thus avoiding reversal of the non-linear processes, as illustrated in Figure 4.6. The most common method of achieving domain inversion is *electric field periodic poling.* In this technique, a very strong electric field is applied to metallic "fingers" that are placed on top of the crystal [109]. These large electric fields rearrange the crystal lattice, changing the sign of the non-linear interaction term. The spacing between these fingers and the electric field applied determines the width of the periodic poling.

The distance at which the non-linear process begins to reverse in a phase mismatched system is known as the coherence length and is defined as

$$L_C = \frac{2\pi}{|\Delta k|}, \tag{4.13}$$

where L_C is the coherence length and $\Delta k = \vec{k}_3 - \vec{k}_2 - \vec{k}_1$ is the phase mismatch term, and we have assumed that the fields are co-propagating. The three wavevectors, $\vec{k}_{1,2,3}$ correspond to the wave vectors of the three electric fields that interact in the three-wave-mixing process. For example, in the NDOPA we can write

$$\begin{aligned} \Delta k &= \vec{k}_3 - \vec{k}_2 - \vec{k}_1 \\ &= \vec{k}_3 - \vec{k}_1 - \vec{k}_1 \\ &= \vec{k}_{pump} - 2\vec{k}_{seed} \end{aligned} \tag{4.14}$$

For collinear beams and in a degenerate system, the phase matching condition is equivalent to writing

$$n_{pump} = n_{seed}, \tag{4.15}$$

where n_{pump} and n_{seed} are the refractive indices for the pump and seed fields.

The standard method of poling a non-linear medium is to pole the crystal at intervals equal to the coherence length. This is known as *first order periodic poling.* Sometimes, however, it is technically not feasible to achieve first order poling. This can be due to the non-linear material requiring very large electric fields to facilitate domain inversion or it can be due to a large phase mismatch in a particular crystal direction, which results in a small coherence length [109]. If first order phase matching is not possible then third order phase matching, where the domain is flipped every 3 coherence lengths, can be attempted.

Chapter 5

Optical Cavities

In the following chapter we introduce the framework for the investigation of optical cavities using the standard methods (detailed in such works as[110, 83, 108]) and use this framework to then investigate the theoretical amount of squeezing that the cavity can produce. First, the semi-classical cavity equations of motion are derived for a simple empty, single mode optical cavity. Through simplification of these equations, the classical amplitude and phase response of this cavity are derived. Simple extension of this model allows for the derivation of the semi-classical noise response of the system. From here, the cavity equations of motion are extended to allow for a second field and the exchange of photons between these two fields, facilitated by the second order response of a non-linear medium. The relevant cavity properties and the dependence of these properties upon one another are investigated.

5.1 Cavity Equations of Motion

We begin by introducing the cavity equations of motion for a simple single mode empty cavity. This is a semi-classical approach to the problem in which we describe the time behaviour of the intra-cavity and external fields involved using the methods put forth by Gardiner and Collett [111]. Two partially transmissive mirrors, the input and output couplers, with power reflectivities of R^{in} and R^{out} respectively, and a third mirror representing the loss, $T^l = 1 - R^l$, make up the optical components. The round trip time, τ, defined as the time taken for the light to travel one round-trip of the cavity, is defined as the optical path length, L, divided by the speed of light, c, written

$$\tau[s] = \frac{L}{c}. \tag{5.1}$$

A driving field, A^{dr}, is incident on the input coupling mirror, A^{ref} is the field that reflects off the input coupler and A^{trans} is the field that exits the output coupler. We treat the cavity as an open quantum system, a system into which photons can be added, through a driving field, and photons can be irreversibly lost, through intra-cavity field decay. Cavity decay rates are a measure of the rate at which photons exit, or enter, the system. The decay rate in its entirety is an infinite Taylor expansion, from which only the first two terms are generally retained. This approximation is most accurate for high reflectivities, but for moderate to high reflectivities, it has been shown by White [112] that we can achieve reasonable accuracy by defining the cavity decay rates, κ^x, as

$$\kappa^x[s^{-1}] = \frac{1 - \sqrt{R^x}}{\tau}, \tag{5.2}$$

for any mirror, x. The setup is shown in Figure 5.1.

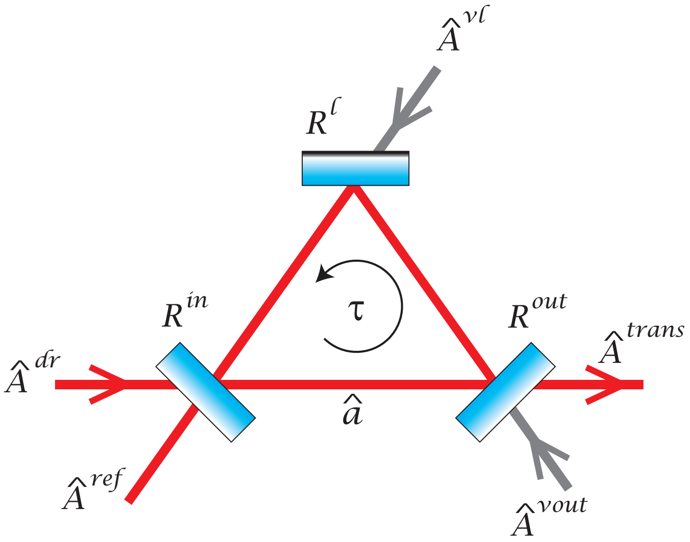

Figure 5.1: The optical cavity. Loss is modelled as transmission through one of the mirrors, $T^l = 1 - R^l$. A driving field, A^{dr}, enters the cavity through the input coupler, R^{in}. The reflected field, A^{out}, consists of the promptly reflected field and the escaping intra-cavity field, the transmitted field consists of the intra-cavity field escaping from the output mirror, with reflectivity R^{out}.

The equation of motion that describes the time evolution of the intra-cavity field, $\hat{a}$, for this system, is written [113]

$$\dot{\hat{a}} = i\Delta\hat{a} - \kappa^a\hat{a} + \sqrt{2\kappa^{in}}\hat{A}^{dr} + \sqrt{2\kappa^{out}}\hat{A}^{vout} + \sqrt{2\kappa^l}\hat{A}^{vl}, \tag{5.3}$$

where $\Delta = \omega_0 - \omega_A$ is the detuning of the driving field, ω_A, from the cavity resonance, ω_0, κ^{in} is the decay rate of the input coupler, κ^{out} is the decay rate of the output coupler, κ^l is the decay rate of the intra-cavity loss, $\hat{A}^{dr}$ is the external cavity driving field, and $\hat{A}^{vl}$ and $\hat{A}^{vout}$ are the external vacuum fields. The total cavity decay rate, κ^a, is defined as the sum of the individual cavity decay rates

$$\kappa^a = \kappa^{in} + \kappa^{out} + \kappa^l. \tag{5.4}$$

The external travelling fields have units of $\sqrt{\frac{\text{photons}}{s}}$ such that $\hat{A}^\dagger\hat{A}$, the number operator, gives the photons per second in the field and is thus proportional to the intensity. The intra-cavity fields have dimensions of $\sqrt{\text{photons}}$ such that $a^\dagger a$ gives the number of photons in the cavity mode.

The power in the external driving field, $\hat{A}^{dr}$, is proportional to the number of photons per second and can be determined via

$$P^{dr}[W] = \frac{\hat{A}^{\dagger dr}\hat{A}^{dr}hc}{\lambda^{dr}}, \tag{5.5}$$

where P^{dr} is the power in the external driving field, A^{dr}, in watts, h is Planck's constant, c is the speed of light, and λ^{dr} is the wavelength of the driving field.

To solve Equation 5.3 we move into the frequency domain by taking the Fourier transform and find

$$i\omega\check{a} = i\Delta\check{a} - \kappa^a\check{a} + \sqrt{2\kappa^{in}}\check{A}^{dr} + \sqrt{2\kappa^{out}}\check{A}^{vout} + \sqrt{2\kappa^l}\check{A}^{vl}, \tag{5.6}$$

where the hats have been replaced with carons, or overturned hats, to signify that these operators are now in the frequency domain. The ω term arising from the Fourier transform is the frequency that a measurement of this state is made at, where a value of $\omega = 0$ indicates a measurement at the carrier frequency of the input field. A non-zero term implies investigation of the system when the cavity is off resonance, or equivalently, the frequency of the laser is shifted from the resonance condition of the cavity. To arrive at Equation 5.6 we make use of the identity

$$\mathcal{F}[\dot{X}(t)] = i\omega X(\omega), \tag{5.7}$$

where $\mathcal{F}[\dot{X}(t)]$ is the Fourier transform of the function $\dot{X}(t)$. Equation 5.6 can now be written

$$\check{a} = \frac{\sqrt{2\kappa^{in}}\check{A}^{dr} + \sqrt{2\kappa^{out}}\check{A}^{vout} + \sqrt{2\kappa^l}\check{A}^{vl}}{\kappa^a + i(\omega - \Delta)}, \tag{5.8}$$

from which the reflected and transmitted fields of the cavity can now be determined. The reflected and transmitted fields are determined using the input/output relations [111]

$$\begin{aligned} \check{A}^{ref} &= \sqrt{2\kappa^{in}}\,\check{a} - \check{A}^{dr} &(5.9)\\ \check{A}^{trans} &= \sqrt{2\kappa^{out}}\,\check{a} - \check{A}^{vout}. &(5.10) \end{aligned}$$

This results in output fields that can be written

$$\begin{aligned} \check{A}^{ref} &= \sqrt{2\kappa^{in}}\frac{\sqrt{2\kappa^{in}}\check{A}^{dr} + \sqrt{2\kappa^{out}}\check{A}^{vout} + \sqrt{2\kappa^l}\check{A}^{vl}}{\kappa^a + i(\omega - \Delta)} - \check{A}^{dr}\\ &= \frac{(2\kappa^{in} - \kappa^a - i\omega)\check{A}^{dr} + 2\sqrt{\kappa^{in}\kappa^{out}}\check{A}^{vout} + 2\sqrt{\kappa^{in}\kappa^l}\check{A}^{vl}}{\kappa^a + i(\omega - \Delta)} &(5.11)\\ \check{A}^{trans} &= \sqrt{2\kappa^{out}}\frac{\sqrt{2\kappa^{in}}\check{A}^{dr} + \sqrt{2\kappa^{out}}\check{A}^{vout} + \sqrt{2\kappa^l}\check{A}^{vl}}{\kappa^a + i(\omega - \Delta)} - \check{A}^{vout}\\ &= \frac{2\sqrt{\kappa^{in}\kappa^{out}}\check{A}^{dr} + (2\kappa^{out} - \kappa^a - i\omega)\check{A}^{vout} + 2\sqrt{\kappa^{out}\kappa^l}\check{A}^{vl}}{\kappa^a + i(\omega - \Delta)}. &(5.12) \end{aligned}$$

5.2 Classical Cavity Phase and Amplitude Response

Now that the equations describing the reflected and transmitted fields have been derived, we will first investigate the classical response of the cavity. This is done by ignoring the terms involving vacuum fields in Equation 5.12, $\check{A}^{vout} = \check{A}^{vl} = 0$. We also assume that the wavelength of the laser matches the resonance condition of the cavity, $\Delta = 0$. The reflected and transmitted fields can then be written

$$\begin{aligned} \check{A}^{ref} &= \frac{(2\kappa^{in} - \kappa^a - i\omega)\check{A}^{dr}}{\kappa^a + i\omega} &(5.13)\\ \check{A}^{trans} &= \frac{2\sqrt{\kappa^{in}\kappa^{out}}\check{A}^{dr}}{\kappa^a + i\omega}. &(5.14) \end{aligned}$$

It was shown in Equation 5.5 that the intensities of these fields are proportional to the number operator. The phases of the fields can be found by taking their arguments. Figure 5.2 shows the classical response of the cavity.

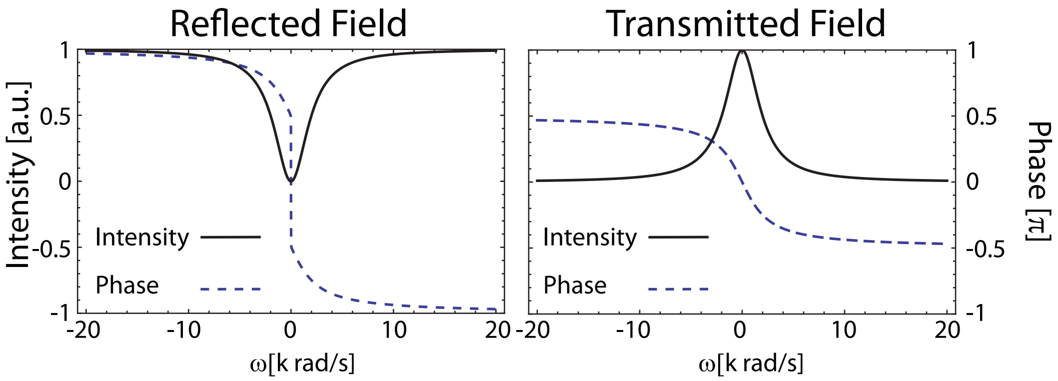

Figure 5.2: The classical response of the two-ended triangle cavity. A critically coupled, lossless cavity is chosen ($\kappa^{in} = \kappa^{out} = 1000$, $\kappa^{l} = 0$)

5.2.1 Circulating Power and Finesse

On resonance, the cavity provides enhancement of the optical field. A relationship between the incident field and the circulating field can be calculated, the result is [114]

$$\frac{P^{circ}}{P^{inc}} = \frac{1 - R^{in}}{(1 - r)^2}, \tag{5.15}$$

where r is defined as the product of the square root of the reflectivity coefficients of all sources of cavity decay, in this case

$$r = \sqrt{R^{in} \times R^{out} \times R^{l}}. \tag{5.16}$$

The enhancement of the field results in a large circulating power. The circulating power is related to another cavity parameter, the finesse. For relatively high mirror reflectivities, we can define the unitless finesse of our cavity as [115]

$$\mathcal{F} = \frac{\pi \sqrt{r}}{1 - r}. \tag{5.17}$$

The finesse is a measure of how efficiently the cavity resonates, which is equivalent to the number of times, on average, that the photons will bounce around the cavity before exiting the system. As can be seen in Equation 5.17, it has no dependence on the length of the cavity. In cavity systems where the intra-cavity loss is much less or similar to the intra-cavity mode loss due to the coupling mirrors, the finesse, although difficult to measure accurately, can provide a good indication of the intra-cavity loss.

The finesse is often used as a means of estimating the circulating power inside a cavity. Figure 5.3 shows the finesse and the circulating power as the power reflectivity of the input coupler is varied. The two values follow a similar trend but using the finesse as an estimate for the circulating power will result in higher circulating power, with the discrepancy between the two values becoming larger as the finesse increases.

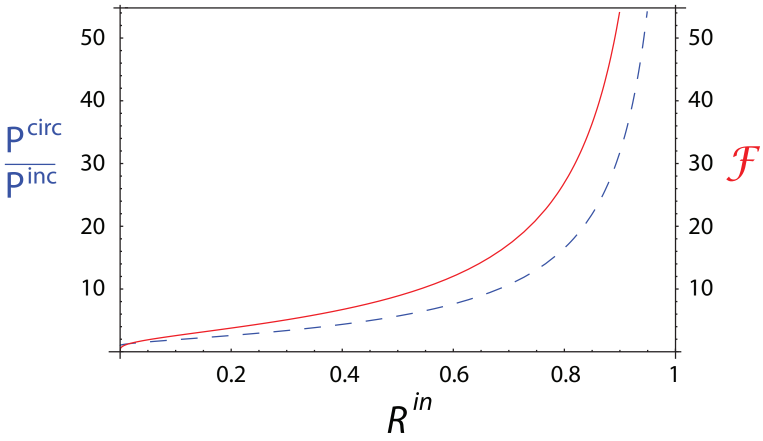

Figure 5.3: The finesse, solid red line, and the circulating power gain, dashed blue line, as the input coupler reflectivity, R^{in}, is varied.

5.2.2 Free Spectral Range

The Free Spectral Range, or FSR, of the cavity is a measure of the spacing between resonances and is defined as [75]

$$\mathrm{FSR[Hz]} = \frac{c}{L}, \tag{5.18}$$

where c is the speed of light and L is the optical path length of one round trip of the cavity. The optical path length is the physical length multiplied by the refractive index of the material traversed through this length.

5.2.3 Linewidth

The linewidth, or Full Width at Half Maximum (FWHM), is a measure of the bandwidth of each resonance of the cavity, it can be defined as the ratio of the FSR to the finesse

$$\Delta_\nu\mathrm{[Hz]} = \frac{\mathrm{FSR}}{\mathcal{F}}. \tag{5.19}$$

This value is important to squeezed light generation because the bandwidth of the cavity limits the bandwidth of the squeezing produced. This is due to the fact that the bandwidth of the non-linear gain is limited by the bandwidth of the cavity. The linewidth also defines the transmission and reflection characteristics of the cavity, which plays a role in how the various locking loops are constructed.

5.3 Semi-Classical Cavity Noise Response

Investigation of Equations 5.12 in their entirety facilitates the analysis of the noise response of the cavity. This analysis includes effects originating from the vacuum fluctuations that enter the system through the various cavity decay mechanisms. The steps towards finding an expression for the noise response of the cavity are as follows; the operators in the cavity equation of motion are first linearised, the quadrature operators are then calculated, and finally, the spectra of the fields are determined.

Linearisation follows the method described in 3.3. Note that the vacuum fields, $\breve{A}^{vout}$ and $\breve{A}^{vl}$, do not have any coherent amplitude and as such, linearisation of these terms results in only the first order fluctuating term. These steps results in

$$\begin{aligned}\breve{A}^{ref} &= \frac{(2\kappa^{in}-\kappa^{a}-i\omega)(\alpha^{dr}+\delta\breve{A}^{dr})+2\sqrt{\kappa^{in}\kappa^{out}}\delta\breve{A}^{vout}+2\sqrt{\kappa^{in}\kappa^{l}}\delta\breve{A}^{vl}}{\kappa^{a}+i\omega} &(5.20)\\ \breve{A}^{trans} &= \frac{2\sqrt{\kappa^{in}\kappa^{out}}(\alpha^{dr}+\delta\breve{A}^{dr})+(2\kappa^{out}-\kappa^{a}-i\omega)\delta\breve{A}^{vout}+2\sqrt{\kappa^{out}\kappa^{l}}\delta\breve{A}^{vl}}{\kappa^{a}+i\omega}. &(5.21)\end{aligned}$$

The next step is to calculate the quadrature operators. These were defined in Equations 3.1 and 3.2 but are written again in the frequency domain for clarity

$$\begin{aligned}\breve{X}^{+} &= \mathcal{F}[\hat{X}^{+}]\\ &= \mathcal{F}[\hat{A}]+\mathcal{F}[\hat{A}^{\dagger}]\\ &= \breve{A}(\omega)+\breve{A}^{\dagger}(-\omega) &(5.22)\\ \breve{X}^{-} &= \mathcal{F}[\hat{X}^{-}]\\ &= i(\mathcal{F}[\hat{A}^{\dagger}]-\mathcal{F}[\hat{A}])\\ &= i(\breve{A}^{\dagger}(-\omega)-\breve{A}(\omega)). &(5.23)\end{aligned}$$

Equations 5.22 have been achieved using the identity [83]

$$\mathcal{F}[\hat{A}^{\dagger}(t)] = \breve{A}^{\dagger}(-\omega). \tag{5.24}$$

These steps result in the quadrature operator equations. All terms without a fluctuating component are dropped because they do not contribute to the noise spectra and all second order terms are removed because, under the assumptions for linearisation (see § 3.3), these terms are small enough to be discarded, resulting in

$$\begin{aligned}\breve{X}^{\pm ref} &= \frac{(2\kappa^{in}-\kappa^{a}-i\omega)\delta\breve{X}^{\pm dr}+2\sqrt{\kappa^{in}\kappa^{out}}\delta\breve{X}^{\pm vout}+2\sqrt{\kappa^{in}\kappa^{l}}\delta\breve{X}^{\pm vl}}{\kappa^{a}+i\omega} &(5.25)\\ \breve{X}^{\pm trans} &= \frac{2\sqrt{\kappa^{in}\kappa^{out}}\delta\breve{X}^{\pm dr}+(2\kappa^{out}-\kappa^{a}-i\omega)\delta\breve{X}^{\pm vout}+2\sqrt{\kappa^{out}\kappa^{l}}\delta\breve{X}^{\pm vl}}{\kappa^{a}+i\omega}. &(5.26)\end{aligned}$$

Finally, we wish to calculate the noise spectra, $V[\omega]$, of these quadrature operators. The noise spectra is defined as the variance of the quadrature operators

$$V[\omega] = \langle \delta\breve{X}^{\dagger}(\omega)\delta\breve{X}(\omega)\rangle, \tag{5.27}$$

for any quadrature operator, $\breve{X}$, in the frequency domain. Calculation of the noise spectra from Equations 5.25 and 5.26 results in

$$\begin{aligned}V^{\pm ref} &= \frac{|2\kappa^{in}-\kappa^{a}-i\omega|^{2}V^{\pm dr}+4\kappa^{in}\kappa^{out}+4\kappa^{in}\kappa^{l}}{|\kappa^{a}+i\omega|^{2}} &(5.28)\\ V^{\pm trans} &= \frac{4\kappa^{in}\kappa^{out}V^{\pm dr}+|2\kappa^{out}-\kappa^{a}-i\omega|^{2}+4\kappa^{out}\kappa^{l}}{|\kappa^{a}+i\omega|^{2}}, &(5.29)\end{aligned}$$

where the variances of the vacuum terms have been replaced with unity, the noise of the vacuum state. Using the fact that $\kappa^a = \kappa^l + \kappa^{in} + \kappa^{out}$, Equations 5.28 and 5.29 can be rearranged to the more succinct forms

$$V^{\pm ref} = 1 + \frac{((2\kappa^{in} - \kappa^a)^2 + \omega^2)(V^{\pm dr} - 1)}{(\kappa^a)^2 + \omega^2} \tag{5.30}$$

$$V^{\pm trans} = 1 + \frac{4\kappa^{in}\kappa^{out}(V^{\pm dr} - 1)}{(\kappa^a)^2 + \omega^2}. \tag{5.31}$$

The cavity noise response given by Equations 5.31 is illustrated in Figure 5.4. It can be seen that, in transmission, the cavity acts as a low pass filter around the resonance frequency. Consequently, the cavity acts as a high pass filter in reflection. Classical laser intensity noise above the characteristic frequency of the cavity can therefore be removed through the use of such a cavity. It can also be seen that the noise does not drop below the quantum noise level (QNL), where the noise is unity. This is a direct consequence of quantum mechanics that arises due to the presence of vacuum fields.

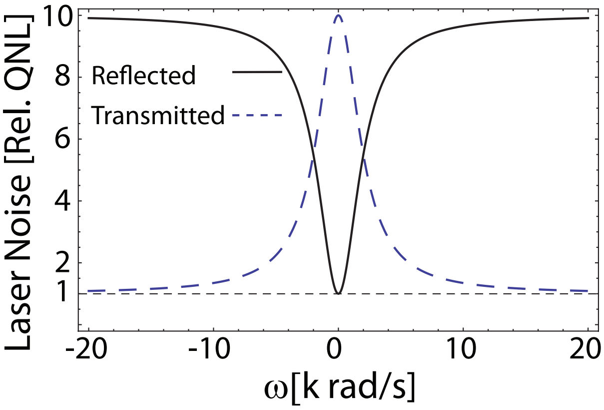

Figure 5.4: The noise response of the optical cavity. A critically coupled, lossless cavity was chosen, $\kappa^{in} = \kappa^{out} = 1000$, $\kappa^l = 0$, and the driving laser field, $\breve{A}^{dr}$, has noise equal to ten times the quantum limit, $V^{dr} = 10$.

5.4 The Optical Parametric Oscillator

By extending the techniques presented up to this point, we can now investigate the squeezing response of an optical parametric oscillator. The next step is to take the equations of motion for the empty cavity (Equation 5.3) and introduce additional fields and a non-linear medium. The non-linear medium facilitates the exchange of photons between the seed and idler fields, A_1 and A_2 respectively, and the second harmonic, or pump field, A_3. The formalisms used here are those introduced by Drummond [110]. We begin by introducing the most general form of the equations that we will require and from these, derive the behaviour of the OPO. In Chapter 6 we will use these equations to investigate coherent locking. The first step is to define the equations of motion for three fields, a pump field and nondegenerate signal and idler fields, in much the same way as shown in

§ 5.1. They are written

$$\begin{aligned}
\dot{\hat{a}}_1 &= i\Delta_1\hat{a}_1 - \kappa_1\hat{a}_1 + g\hat{a}_3\hat{a}_2^\dagger + \sqrt{2\kappa_1^{in}}\hat{A}_1^{dr} + \sqrt{2\kappa_1^{out}}\hat{A}_1^{vout} + \sqrt{2\kappa_1^{l}}\hat{A}_1^{vl} \\
\dot{\hat{a}}_2 &= i\Delta_2\hat{a}_2 - \kappa_2\hat{a}_2 + g\hat{a}_3\hat{a}_1^\dagger + \sqrt{2\kappa_2^{in}}\hat{A}_2^{dr} + \sqrt{2\kappa_2^{out}}\hat{A}_2^{vout} + \sqrt{2\kappa_2^{l}}\hat{A}_2^{vl} \\
\dot{\hat{a}}_3 &= i\Delta_3\hat{a}_3 - \kappa_3\hat{a}_3 - g\hat{a}_1\hat{a}_2 + \sqrt{2\kappa_3^{in}}\hat{A}_3^{dr} + \sqrt{2\kappa_3^{out}}\delta\hat{A}_3^{vout} + \sqrt{2\kappa_3^{l}}\hat{A}_3^{vl}.
\end{aligned} \tag{5.32}$$

Properties relating to the non-degenerate signal and idler fields are written with subscripts 1 and 2 respectively, and the pump field properties with subscript 3. The strength of the non-linear interaction is given by $g\left[s^{-\frac{1}{2}}\right]$ and describes the rate at which photons transfer between fields. The Equations in 5.32 can be used to describe the classical and quantum behaviour of OPO, NDOPA and DOPA systems. Assumptions for various operating regimes can be made which will result in simple analytical solutions to the intra-cavity field solutions. Most treatments of these equations assume that the OPO is not resonant at the pump frequency. This allows for the adiabatic elimination of the pump field, allowing one to assume $\dot{\hat{a}}_3 = 0$. This thesis investigates doubly resonant systems and as such this assumption is generally not valid.

The fact that we are operating the cavity as an OPO does however allow us to simplify the situation in other ways. First, the system is degenerate because it is vacuum seeded, with no coherent amplitude and a variance equal to unity. Finally, we choose to assume that the frequency of our fields match the resonant frequency of the cavity, removing the detuning terms, $\Delta_1 = \Delta_3 = 0$. This results in [110]

$$\begin{aligned}
\dot{\hat{a}}_1 &= -\kappa_1\hat{a}_1 + g\hat{a}_1^\dagger\hat{a}_3 + \sqrt{2\kappa_1^{in}}\delta\hat{A}_1^{dr} + \sqrt{2\kappa_1^{out}}\delta\hat{A}_1^{vout} + \sqrt{2\kappa_1^{l}}\delta\hat{A}_1^{vl} \\
\dot{\hat{a}}_3 &= -\kappa_3\hat{a}_3 - \frac{g}{2}\hat{a}_1\hat{a}_1 + \sqrt{2\kappa_3^{in}}\hat{A}_3^{dr} + \sqrt{2\kappa_3^{out}}\delta\hat{A}_3^{vout} + \sqrt{2\kappa_3^{l}}\delta\hat{A}_3^{vl}.
\end{aligned} \tag{5.33}$$

Although we are operating as an OPO, the coherent amplitude of the seed field, $\alpha_1 = 0$, has not yet been removed because it will be used to illustrate noise couplings in Appendix 1. The next step is to linearise the field operators and remove all second order fluctuation terms and terms that have no fluctuating component. At this point we also make the assumption that the coherent amplitude terms are real. This assumption is valid assuming two things; that the driving fields are real, and that the OPO is operated below threshold. It can be shown that below threshold, the phase of the intra-cavity fields follows the phase of the driving fields [110]. In intra-cavity field units, the threshold of the OPO is defined as

$$a_3^{crit} = \frac{\kappa_1\kappa_3}{g}, \tag{5.34}$$

whilst the external cavity threshold is written

$$A_3^{crit} = \frac{\kappa_1\kappa_3}{g\sqrt{2k_3^{in}}}, \tag{5.35}$$

and the threshold in terms of pump field driving power is written

$$P_3^{crit}[W] = \left(\frac{\kappa_1\kappa_3}{g\sqrt{2k_3^{in}}}\right)^2 \frac{hc}{\lambda_3}. \tag{5.36}$$

The OPO threshold defines a point where the system enters a new mode of operation. It is the point where the round trip loss of the generated field at the fundamental frequency is equal to the round trip gain from the non-linear down-conversion of pump photons into fundamental photons. Operating near to this point, but not over it, produces stronger levels of squeezing as more photon pairs are produced. Above this point, the cavity can behave erratically and new noise couplings are introduced [116].

The next assumption made is that the non-linear interaction term is real. This assumes perfect phase matching within the non-linear medium which relies on sufficient temperature control and is a reasonable assumption for most OPO systems. Making these simplifications and calculating the hermitian conjugate of the intra cavity fields results in

$$\begin{aligned}
\delta\dot{\hat{a}}_1 &= -\kappa_1\delta\hat{a}_1 + g\alpha_1\delta\hat{a}_3 + g\alpha_3\delta\hat{a}_1^\dagger + \sqrt{2\kappa_1^{in}}\delta\hat{A}_1^{dr} + \sqrt{2\kappa_1^{out}}\delta\hat{A}_1^{vout} + \sqrt{2\kappa_1^{l}}\delta\hat{A}_1^{vl}\\
\delta\dot{\hat{a}}_1^\dagger &= -\kappa_1\delta\hat{a}_1^\dagger + g\alpha_1\delta\hat{a}_3 + g\alpha_3\delta\hat{a}_1 + \sqrt{2\kappa_1^{in}}\delta\hat{A}_1^{\dagger dr} + \sqrt{2\kappa_1^{out}}\delta\hat{A}_1^{\dagger vout} + \sqrt{2\kappa_1^{l}}\delta\hat{A}_1^{\dagger vl}\\
\delta\dot{\hat{a}}_3 &= -\kappa_3\delta\hat{a}_3 - g\alpha_1\delta\hat{a}_1 + \sqrt{2\kappa_3^{in}}\delta\hat{A}_3^{dr} + \sqrt{2\kappa_3^{out}}\delta\hat{A}_3^{vout} + \sqrt{2\kappa_3^{l}}\delta\hat{A}_3^{vl}\\
\delta\dot{\hat{a}}_3^\dagger &= -\kappa_3\delta\hat{a}_3^\dagger - g\alpha_1\delta\hat{a}_1^\dagger + \sqrt{2\kappa_3^{in}}\delta\hat{A}_3^{\dagger dr} + \sqrt{2\kappa_3^{out}}\delta\hat{A}_3^{\dagger vout} + \sqrt{2\kappa_3^{l}}\delta\hat{A}_3^{\dagger vl}.
\end{aligned} \tag{5.37}$$

From these equations we can now write the amplitude and phase quadrature operator equations of motion using Equations 3.1 and 3.2. For our purposes, it is sufficient to determine only one of the quadrature operators. It can be shown that the sign of the non-linear interaction term, g, completely determines whether one observes the amplitude or phase quadrature output variances [83]. The amplitude quadrature noise operators can be written

$$\begin{aligned}
\delta\dot{\hat{X}}_1 &= -\kappa_1\delta\hat{X}_1 + g\alpha_1\delta\hat{X}_3 + g\alpha_3\delta\hat{X}_1^\dagger + \sqrt{2\kappa_1^{in}}\delta\hat{X}_1^{dr} + \sqrt{2\kappa_1^{out}}\delta\hat{X}_1^{vout} + \sqrt{2\kappa_1^{l}}\delta\hat{X}_1^{vl}\\
\delta\dot{\hat{X}}_3 &= -\kappa_3\delta\hat{X}_3 - g\alpha_1\delta\hat{X}_1 + \sqrt{2\kappa_3^{in}}\delta\hat{X}_3^{dr} + \sqrt{2\kappa_3^{out}}\delta\hat{X}_3^{vout} + \sqrt{2\kappa_3^{l}}\delta\hat{X}_3^{vl}.
\end{aligned} \tag{5.38}$$

Now we take the Fourier transform of Equations 5.38 to transform the quadrature operators into the frequency domain such that we can determine the spectra. It is important to note that two of these operators are still in intra-cavity units, $\delta\check{X}_1$ and $\delta\check{X}_3$, whilst the rest are in travelling wave units. Taking the Fourier transform results in

$$\begin{aligned}
i\omega\delta\check{X}_1 &= -\kappa_1\delta\check{X}_1 + g\alpha_1\delta\check{X}_3 + g\alpha_3\delta\check{X}_1^\dagger + \sqrt{2\kappa_1^{in}}\delta\check{X}_1^{dr} + \sqrt{2\kappa_1^{out}}\delta\check{X}_1^{vout} + \sqrt{2\kappa_1^{l}}\delta\check{X}_1^{vl}\\
i\omega\delta\check{X}_3 &= -\kappa_3\delta\check{X}_3 - g\alpha_1\delta\check{X}_1 + \sqrt{2\kappa_3^{in}}\delta\check{X}_3^{dr} + \sqrt{2\kappa_3^{out}}\delta\check{X}_3^{vout} + \sqrt{2\kappa_3^{l}}\delta\check{X}_3^{vl}.
\end{aligned} \tag{5.39}$$

We want to solve these equations for the intra-cavity field quadratures, $\delta\check{X}_1$ and $\delta\check{X}_3$. At this point we will set the coherent amplitude of the seed field to zero, $\alpha_1 = 0$, and leave the details of the derivation of the intra-cavity field quadratures for Appendix 1.

The result is that we can write $\delta\check{X}_1$ as

$$\delta\check{X}_1 = \frac{\sqrt{2\kappa_1^{in}}(\kappa_3 + i\omega)}{\alpha_1\alpha_1 g^2 - (g\alpha_3 - \kappa_1 - i\omega)(\kappa_3 + i\omega)} \times \left(\delta\check{X}_1^{dr} + \frac{\sqrt{2\kappa_1^{out}}}{\sqrt{2\kappa_1^{in}}}\,\delta\check{X}_1^{vout} + \frac{\sqrt{2\kappa_1^{l}}}{\sqrt{2\kappa_1^{in}}}\,\delta\check{X}_1^{vl}\right). \tag{5.40}$$

The final steps are to use Equation 5.40 to determine the amplitude quadrature operator for the output field using the input-output relations, Equation 5.9, and then to determine the variance of the output field, using Equation 3.7. From the variance of the amplitude quadrature, one can determine the variance of the phase quadrature. The details of these steps are given in the appendix. The resulting amplitude and phase quadrature variances are

$$V_{out}^{+} = 1 + \frac{4g\kappa_1^{out}\alpha_3}{(\kappa_1 - g\alpha_3)^2 + \omega^2} \tag{5.41}$$

$$V_{out}^{-} = 1 - \frac{4g\kappa_1^{out}\alpha_3}{(\kappa_1 + g\alpha_3)^2 + \omega^2}. \tag{5.42}$$

Figure 5.5 shows the variance in the squeezed quadrature and the variance in the orthogonal anti-squeezed quadrature for various internal losses. The detection frequency, ω, is set to a value of zero because we assume that we are looking at frequencies well within the linewidth of the cavity and hence the filtering behaviour of the cavity is negligible.

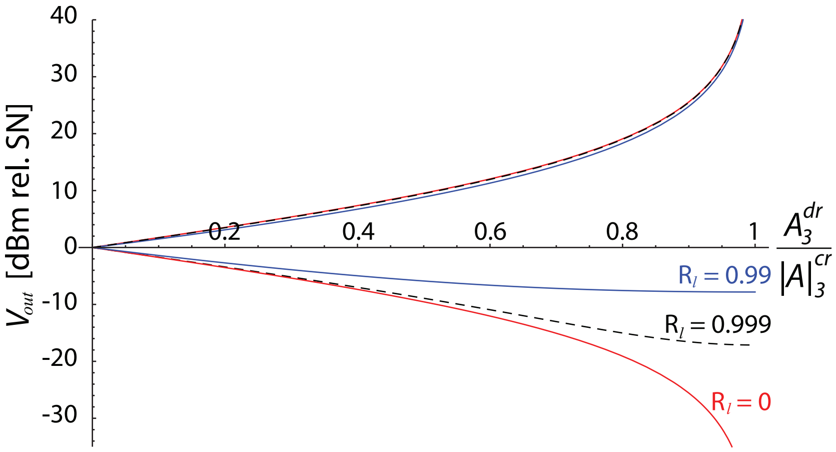

Figure 5.5: The variance of the squeezing and anti-squeezing at the output of an OPO as the system is driven towards threshold power, A_3^{crit}. The variance is shown for the same cavity with varying internal losses of; 0%, shown by the red lines, 0.1%, shown by the dotted black lines, and 1%, indicated by the blue lines. The cavity parameters are; cavity length, $L = 0.3\,\mathrm{m}$, output coupler reflectivity, $R_1^{out} = 0.95$ and input coupler reflectivity, $R_1^{out} = 1$. By setting $R_1^{out} = 1$ we have assumed that the OPO is single-ended for the fundamental field. Note that the losses and coupling reflectivities of the pump are irrelevant because we have normalised to threshold.

Figure 5.5 illustrates a number of important features of the OPO. Firstly, the squeezing gets greater the closer the OPO is to threshold. However, it is important to ensure that the system does not drift above threshold as the system enters a new mode of operation. Second, intra-cavity loss affects the squeezing much more than it affects the anti-squeezing. This is simply due to the fact that the vacuum noise is relatively large compared to the noise of the squeezing but relatively small compared to the noise in the anti-squeezed quadrature. Mixing the state with vacuum therefore results in greater degradation of the squeezing than it does for the anti-squeezing. It is evident that the measured anti-squeezing is thus a relatively good measure of the proximity to threshold of an OPO system.

5.4.1 Escape Efficiency

The escape efficiency, η_{esc}, of an OPO is defined as the ratio of the decay rate of the squeezed field through the output coupler over the total decay rate of the cavity at the fundamental frequency

$$\eta_{esc} = \frac{\kappa_1^{out}}{\kappa_1}. \tag{5.43}$$

The escape efficiency of an OPO limits the maximum amount of squeezing that the system is capable of producing. It is essentially a measure of how many times the intra-cavity field will interact with the loss sources inside the cavity before it escapes through the output coupler. The number of round trips for the squeezed state can be quite high, therefore the intra-cavity field samples this loss many times. The effect of the escape efficiency is shown in Figure 5.6.

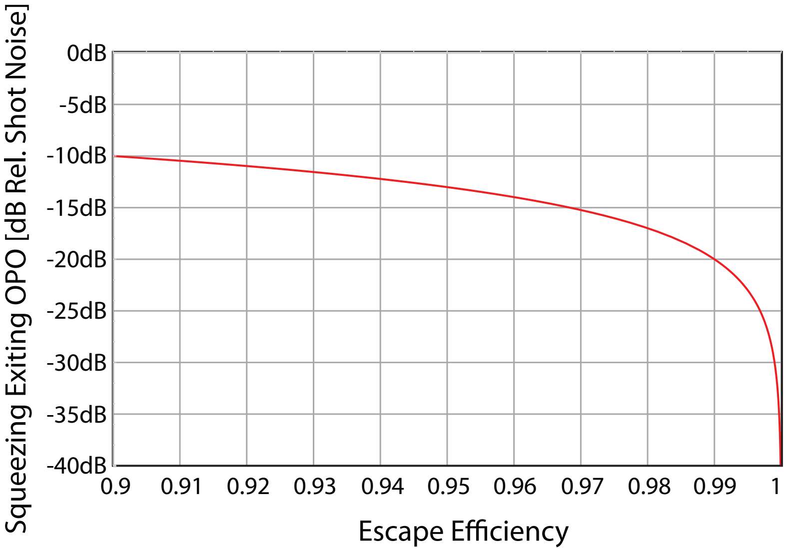

Figure 5.6: The effect of the escape efficiency on the maximum amount of squeezing that can be produced from any cavity.

There are two ways to improve the escape efficiency, one can reduce the intra-cavity losses, or one can reduce the reflectivity of the input/output coupler at the fundamental wavelength. From a design perspective, reducing the intra-cavity losses is achieved by reducing the number of surfaces that the intra-cavity field interacts with. In particular, anti-reflection (AR) coatings, tend to be relatively lossy. In this regard a monolithic cavity, with no internal AR surfaces and one HR coating, is better than a hemilithic resonator, with two AR surfaces and one HR coating per round trip, which is better than a bow-tie cavity, with two AR surfaces and three HR coatings per round trip. However, the major source of loss is often absorption from the non-linear medium. This is why the various cavity designs can currently perform at similar levels. The best AR coatings can have a reflectivity less than 0.01% and the best HR coatings can have a reflectivity greater than 99.999%. Typical non-linear crystals currently have an absorption of approximately 0.1 % per centimetre (See Table 6.2). If advancements in crystal growing techniques result in reduced absorption, then loss from mirror coatings will become the limitation to improving the escape efficiency.

Reducing the reflectivity of the input coupling mirror in order to increase the escape efficiency unfortunately also changes other cavity parameters. Reducing the reflectivity of the input coupler will reduce the finesse of the cavity, which will increase the the linewidth and, more importantly, will also increase the threshold power of the system (this effect is later discussed in § 6.2.2). At some point it will not be possible to provide enough pump power to reach threshold. It has previously shown that the greatest levels of squeezing occur near to threshold and as such it is a requirement that we can produce an adequate amount of pump power. A solution to this problem is to move to a doubly resonant system. This enhances the pump field, reducing the required amount of driving pump power required to reach threshold. This will be explained in detail in § 6.2.1. However, large circulating powers may damage the crystal [117, 118, 119] and can lead to photothermal instabilities [60]. Squeezers typically operate in a regime where the squeezing is maximized whilst the stability of the OPO is kept at a level that is suitable for the application.

The escape efficiency is such an important parameter that it is worthwhile rearranging the squeezed field variances, Equations 5.41 and 5.42, to highlight the effect of the escape efficiency. Doing this results in

$$\begin{aligned} V^+_{out} &= 1 + \eta_{esc}\frac{4g\alpha_3}{\kappa_1(1-\frac{g\alpha_3}{\kappa_1})^2 + \frac{\omega^2}{\kappa_1}} && (5.44)\\ V^-_{out} &= 1 - \eta_{esc}\frac{4g\alpha_3}{\kappa_1(1+\frac{g\alpha_3}{\kappa_1})^2 + \frac{\omega^2}{\kappa_1}}. && (5.45) \end{aligned}$$

Equations 5.44 and 5.45 illuminates the fact that the escape efficiency can be regarded as a beamsplitter operation directly after the OPO. It is often useful to consider the OPO as having produced a pure state which then passes through a beamsplitter of power transmittivity η_{esc}. The escape efficiency is then treated as another loss source on the squeezed state before detection. By treating it this way, it becomes evident that the escape efficiency completely determines the maximum amount of squeezing that a cavity system can produce.

5.5 The Classical Degenerate Optical Parametric Amplifier

Using Equations 5.32 we can also determine the behaviour of the system when operated as a degenerate optical parametric amplifier (DOPA or simply OPA). This is the case when a bright driving field is present at the fundamental frequency. The presence of a bright seed, which may temporarily be injected into an OPO setup, allows one to determine the threshold power of the system through investigation of the amplification and de-amplification of the seed field. The equations describing the classical, degenerate OPA are written

$$\begin{aligned}\dot{\alpha}_1 &= -\kappa_1\alpha_1 + g\alpha_3\alpha_1^* + \sqrt{2\kappa_1^{in}}A_1^{dr} \\ \dot{\alpha}_3 &= -\kappa_3\alpha_3 - g\alpha_1\alpha_1 + \sqrt{2\kappa_3^{in}}A_3^{dr}.\end{aligned} \tag{5.46}$$

At this point we combine the non-linear gain term with the intra-cavity pump field and write $g\alpha_3 = G$. This is done under the assumption that the seed field is much smaller in magnitude than the pump field, $A^1_{dr} << A^3_{dr}$, such that the pump field is not depleted by the parametric process to some approximation. This results in

$$\dot{\alpha}_1 = -\kappa_1\alpha_1 + G\alpha_1 + \sqrt{2\kappa_1^{in}}A_1^{dr}. \tag{5.47}$$

We are looking for the steady state solution, and as such set $\dot{\hat{a}}_1 = 0$ and solve for the intra-cavity field, α, resulting in

$$\alpha = \frac{\sqrt{2\kappa_1^{in}}\,(1 + G/\kappa_1)}{\kappa_1(1 - |G|^2/\kappa_1^2}A_1^{dr}. \tag{5.48}$$

This equation holds only for below threshold operation of the system. We now use the input/output relations given by Equation 5.9 to determine the output field, which is written

$$A_1^{out} = \frac{2\sqrt{\kappa_1^{in}\kappa_1^{out}}\,(1 + G/\kappa_1)}{\kappa_1\left(1 - |G|^2/\kappa_1^2\right)}A_1^{dr}. \tag{5.49}$$

The ratio of output power without the non-linear interaction to the output power with the non-linear interaction can then be calculated in order to determine the parametric gain of the system. Calculating the ratio we find

$$\begin{aligned}\frac{\mathrm{P}_1^{out}}{\mathrm{P}_1^{out}|_{G=0}} &= \frac{A_1^{out*}A_1^{out}}{A_1^{out*}|_{G=0}A_1^{out}|_{G=0}} \\ &= \frac{(1 + G/\kappa_1)^2}{\kappa_1\left(1 - |G|^2/\kappa_1^2\right)}.\end{aligned} \tag{5.50}$$

Noting that the steady state intra-cavity second harmonic field, $\alpha_3 = \frac{\sqrt{2\kappa_3^{in}}}{\kappa_3}A_3^{dr}$, divided by the intra-cavity threshold value, $\alpha_3^{crit} = \frac{\kappa_1\kappa_3}{g\sqrt{2\kappa_3^{in}}}$, results in one of the terms in this expression

$$\frac{\alpha_3}{\alpha_3^{crit}} = \frac{\kappa_1}{G}, \tag{5.51}$$

allows us to rearrange the non-linear gain into an expression written in terms of the external driving fields

$$\frac{\mathrm{P}_1^{out}}{\mathrm{P}_1^{out}|_{G=0}} = \frac{\left(1 + A_3^{dr}/|A_3^{crit}|\right)^2}{\left(1 - |A_3^{dr}|/A_3^{crit}|^2\right)}. \tag{5.52}$$

This expression will later be used to determine the threshold of our cavity systems. By changing the phase of the pump field by 180 degrees, the pump field term, A_3^{dr}, becomes negative and the system moves from amplification of the seed field to de-amplification. This effect is illustrated in Figure 5.7.

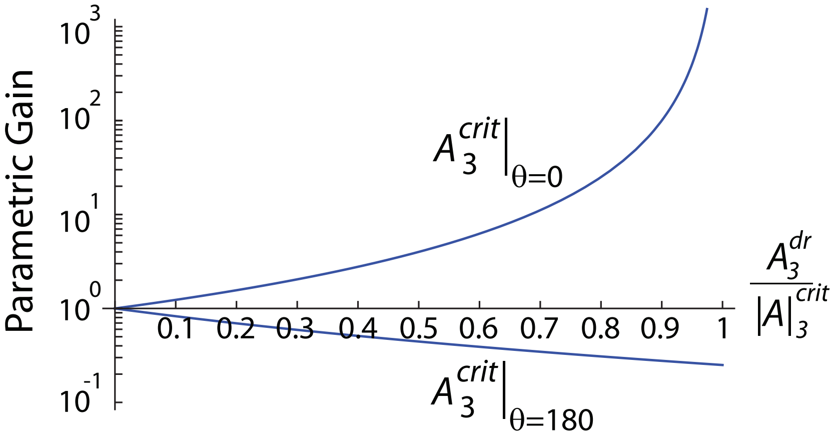

Figure 5.7: Non-linear gain of an OPA system as the input pump power, A_3^{dr}, is driven to threshold, A_3^{crit}.

Chapter 6

The Doubly Resonant Bow-Tie Optical Parametric Oscillator

In this chapter we introduce the details of the doubly resonant bow-tie OPO used to produce the results in this thesis and explain the decisions for arriving at the final design. We investigate the advantages and disadvantages of the various cavity geometries, non-linear media and cavity optical properties. The work in this chapter was undertaken by me in order to determine the optimal cavity design for the LIGO application.

6.1 Cavity Geometry

The first design consideration that we will investigate is the cavity geometry. The cavity geometry affects a number of things; the cavity mode shape, the number of HR and AR surfaces, the number of mirrors available for input and output coupling of external fields and whether the forward and reverse directions in the cavity are degenerate or not. The various cavity geometries are illustrated in Figure 6.1 for clarity.

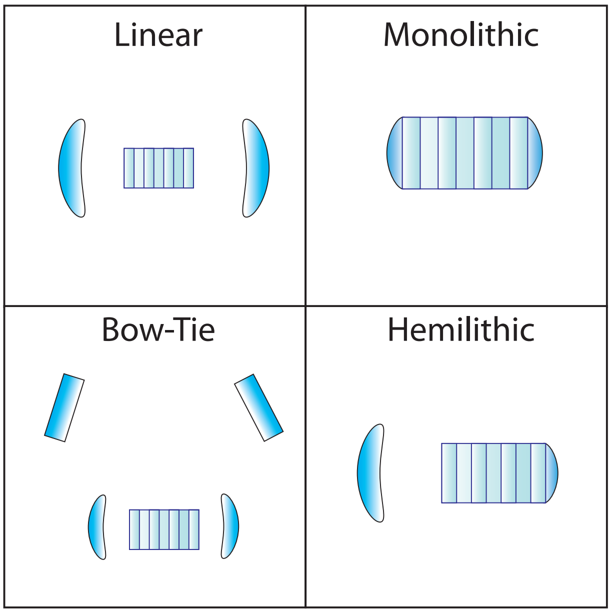

Figure 6.1: The various cavity geometries; linear, monolithic, bow-tie and hemilithic.

6.1.1 Travelling Wave vs. Standing Wave

The first decision we will investigate is whether to choose a standing wave or a travelling wave, ring cavity design. In a travelling wave design the forward and reverse directions of beam propagation exit the cavity at a different angle and hence are non-degenerate. In the standing wave case, light travelling in both the forward and reverse directions occupy the same mode when exiting the cavity. We can see from Figure 6.1 that the bow-tie cavity is a travelling wave cavity and that the three other cavities are standing wave designs.

The standing wave design has three major advantages. The first is the reduced number of surfaces per round trip. As discussed in § 5.6, reducing the number of HR and AR surfaces will reduce the intra-cavity loss and thus increase the escape efficiency. Thus, in theory standing wave cavities, particularly monolithic and hemilithic designs, are capable of producing higher levels of squeezing. However, this is only technically true provided that the loss due to the non-linear medium does not dominate the total intra-cavity loss.

The second advantage to standing wave cavities is that it is easier to make them mechanically stable due to the smaller number of optical elements and a fixed cavity geometry. An example of this is presented by Vahlbruch *et al.* [120], where a very solid modular hemilithic cavity is introduced. By design, the cavity is isolated from both air currents and thermal fluctuations. This aids in both the long term and short term stability of the cavity.

Finally, astigmatism is generally not an issue in these standing wave cavities. Due to the geometry of these cavities, there are no reflections from any curved mirrors which occur at an angle, hence astigmatism does not occur. Astigmatism can make it more difficult to match the mode of the squeezed light to the mode of the interferometer, an issue that should theoretically be relatively easy to overcome, but can also reduce the non-linear coupling between the intra-cavity fields in extreme cases.

The advantages of the bow-tie cavity are flexibility and isolation to backscatter. Access to an increased number of mirrors leaves more locations for the input and output of optical fields, providing flexibility in locking. Also, if a crystal degrades over time then a replacement crystal of the same material can be put in its place in less than a few hours without altering any of the mode matching. If a new material is desired in the setup then the separation of the curved mirrors can be altered to account for changes in refractive index of the non-linear medium and it is theoretically possible to return to a nearly identical cavity geometry.

The second advantage, and the deciding factor in choosing a bow-tie design for the work in this thesis, is the isolation to backscattered light that the travelling wave geometry affords, due to the ability of the cavity to separate the forward and reverse travelling modes. The effect is illustrated in Figure 6.2.

Figure 6.2 shows that scattered light from the interferometer may reflect at the Faraday isolator and thus be directed towards the squeezer. If this light is able to re-enter the interferometer, it will adversely impact on the sensitivity of the device. If the travelling wave cavity in the figure were to be replaced with a standing wave cavity, then virtually all of the scattered light that travels towards the squeezer will reflect off the linear cavity and re-enter the interferometer. This light will pick up random phase shifts as it travels towards the OPO, reflects off it, and travels back into the interferometer. These random phase shifts on the light are detected as a spurious signal. Additionally, this light will seed the OPO, making it operate as an OPA, which will couple pump noise into the squeezed field and degrade the low-frequency squeezing, as discussed in Appendix 1.

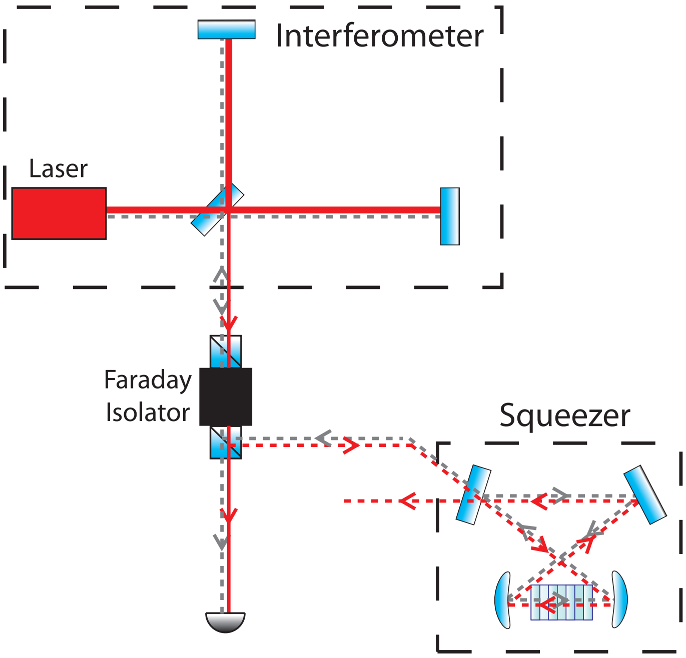

Figure 6.2: Backscattered light from the interferometer, dashed red trace, travelling towards the squeezer. The squeezed state, injected into the interferometer through a Faraday isolator in the signal path, is marked in dashed grey whilst the interferometer laser is marked in red. In the absence of scattering from within the cavity, all of the backscattered light from the interferometer does not re-enter the interferometer.

In order to remove this effect it is necessary to place a number of Faraday isolators between the interferometer and the squeezer. Unfortunately, this adds loss to the squeezed state, reducing the amount of squeezing entering the interferometer. A Faraday isolator can be expected to have an isolation factor of around 40 dB and a loss of anywhere from around 3 to 5 percent. With high levels of squeezing, this loss is substantial, particularly when multiple Faraday isolators are required.

Figure 6.2 shows that with the travelling wave design, the backscattered light from the interferometer will exit the cavity at some angle that does not direct it back towards the interferometer. The scattered light can then be dumped in order to ensure that it does not scatter again and end up being redirected towards the interferometer. Also, light that has scattered at the interferometer and enters the cavity is traversing the cavity in the opposite direction to the pump field and will not seed the OPO process.

However, it is useful to consider the experimental amount of backscattered light rejection that the travelling wave cavity affords. Scatter within the OPO may cause the backscattered light from the interferometer to enter the forward travelling mode of the cavity. If this occurs, then this light will seed the OPO and will be directed back towards the interferometer. The technical limitation to the isolation of forward (direction of propagation of the pump) and reverse modes is scatter off the intra-cavity surfaces, the mirrors and in particular the AR coatings on the crystal. The crystal is very close to normal to the beam direction and near a waist, light that reflects off this surface has a good chance of entering the cavity mode in the forward direction. The amount of isolation between the forward and reverse travelling cavity modes for the ANU squeezer has been measured at

41 dB [102]. This is nearly identical to the isolation offered by a good Faraday isolator. By using a travelling wave design, the loss outside of the cavity can therefore be reduced by an amount equal to the loss introduced by a single Faraday isolator. Different crystal geometries and super-polished cavity mirrors should increase the isolation offered.

6.1.2 Choosing a Bow-Tie Geometry

Due to the advantages detailed previously, it was decided that a bow-tie cavity was the preferred geometry. Using the standard treatment of ABCD matrices we can determine the spatial properties of the intra-cavity field for one of these cavities such that suitable cavity lengths can be found [114]. For Gaussian beams we can fully describe the beam by determining the complex beam parameter, $q(z)$, at some location z relative to the position of the beam waist z_0 as

$$q(z) = z + z_R i = \left(\frac{1}{R(z)} - \frac{i\lambda}{\pi n w(z)^2} \right)^{-1}, \tag{6.1}$$

where λ is the wavelength of the beam, $R(z)$ is the radius of curvature of the phase front, w_0 is the beam waist, n is the refractive index, $w(z)$ is the beam radius at position z and z_R is the Rayleigh range defined by

$$z_R = \frac{\pi w_0^2}{\lambda}. \tag{6.2}$$

The ABCD matrix method allows us to determine a relationship between an input field, and an output field that has undergone a system of optical elements. We can write

$$\begin{pmatrix} q_i \\ 1 \end{pmatrix} = k \begin{pmatrix} A & B \\ C & D \end{pmatrix} \begin{pmatrix} q_o \\ 1 \end{pmatrix} \tag{6.3}$$

for the input and output beam parameters, q_i and q_o, respectively, passing through an optical system with some ray transfer matrix. The k term is merely a normalisation factor to aid in manipulation of the equations. Equation 6.3 allows us to write for the input and output fields

$$q_o = \frac{Aq_i + B}{Cq_i + D}. \tag{6.4}$$

In order for the cavity to resonate, we require our beam at some location to match the shape of the beam after one round trip. This is equivalent to assuming that the beam parameter at some location, the input, is equal to the beam parameter after traversing the cavity once, the output field. Setting this requirement results in a quadratic equation for the complex beam parameter that can be solved in order to determine the complex beam parameter that matches the cavity mode.

From the complex beam parameter, one can then determine any property of the beam. The beam radius at position z is given by

$$w(z) = \sqrt{\frac{\lambda \, \mathrm{Im[q_o]}}{\pi}}, \tag{6.5}$$

where $\mathrm{Im}[q_o]$ is the imaginary part of the complex parameter for the cavity mode.

The ABCD matrices for propagation of distance d through a medium of refractive index

Propagation	**Interface**	**Tangential Reflection**	**Sagittal Reflection**
$M_d = \begin{pmatrix} 1 & \frac{d}{n} \\ 0 & 1 \end{pmatrix}$	$M_i = \begin{pmatrix} 1 & 0 \\ 0 & \frac{n_1}{n_2} \end{pmatrix}$	$M_{rt} = \begin{pmatrix} 1 & d \\ \frac{-R}{2\mathrm{Cos}\theta} & 1 \end{pmatrix}$	$M_{rs} = \begin{pmatrix} 1 & d \\ \frac{-R\mathrm{Cos}\theta}{2} & 1 \end{pmatrix}$

Table 6.1: ABCD matrices for various propagation events.

n, transmission through an interface from a refractive index of n_1 into a material with a refractive index of n_2, and reflection off a spherical mirror with a radius of R are shown in Table 6.1. The reflection off the concave mirror is shown for both the tangential (in the plane of incidence between the ray and the mirror) plane and the orthogonal sagittal plane for a mirror that has an angle of θ relative to the beam axis and the normal direction.

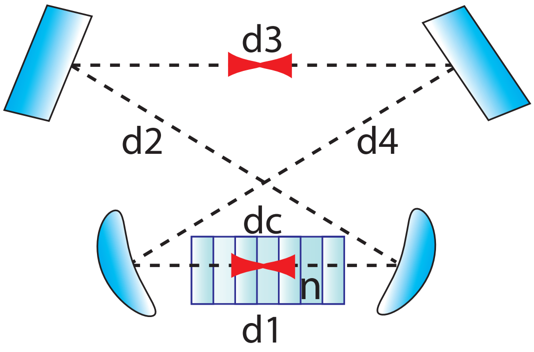

Figure 6.3: The geometry of the bow-tie cavity with the distances involved and the location of the two waists illustrated. The distance through the crystal, of refractive index n, is marked dc whilst d1 is the distance between the two curved mirrors.

The layout of the bowtie cavity is shown in Figure 6.3. The cavity consists of two curved mirrors, focussing the light to a small waist inside the non-linear crystal, and two flat mirrors. The term dc denotes the distance through the crystal whereas the remaining dx terms are used to represent the various distances from mirror to mirror in the cavity, whilst n is the refractive index of the non-linear medium. Reflection off a plane mirror is simply equal to unity. A full round-trip of the cavity for the tangential axis, beginning and ending mid-way through the non-linear medium, can thus be written

$$M = M_{dc/2} M_{i(1\rightarrow n)} M_{(d1-dc)/2} M_{rt} M_{d4} M_{d3} M_{d2} M_{rt} M_{(d1-dc)/2} M_{i(n\rightarrow 1)} M_{dc/2}, \tag{6.6}$$

where it is important to note that the refractive index as the light travels through the crystal, $M_{dc/2}$, must be accounted for and that the two interface terms vary depending on whether the material is exiting or entering the crystal. The same can be written for the sagittal plane, replacing all instances of M_{rt} with M_{rs}. The distances d2 and d4 are equal and can be determined from the angle of the bow-tie

$$d2 = d4 = \frac{d1 + d3}{2\mathrm{Cos}\theta}. \tag{6.7}$$

In order to solve this problem, we need to fix some of these parameters. The method chosen was to set the distance between the two plane mirrors (90 millimetres), the angle of the bow-tie (twelve degrees), the radius of curvature of the curved mirrors (-38 millimetres) and then to vary the distance between the two curved mirrors. The angle of the cavity is chosen to be as small as possible in order to reduce astigmatism but not so small as to make clipping of the beam on mirror mounts an issue. The distance between the two curved mirrors was chosen after varying this value a number of times and finding a region that resulted in a suitable waist size (The waist size can be optimised using the Boyd-Kleinman method [121]). The radius of curvature of the curved mirrors was chosen to provide the necessary focussing to achieve the desired waist size without a large separation between the mirrors. A small radius of curvature is favoured such that the waist size within the crystal is small with a reasonable separation between the two mirrors.

After setting these values we can then plot the radii of the two waists of the bow-tie cavity. One waist is situated between the flat mirrors and the other between the curved mirrors. In order to determine the size of the waist outside the crystal we need only propagate the complex beam parameter through Equation 6.4 with a new transfer matrix that only transfers the beam the required distance. We can write for the propagation matrix, M2, from the crystal waist to the free-space waist

$$M2 = M_{d3/2} M_{d2} M_{rt} M_{(d1-dc)/2} M_{i(n\rightarrow 1)} M_{dc/2}, \tag{6.8}$$

where we note again that the transfer matrices have been applied in reverse order to the order of propagation of the beam.

Figure 6.4 shows the resulting waist sizes. It is evident that astigmatism within the non-linear medium is near zero for some separation between the curved mirrors. There is some astigmatism at the larger waist, situated outside the crystal, and this means that there will be astigmatism on the field exiting the cavity. This is because the portion of light that transmits through the coupling mirror has the same mode shape as the cavity mode and will therefore have an identical waist at the same distance from the mirror, albeit outside the cavity. It is important to remember that the squeezing will have this shape upon exiting the cavity when attempting to mode match the squeezed light to other fields or cavities.

Figure 6.4 shows the waist size for the cavity at the fundamental wavelength of 1064 nm. Due to the fact that we are using a quasi-phase matched system, the refractive indices for the fundamental and the pump fields are different. By changing the wavelength and the refractive index, we can repeat the process followed for the fundamental field to determine the cavity mode for the pump. The result is shown in Figure 6.5

6.2 Cavity Optical Design Considerations

Now that a cavity geometry is decided, the next step is to determine the properties of the mirror coatings. The coatings of the mirrors will dictate the loss dynamics of the optical field within the cavity, defining the escape efficiency, linewidths, finesse and threshold power for the system.

6.2.1 Doubly Resonant System

A choice must be made as to whether the system is operated in a doubly resonant configuration, one in which both the pump and fundamental fields resonate, or in a singly

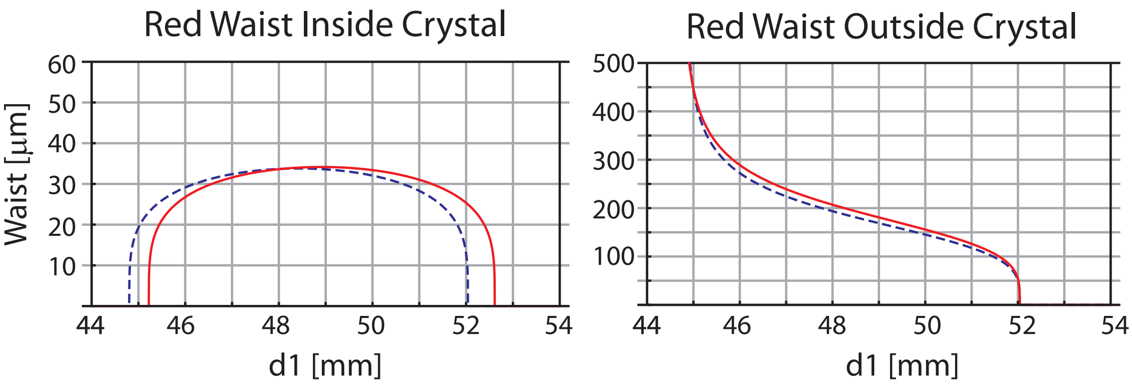

Figure 6.4: The tangential (dashed blue) and saggital (solid red) beam radii of the two fundamental waists in the bow-tie cavity as the distance between the curved mirrors, d1, is varied. The length of the crystal, dc, is 10.5 mm with a refractive index, n, of 1.830 [122]. The distance, d3, is set to 90 mm, the bow-tie cavity has an angle of 12 degrees and the curved mirrors have a radius of curvature of -38 mm.

resonant configuration, where only the fundamental field resonates. The advantages of a doubly resonant system are that the threshold pump power is reduced, the resonant green field provides an additional control field and the optimal spatial overlap between the fundamental and pump fields is ensured.

The optimal overlap between the pump field with waist w_p and fundamental field with waist w_f is given by the relation [121]

$$w_p = \sqrt{2} w_f. \tag{6.9}$$

Investigation of Equation 6.5 reveals that the cavity ensures that, on resonance, this condition is met for the two fields when using a phase matched material. This is not strictly the case for quasi-phase matched materials as will be shown in § 6.3.6. However, Figure 6.5 shows that the slight difference in refractive indices between the fundamental and pump fields has very little impact on the fundamental and pump field modes within the cavity. Figures 6.5 and 6.4 show that, with the correct separation between the curved mirrors, the waist sizes are very well matched, which is to say that Equation 6.9 holds.

As for cavity locking. The fact that the pump field is resonating allows for the pump field to be used as a reference for locking schemes, such as a Pound-Drever-Hall technique. Additionally, the pump field will likely have a different finesse to the fundamental field and may facilitate different modulation frequencies for such a lock.

Finally, the doubly resonant system is a means of reducing the threshold power. The threshold power of the cavity is given by Equation 5.36, but is written again for reference

$$P_3^{crit}[W] = \left(\frac{\kappa_1 \kappa_3}{g\sqrt{2k_3^{in}}} \right)^2 \frac{hc}{\lambda_3}. \tag{6.10}$$

By resonating the second harmonic field, we are decreasing the rate at which photons decay from the cavity, thus decreasing the value of κ_3^{in}. Expanding $\kappa_3 = \kappa_3^{in} + \kappa_3^{out} + \kappa_3^{l}$ in Equation 5.36 will result in a term proportional to $\frac{\kappa_3^{in}}{\sqrt{\kappa_3^{in}}}$, which reduces as the decay

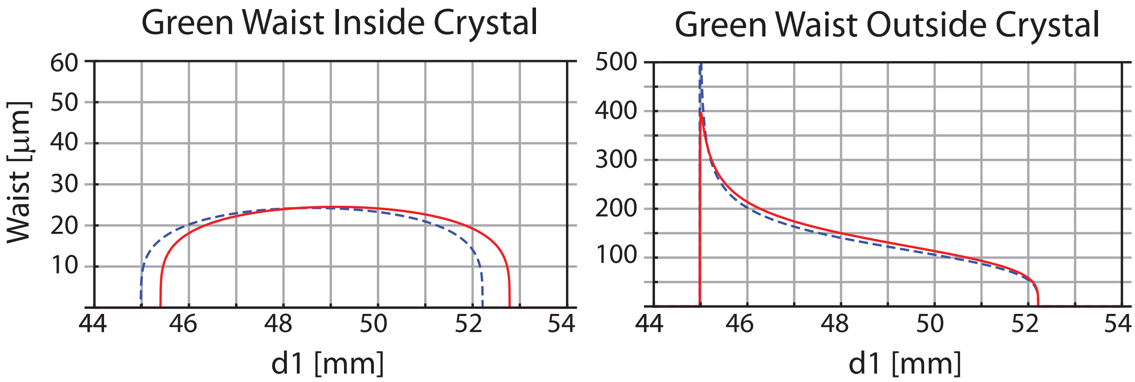

Figure 6.5: The tangential (dashed blue) and saggital (solid red) beam radii of the two pump waists in the bow-tie cavity as the distance between the curved mirrors, d1, is varied. The length of the crystal, dc, is 10.5 mm with a refractive index, n, of 1.830 [123]. The distance, d3, is set to 90 mm, the bow-tie cavity has an angle of 12 degrees and the curved mirrors have a radius of curvature of -38 mm.

rate of the input coupler reduces, thus decreasing threshold power.

The advantage to the singly resonant system is simplicity, and there are alternative solutions to many of the issues that the doubly resonant system offers. Techniques can be employed in singly resonant systems to ensure that the spatial overlap is close to optimal [97]. The threshold power can be lowered by reducing the intra-cavity loss or increasing the reflectivity of the fundamental output coupling mirror, rather than increasing the resonant enhancement of the pump. The phase matching bandwidth, the temperature over which the non-linear interaction is optimised, is also typically larger in the singly resonant case [108]. It is reduced in the doubly resonant system because a temperature shift will result in a differential phase shift on both fields. The cavity length is typically locked through deriving an error signal from one of these intra-cavity fields and hence the cavity will only track the resonance condition of that field. Finally, in the singly resonant system, no techniques are required to ensure that the pump field and fundamental field are co-resonant. Co-resonance is an issue because intra-cavity dispersion shifts the phase relationship between the two fields as they travel around the cavity.

Intra-Cavity Dispersion

The resonance condition of the cavity requires that the phase of a particular field at some location in the cavity be equal to the phase after the field has undergone a complete round-trip and returned to the same location. If the phase relationship between the two fields varies after one round trip then the two fields will now resonate at different cavity lengths. This effect is shown in Figure 6.6

We see that at location 5 the two fields now have a very different phase relationship to that when they started their journey, at location 1. A control loop designed to lock the pump field, for example, will now change the cavity length such that the phase of pump field at location 5 matches the initial phase. However, due to the changed relationship between the two fields, the fundamental field will no longer resonate. If this field is not resonant then many effects arise, but the final result is that squeezing is degraded. With this in mind, it is helpful to resonate the pump field by only a moderate amount, such

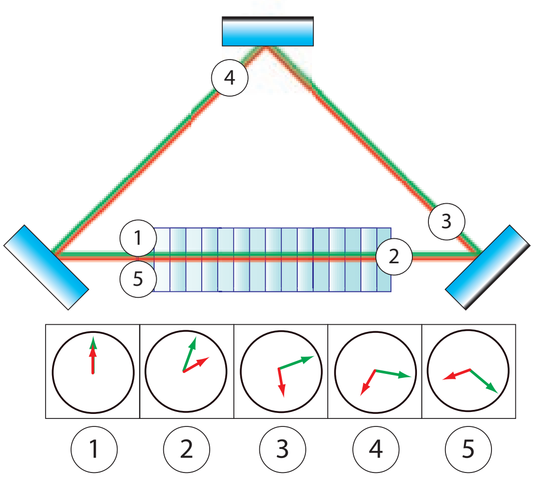

Figure 6.6: Cavity dispersion as the pump and fundamental fields traverse one round-trip of the cavity. As the fields complete one round-trip, they pick up phase shifts from each mirror surface and from the nonlinear medium. As they complete one round trip, from location 1 to location 5, the phase relationship between the two fields has changed.

that the pump field linewidth is much broader than the fundamental field linewidth, such that co-resonance is more easily achieved. By doing this, the sensitivity of the cavity to temperature and length fluctuations is reduced.

Historically, cavity dispersion between the two cavity modes has been overcome by detuning the temperature of the non-linear medium. This allows for dispersion within the material to compensate for dispersion from the various sources of dispersion. In a monolithic geometry, varying the temperature is the only method of overcoming intra-cavity dispersion. This technique is not ideal, as it forces the system away from the ideal phase matching temperature, reducing the efficiency of the non-linear process. The magnitude of this effect is dependant upon the FWHM of the non-linear conversion process, which varies significantly between materials [108].

A simple method for overcoming intra-cavity dispersion is to use a dispersion plate [124]. The dispersion plate is simply a “window” of dispersive material that has been anti-reflection coated at both wavelengths in order to minimise losses. The angle of incidence between this plate and the two fields, inside the cavity, is varied in order to change the path that the two fields travel through the material. By tuning the angle of the plate, a position can be found where the dispersion introduced by the plate compensates for that introduced by the crystal and the cavity mirrors. The disadvantage of this method is the extra loss introduced, decreasing the escape efficiency and hence the squeezing produced. Such a plate might will also likely reduce the forward to reverse direction rejection ratio of the bow-tie cavity.

An alternative method of overcoming intra-cavity dispersion, wedged quasi-phase matched crystals, is described in detail in 6.3.6. This method does not introduce additional loss or scattering into the OPO and allows the non-linear medium to operate at the optimum phase-matching temperature.

6.2.2 Escape Efficiency and the Doubly Resonant System

As mentioned previously, the bow-tie cavity has the disadvantage over other cavity designs of having a relatively larger number of HR and AR surfaces per round trip. This higher intra-cavity loss results in a decreased escape efficiency. The escape efficiency was introduced in § 5.6 and is defined

$$\eta_{esc} = \frac{\kappa_1^{out}}{\kappa_1}. \tag{6.11}$$

Seeing as the losses in the cavity cannot be easily tailored, the remaining means of increasing the escape efficiency is then to increase the decay rate of the output coupler by reducing the reflectivity of the output coupler for the squeezed field. This comes with the unwanted side-effect of increasing the threshold power, given by Equation 5.36. However, the threshold power depends upon the decay rates of both the fundamental and pump fields. By resonating the pump field, thereby decreasing the decay rate of the pump field, the threshold power can be tailored to suit the application. Figure 6.7 uses Equation 5.42 to illustrate the effect on the squeezing produced by the cavity as the reflectivity of the fundamental and pump fields are varied on a singly-ended cavity, $\kappa_1 = \kappa_1^{in/out} + \kappa_1^l$ and $\kappa_3 = \kappa_3^{in/out} + \kappa_3^l$. The sole coupling mirror has a power reflectivity for the pump of $R_3^{in/out}$ and a power reflectivity for the fundamental of $R_1^{in/out}$.

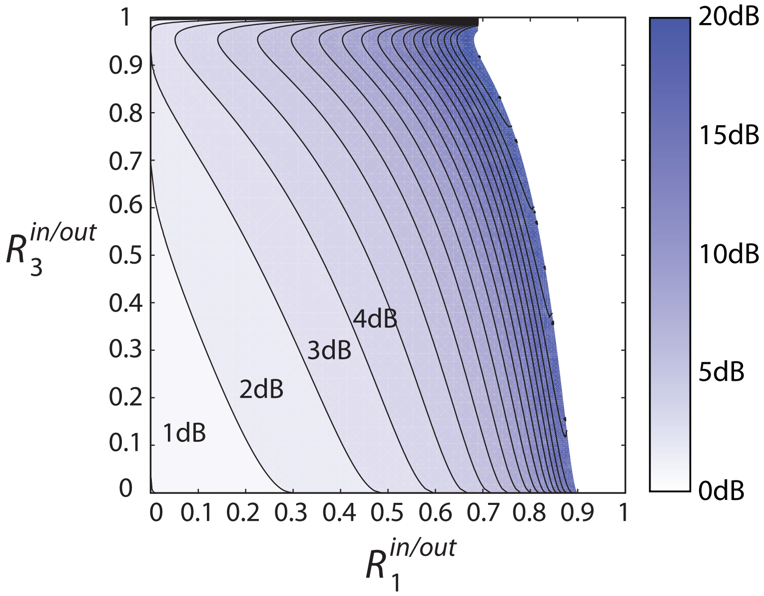

Figure 6.7: Contour plot of the vacuum squeezing produced, in dB relative to shot noise, from a singly-ended doubly resonant OPO cavity as the reflectivities of the input coupler at the fundamental, $R_1^{in/out}$, and pump, $R_3^{in/out}$, wavelengths are varied. The white region in the top right of the figure indicates the region where the system has moved above threshold. Darker regions indicate more squeezing, with each contour indicating an increase of the squeezing by 1 dB. Parameters are; cavity length $L = 0.273m$, non-linear interaction strength, $g = 1891$, intra-cavity loss at fundamental and pump, 0.26% and 4.6%, respectively, detection frequency, $\omega = 0$, and incident pump field power of 100 mW.

It is apparent that as the reflectivity of the coupling mirror at the fundamental is decreased and the escape efficiency increases, more squeezing becomes theoretically available. However, without changing the pump power, it is necessary to increase the reflectivity of the same mirror at the pump such that the incident power stays near to the threshold of the system. This can be seen by tracing the contour that separates the squeezing from the above threshold regime. This type of plot is particularly useful in situations where the maximum amount of pump power is known, as is often the case in experimental setups. The final thing to mention is that this figure does not indicate the amount of circulating pump field power. As the value of $R_3^{in/out}$ is increased, the circulating power also increases, by Equation 5.15. If the circulating power becomes too high then photothermal effects will reduce the stability of the system and may even lead to damage of the non-linear medium. This is explained in more detail in § 6.3.4.

It is important to understand the effect varying one property of the cavity system will have on the other properties. Improving one parameter often leads to the degradation of another. One of the most important and defining properties of the system is the reflectivity of the output coupler at the fundamental wavelength (or input/output coupler in the case of a singly-ended cavity). The interplay between the various parameters that depend upon the reflectivity of the input/output coupler at the fundamental wavelength for a singly ended cavity is shown in Figure 6.8. To find the right reflectivity is a balancing act between the various cavity parameters, particularly the escape efficiency and the threshold power. For example, lower threshold powers are generally preferred because of reduced photothermal effects. However, increasing $R_1^{in/out}$ to achieve this, decreases the escape efficiency and the linewidth, and increases the finesse.

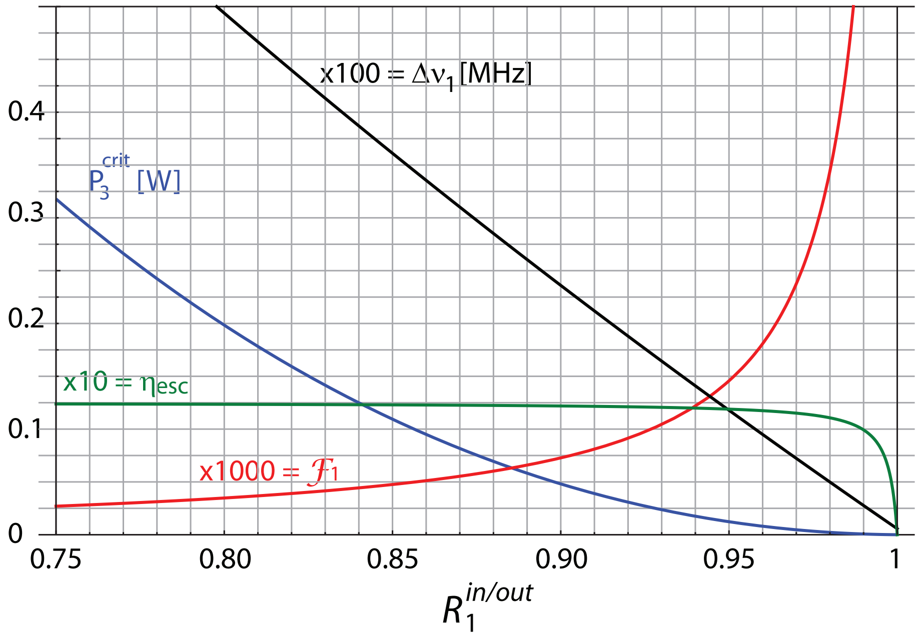

Figure 6.8: The fundamental finesse, $\mathcal{F}_1$, fundamental linewidth, $\Delta\nu_1$, escape efficiency, η_{esc}, and the threshold power P_3^{crit} of the cavity as the reflectivities of the input/output coupler for the fundamental, $R_1^{in/out}$, is varied. Parameters are; cavity length $L = 0.273m$, non-linear interaction strength, $g = 1891$, reflectivity of the input/output coupler at the pump wavelength, $R_3^{in/out} = 0.722$, and intra-cavity loss at fundamental and pump, 0.26% and 4.6%, respectively.

6.2.3 Linewidths and Finesse

The linewidth of the cavity at the fundamental wavelength was tailored specifically for the coherent locking field used. The cavity mirrors and length were chosen such that the linewidth was 25.9 MHz, placing the coherent locking field, which is detuned from the carrier frequency by 29.8 MHz, just outside the cavity linewidth. This will be explained in more detail in § 7.4 but the philosophy was to ensure that the coherent locking field inside the cavity was kept as small as possible. The linewidth of the cavity at the pump frequency was 71 MHz, chosen to be as broad as possible to ensure that the non-linear gain sensed by the coherent locking field was as large as possible. However, increasing the linewidth of the cavity at the pump frequency increases the necessary pump power to reach threshold, and the PDH lock controlling the cavity length on this field performs better with higher finesse, and hence smaller linewidth, cavities.

6.2.4 Threshold Power

As mentioned in the section on escape efficiency (§ 6.2.2), increasing the escape efficiency by reducing the reflectivity of the fundamental coupling mirror, $R_1^{in/out}$, results in a higher threshold power. This effect can be counteracted by increasing the reflectivity of this coupler at the pump frequency. Figure 6.9 has the same parameters as Figure 6.7, but this time shows the threshold power as the reflectivity at the fundamental and pump frequencies is varied.

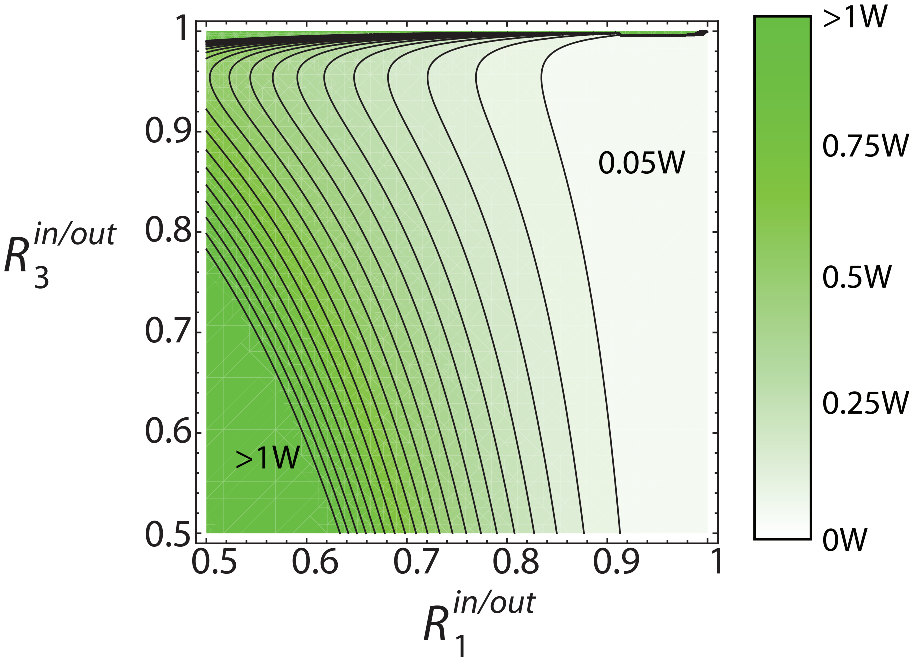

Figure 6.9: Contour plot of threshold power, P_3^{crit}[W], for a singly-ended doubly resonant OPO cavity as the reflectivities of the input coupler at the fundamental, $R_1^{in/out}$, and pump ,$R_3^{in/out}$, wavelengths are varied. Greener regions indicate a higher threshold, with each contour indicating an increase in the threshold power of 50 mW. Parameters are; cavity length $L = 0.273$m, non-linear interaction strength, $g = 1891$, intra-cavity loss at fundamental and pump, 0.26% and 4.6%, respectively.

It can be seen that the threshold power depends very strongly upon the reflectivity of the coupling mirror. As the reflectivity at the fundamental drops below a value of around 0.8, the threshold increases very quickly and the system becomes impractical. Increasing the reflectivity of this mirror at the second harmonic reduces the threshold value but will also increase the circulating power. An operating condition must be found where the escape efficiency and the threshold power are both reasonable.

6.3 Non-Linear Crystal Considerations

There are many choices of non-linear crystals available when building an OPO. The ideal material would possess high non-linear gain, low absorption and a high damage threshold. Below is a summary of the properties of some of the more commonly used periodically poled materials. Many of the absorption values are for materials that have not been periodically poled. A number of experiments have qualitatively found the absorption in periodically poled materials to be nearly identical to those without poling [109]. Multiplying the GRIIRA values by the absorption of the medium in the absence of green light results in the absorption value found in the presence of a 532 nm pump field.

Crystal	**n**	d_{eff} **[pm/V]**	α **[%/cm]**	**Dam. [W/cm^2]**	GRIIRA
PPMgO:LN	2.1494//2.2279	15.9	< 0.1 [125]	> 400 [126]	1 [127]
PPKTP	1.8296//1.8868	9.3	0.02 [109]	89k [128]	7 [109]
PPLT	2.1399//2.2078	8.8	0.1 [129]		1 [125]
PPKN	2.1201//2.2041	12.5	< 0.5 [130]		

Table 6.2: Crystal properties of some of the more commonly used periodically poled materials; the refractive indices, n, non-linear strength, d_{eff}, absorption, α, damage threshold, Dam., and green induced infra-red absorption, GRIIRA. Values for refractive indices and non-linear coefficients are from Shoji *et al.* [122]. Values which could not be found or verified have been left blank.

A periodically poled material was necessary for the cavity because a doubly resonant system was desired and dispersion compensation was to be achieved through the use of a wedged crystal. This is explained in detail in § 6.3.6.

6.3.1 Periodic Poling and Non-Linear Strength

Periodic poling was introduced in § 4.5.2. It is a means of achieving quasi-phase matching within a material. Periodically poled materials typically exhibit larger non-linear interaction strengths than their birefringent matched counterparts due to the fact that the poling can be designed for use with the optimal non-linear coefficient of the crystal. Birefringent phase matching [131], requires cutting the crystal at a particular angle such that the refractive indices of the fundamental and pump fields are equal at some temperature. The temperature at which birefringent phase matching occurs can also be rather inconvenient, as in the case of lithium niobate, whose phase matching temperature is 60 degrees Celsius or higher [108]. With periodic poling the quasi-phase matching temperature can be chosen by varying the domain size of the poling, choosing them to match the coherence length (defined in Equation 4.13) at a particular temperature. The limitation to this is when the domain periods required become too small to physically manufacture.

6.3.2 Absorption and Scattering

As discussed in § 5.6, the loss due to the crystal is often the limiting factor for the amount of squeezing that a system can produce. With this in mind, it is important to choose a non-linear material with as small an absorption coefficient as possible. Table 6.2 shows the expected absorption values for the various non-linear materials. These values are difficult to measure and as such there are limited papers detailing these properties. Quoted values for these materials can vary substantially, and is likely related to the specific growth conditions. This makes it hard to get a good estimate on the actual absorption one might expect. From experience, the loss can also vary greatly between different crystal growth batches. Local defects in the materials can have an enormous impact on the crystal loss. It is often necessary to translate individual crystals and search for the location where the intra-cavity loss is at a minimum.

6.3.3 Green Induced Infra-Red Absorption (GRIIRA)

Many non-linear materials exhibit a property known as GRIIRA. In the presence of green light, the absorption of these materials in the infra-red increases. The phenomenon has been studied in detail for many materials and is believed to be due to the formation of "colour centres" [127, 125, 132, 109]. The infrared absorption for some materials can increase by as much as a factor of 35 in the presence of green light [125] and as such it is worth understanding which materials exhibit this property and how it can be avoided.

Wang [109] meaured the GRIIRA response of KTP and PPKTP after illumination with a 532 nm pump intensity of 320 MW/cm^2. In this material, the absorption of KTP was seen to increase by greater than a factor of 5 and the absorption of PPKTP was seen to increase by greater than a factor of 7. In the absence of GRIIRA the absorption of this material is that quoted in table 6.2, a value of 0.2 %/cm. GRIIRA in lithium niobate was a limiting factor until it became standard practice to dope the crystal with magnesium oxide. Furukawa *et al.* [127] showed that with sufficient doping, GRIIRA could essentially be eliminated from both congruent and stoichiometric growths of lithium niobate.

GRIIRA has been studied well enough that in most commonly used materials GRIIRA is no longer an issue under standard operating conditions. It is worth noting, however, that loss in PPMgO:LN may be less than in PPKTP under high circulating pump fields at 532 nm.

6.3.4 Damage Threshold and Photothermal Effects

The powers used in these experiments are typically very far from the damage threshold of the crystals. With a typical circulating power gain of 10 for the pump field in a doubly resonant system, a threshold power of 200 mW and a waist size of 30 μm, the intensity of the light hitting the non-linear medium is approximately 0.7 kW/cm^2 at threshold. This is very close to the damage threshold of non-doped congruent lithium niobate, at 1 kW/cm^2 [127], but most lithium niobate crystals are now doped in order to increase this value. Doped and/or stoichiometric growths can lead to lithium niobate damage thresholds greater than 8000 kW/cm^2 [127]. For comparison, potassium titanyl phosphate is reported to have a damage threshold of 41 MW/cm^2 [128]. Interestingly, periodic poling can also increase the damage threshold of both KTP and LN [128]. These power levels are generally not reached in OPO setups because photothermal effects, such as lensing and localised heating, from the relatively high absorption of the pump field in most of these materials, will destroy the stability of the OPO well before the large laser powers needed to damage the crystal are ever reached.

6.3.5 Grey Tracking

Whilst the damage threshold of KTP is generally considered significantly higher than that for LN, it can exhibit a phenomenon known as grey tracking. Grey tracking, or photochromic damage, is not completely understood but it is an effect whereby the refractive index of the material and the loss changes after some time of exposure to bright radiation [118, 117, 119]. It has been shown that grey tracking only occurs in the presence of both fundamental and second harmonic fields [117] and that it also occurs in non-degenerate OPA systems. The effect can typically be removed through heating of the crystal, although long term effects of this damage have not been investigated. PPKTP is the only material from Table 6.2 that is known to exhibit this effect.

6.3.6 Wedged Crystal

In doubly resonant cavity systems, in which the pump and the fundamental field are both resonant, cavity dispersion must be overcome. Intra-cavity dispersion is introduced in detail in § 6.2.1. It was discussed that intra-cavity dispersion was historically overcome with the use of a dispersion plate but that this introduces additional intra-cavity losses.

An alternative solution, one that does not introduce additional intra-cavity loss, is to use a wedged quasi-phase matched crystals. This technique exploits the fact that quasi-phase matched materials inherently have different refractive indices for the fundamental and pump fields. At the phase matching temperature, the coherence length matches the poling length, compensating for dispersion. However, dispersion is still present. By leaving a wedged section at the end of the crystal that is free of poling, one can vary the phase relationship between the two fields as they exit the non-linear medium by shifting the crystal laterally to the path of the beams, thus varying the distance travelled through the dispersive medium. In this way, the intra-cavity dispersion can be compensated for such to ensure that the pump and the fundamental fields are co-resonant. The physical parameters of the wedged PPKTP crystals used throughout the work in this thesis are shown in Figure 6.10.

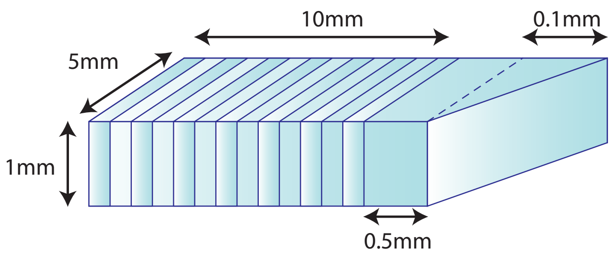

Figure 6.10: The periodically poled wedged crystal. The wedge is cut at an angle of approximately 1 degree.

One thing to note is that the wedge will cause the two fields to undergo different angles of refraction upon entering or exiting the medium due to the different refractive indices of the two fields. Using refractive indices for KTP given in Table 6.2 we can examine the effect that the wedge will have on the propagation of the fields using Snell's law [114]. We choose to investigate only the effect on the pump field. The pump field is propagated through the non-linear medium and the cavity equations are then solved, taking into account the change in angle of incidence of the pump field on the first curved mirror it reflects off. Snell's law is written

$$n_1 \mathrm{Sin}\theta_1 = n_2 \mathrm{Sin}\theta_2, \tag{6.12}$$

where n_1 is the refractive index of air, n_2 is the refractive index of the medium, θ_1 is the angle between the normal of the mirror and the ray in free-space and θ_2 is the angle between the normal and the ray in the crystal. For the pump field we find, with a 1 degree wedge, that the refracted field has an angle of 0.53 degrees. If we then propagate this through the end of the crystal we find that the pump field exiting the crystal has an angle of 0.89 degrees from the normal. The situation is shown in Figure 6.11.

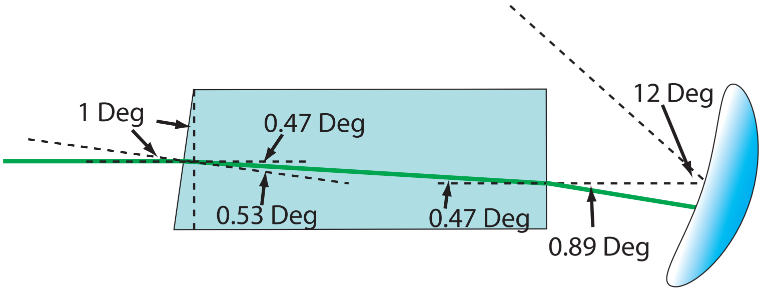

Figure 6.11: Propagation of the pump field through a PPKTP crystal with a 1 degree wedge.

To solve for the intra-cavity field then requires that the θ term describing the angle that the pump field hits the first curved mirror, matrix M_{rt} from Equation 6.6, have the additional angle from the wedge added to it before it. Without the wedge the intra-cavity pump field mode has a tangential waist of 23.81 μm that is 0.14 μm from the centre of the crystal. With the wedge, the pump mode has a tangential waist of 23.01 μm that is 0.55 μm from the centre of the crystal. The results for the sagittal waists are very similar. We therefore conclude that the wedge has only a minor effect on the intra-cavity modes.

Chapter 7

The ANU Squeezer

In this chapter the details of the squeezer that was constructed and operated at the ANU, the prototype for the LIGO squeezer, are discussed. The properties of this cavity are first introduced and the coherent locking scheme, used to control the angle of the squeezing, is modelled using the cavity equations of motion. A variant of the original coherent locking scheme, resulting in improved locking signals, is then investigated. The squeezing results from this system are presented and discussed in Chapter 8.

7.1 ANU Cavity Properties

An overview of many of the design decisions were addressed in Chapter 6 and included cavity geometry, choice of non-linear media, the escape efficiency and the physical distances between mirrors. With these in mind, the properties of the squeezer constructed at The Australian National University, henceforth referred to as the "ANU Squeezer" can be understood. A photo of the cavity is shown in Figure 7.1

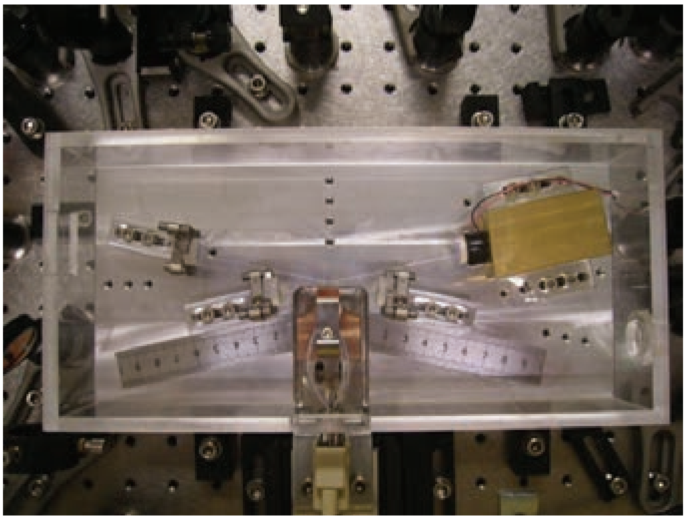

Figure 7.1: The doubly resonant, bow-tie optical parametric oscillator.

The original design for this cavity (the mirror mounts, optical layout, mounting block etc.) originates from the work of Nicolai Grosse for use in a harmonic entanglement experiment [116, 133, 80]. The general design suited our needs because of its modularity, the ability to customise the components and the fact that it was a travelling wave design.

The cavity length is controlled with a lead zirconate-titanate ceramic stack (or PZT). A number of modifications were made to the PZT mount, the crystal holder, the crystal translation stage, and the cavity length to improve upon the original setup. The design allows for easy exchange of non-linear materials, multiple input and output ports, and the ability to alter the mirror separations with ease. The layout of the cavity is shown in Figure 7.2. The design choices taken when constructing the bow-tie cavity were;

- Physical Size - One of the design philosophies was to design the OPO as small as possible after taking all other considerations into account. This was to reduce the bench space required for the device.
- Mechanical Stability - The entire cavity is constructed on a large steel block, shown in Figure 7.1. The steel block at the base of the cavity allows for easy construction and, once completed, shifting of the cavity. It allows the OPO to be a modular device and adds rigidity to the entire device.
- Angle - The folds in the bowtie cavity are designed to have an angle of 12 degrees. This angle is made as small as possible in order to reduce astigmatism. The limit on the reduction of this angle is the cavity size and clipping of mirror mounts by the beam.
- Cavity Length - The cavity length was chosen such that with the smallest angle possible, the mirror mounts would not interfere with the beam paths.

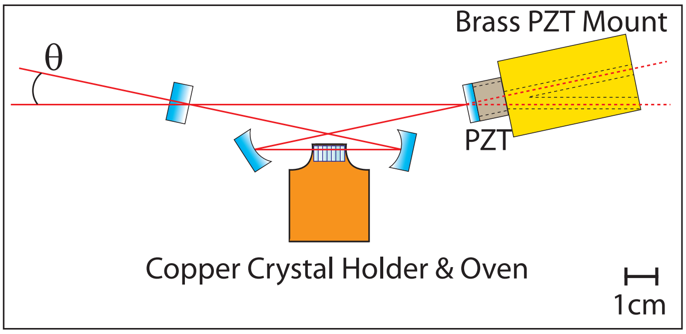

Figure 7.2: To-scale layout of the bow-tie optical parametric oscillator. The bow-tie angle, θ, is 12 degrees and the brass PZT block is cut out to allow for optical access to the back of the mirror attached to the PZT.

Three of the cavity mirrors were provided by Photon LaserOptik; the two curved HR mirrors (with radii of curvature of -38 mm) and the input/output coupler, all half an inch in diameter and 6.35 mm thick. The remaining mirror, from AT Films, was the 99.82 % reflective coherent locking mirror which was half an inch in diameter and 3.2 mm thick to reduce the weight that the PZT had to drive. The PZT is a standard ceramic stack from Piezomechanik, attached using Loctite E-30CL epoxy due to its large Young's modulus, onto a brass block. This block is hollowed such that the input and output ports of this mirror are accessible. This was done after finding that coupling through the curved mirrors had proved difficult in previous cavities. The coatings were all designed for an angle of incidence of 6 degrees to account for the 12 degree cavity angle. The cavity parameters are shown in Table 7.1

Cavity Parameter	**Symbol**	**Value**	**Uncert.**	**Units**
Fundamental Wavelength	λ_1	1064	-	nm
Second Harmonic Wavelength	λ_3	532	-	nm
Input/Output Coupler Fundamental Ref.	$R_1^{in/out}$	0.839	0.001	-
Input/Output Coupler Pump Ref.	$R_3^{in/out}$	0.722	0.001	-
Coherent Locking Mirror Fundamental Ref.	R_1^{cl}	0.9982	0.0002	-
Total Intra-Cavity Loss for Fundamental	T_1^l	0.0026	0.0001	-
Total Intra-Cavity Loss for Pump	T_3^l	0.046	0.001	-
Finesse at Fundamental	$\mathcal{F}_1$	36	3	-
Finesse at Pump	$\mathcal{F}_3$	16.8	0.6	-
Linewidth at Fundamental	$\Delta\nu_1$	31.2	1.5	MHz
Linewidth at Pump	$\Delta\nu_3$	65.3	2.5	MHz
Auxiliary Laser Detuning	Δ_{Aux}	29.8	-	MHz
Optical Path Length	L	0.279	0.001	m
Threshold Power	P_3^{crit}	118.0	0.1	mW
Escape Efficiency	η_{esc}	0.985	0.001	-
Non-linear Coupling Strength	g	1891	9	$\text{s}^{-\frac{1}{2}}$
Curved Mirror Radius of Curvature	RoC	-38	-	mm

Table 7.1: The properties of the ANU squeezer. The loss values given are the transmission values of loss equivalent high reflectivity mirrors. Uncertainties are given for measured values.

The parameters were chosen to optimise squeezing without sacrificing stability. The locking frequencies were chosen to match the frequencies available at the LIGO Hannford site and as such the linewidths of the cavity were tailored, as much as possible, to work with these frequencies. The following sections detail the optimisation of the non-linear medium within the cavity and the two most important measurements for defining the cavity properties, the threshold, which describes the strength of the non-linear interaction, and the intra-cavity loss.

7.1.1 Optimising the Wedged Crystal

Determining the optimum operating conditions of the non-linear medium within the squeezer is non-trivial. The position of the crystal varies the intra-cavity dispersion as well as the loss due to local defects; the temperature sets the phase matching condition; and finally, the pump power determines the amount of localised heating. Figure 7.3 shows the experimental setup used for optimising the crystal parameters within the OPO.

Figure 7.3 shows that both the fundamental (red) and pump (green) fields enter the cavity through the input coupler after combining on a dichroic mirror. The cavity length can be scanned using the PZT attached to one of the cavity mirrors and a second PZT can be driven to scan the relative phase between the fundamental and pump fields. The crystal is located on a translation mount and temperature actuation is available through utilisation of a Peltier device. Photo-detectors are used to detect the transmitted and reflected components of both laser fields. The reflected fields are separated by a second dichroic mirror.

- 1) The bottom half of 1) in Figure 7.4 shows that the crystal was set up such that the fields travelled through it at one edge to provide a position reference. The pump power was then set to the expected final operating pump power so that localised

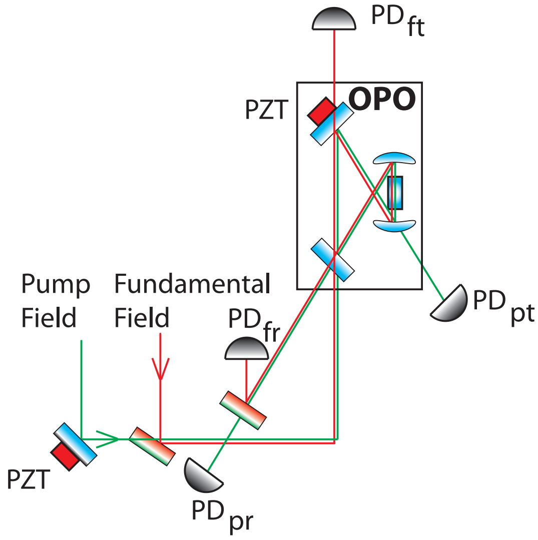

Figure 7.3: Schematic of the experimental setup used to optimise the crystal parameters within the OPO. PZT - piezo-electric transducer, PD_{ft} - transmitted fundamental field photo-detector, PD_{fr} - reflected fundamental field photo-detector, PD_{pt} - transmitted pump field photo-detector, PD_{pr} - reflected pump field photo-detector.

heating due to absorption from the pump was factored into the optimisation. A theoretical value for the threshold, allowing one to estimate the expected operating pump power, can be found using the technique described by Boyd and Kleinmann [121] or alternatively, one can estimate values from previous experiments by using information such as that shown in table 7.1. The top half of 1) illustrates the pump (green) and fundamental (red) fields detected on PD_{pt} and PD_{ft} photo-detectors respectively, as the cavity length was scanned. At this point, the temperature of the crystal had been set to the phase matching temperature specified by the manufacturer, of approximately 35 degrees Celsius. At this temperature, the two fields resonated at different cavity lengths.

- 2) To tune the dispersion such that the cavity was co-resonant for both circulating fields, the crystal was displaced relative to the circulating fields as shown in the bottom half of 2) in Figure 7.4. The crystal was translated until the transmitted fields, as monitored on PD_{pt} and PD_{pt}, showed that both fields were resonating at the same cavity length.

- 3) The co-resonance condition found by following the previous steps provides only a rough estimate for co-resonance. This is mainly due to the fact that co-resonance has been found as the cavity was being scanned and therefore the pump field, which causes localised heating and thereby introduces dispersion, does not have enough time to reach an equilibrium within the cavity. Additionally, it is not strictly co-resonance that one need to concern themselves with. To optimise the amount of squeezing, the non-linear interaction strength is the parameter that must be optimised. To optimise this, and to remove dynamical effects, the non-linear gain was then measured. This involved locking the cavity length, reducing the fundamental field power, and scanning the phase of the pump field using the second PZT. These

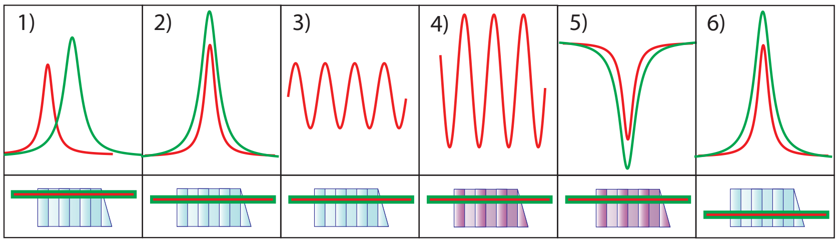

Figure 7.4: Schematic of the procedure used to optimise the temperature and position of the non-linear crystal. The top row illustrates the modelled signals (not to-scale) from various photodetectors for the fundamental (red) and pump (green) fields (the magnitude of these signals is arbitrary and the x-axis is time). The bottom row shows the position of the laser beam through the crystal inside the cavity. Different colours for the crystal represent that the crystal temperature has changed. Full description in text.

steps are described in further detail in § 7.1.2. The signal on $\mathrm{PD_{ft}}$ then shows the non-linear gain of the fundamental field as the relative phase between the fundamental and pump fields was scanned.

- 4) To optimise the non-linear gain, the temperature of the crystal was then adjusted until the largest amount of gain was seen. The non-linear gain is recorded (as described in § 7.1.2.

- 5) Although the maximum non-linear interaction had then been determined, another parameter must also be addressed, loss within the crystal. The loss can change by very large amounts as the crystal is translated due to local defects in the crystal. Therefore the loss at this crystal position was measured, by unlocking and then scanning the cavity length and analysing the reflected field signals detected by $\mathrm{PD_{pr}}$ and $\mathrm{PD_{fr}}$. The process is quite involved and so a detailed description is left for § 7.1.3.

- 6) The locally optimised non-linear interaction strength and the intra-cavity loss were then known for some position within the crystal. However, the crystal wedge was designed such that there were at least 3 locations where the beams could enter the crystal, at the phase matching temperature, and be co-resonant. The entire process was then repeated for these other locations, found by tuning the crystal to the phase matching temperature and translating the crystal to where the two fields were seen to co-resonate again. The entire process was then repeated, eventually resulting in a known crystal displacement with the lowest loss and highest non-linear interaction strength. The system was then brought back to this operating regime.

7.1.2 Measuring Threshold

The setup for measuring the non-linear gain of the OPA system is shown in Figure 7.5.

First, the pump field is blocked such that it does not enter the cavity, and the temperature of the non-linear crystal is set to approximately 20 degrees above the phase matching temperature (specified at approximately 35 degrees Celsius). The fundamental field enters the cavity, resonates and some portion is then transmitted through the cavity. This transmitted field reflects off a dichroic mirror, and is then detected on the photo-detector.

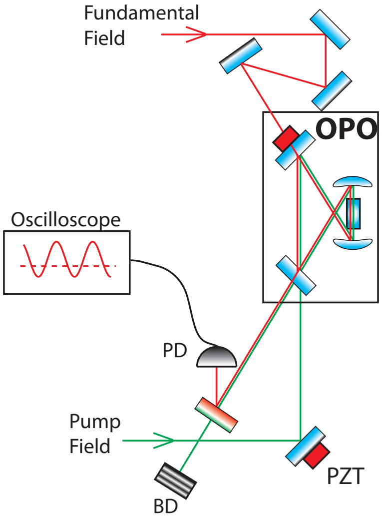

Figure 7.5: The setup for measuring the parametric gain. PD - Photo-Detector, BD - Beam Dump, PZT - Piezo-Electric Transducer.

This signal is measured on an oscilloscope and sets a reference level for the amount of transmitted cavity light in the absence of non-linear gain. Next, both the fundamental and second harmonic fields are made to enter the cavity and the temperature of the non-linear crystal is tuned to near phase matching. By scanning the phase of the pump field, using the piezo, the system is driven through amplification and de-amplification of the fundamental field (See § 5.5). The output field, consisting of light at both wavelengths, is then incident on a dichroic mirror, separating the two fields. The intensity of the fundamental field is once again detected on an oscilloscope. The resulting signal is a sinusoid showing the non-linear gain on the fundamental field. The amount of amplification and de-amplification is maximised by tuning the temperature of the crystal. By taking the ratio of the maximum and minimum voltage values of this sinusoid, with the initial reference value, one can determine the non-linear gain in both the amplification and de-amplification regimes respectively. By taking these measurements for many different pump powers, the threshold can be determined by using the theory introduced in § 5.5. The results for the ANU squeezer are shown in Figure 7.6.

The incident pump power was multiplied by the mode matching of this field to the cavity in order to get a more accurate figure on the amount of light that will actually enter the cavity and undergo cavity enhancement. The proportion of light that does not match the cavity mode simply reflects off the coupling mirror. The best fit to this data resulted in a threshold power of 118 mW for the amplification regime and a threshold of 85 mW for the de-amplification regime. The discrepancy is likely due to the fact that de-amplification is much harder to measure accurately. The signal to noise ratio is smaller because of the signal size and thus noise sources can add systematic offsets if not properly accounted for. With this in mind it was assumed that the amplification regime provided the best estimate and concluded that the squeezer had a threshold of approximately 118.0 ± 0.1 mW. Using this threshold power and the mirror properties in Table 7.1, Equation 5.36 can then be solved for the non-linear coupling term, g, to determine a value for the non-linear coupling term of $1891 \pm 9\,\mathrm{s}^{-\frac{1}{2}}$.

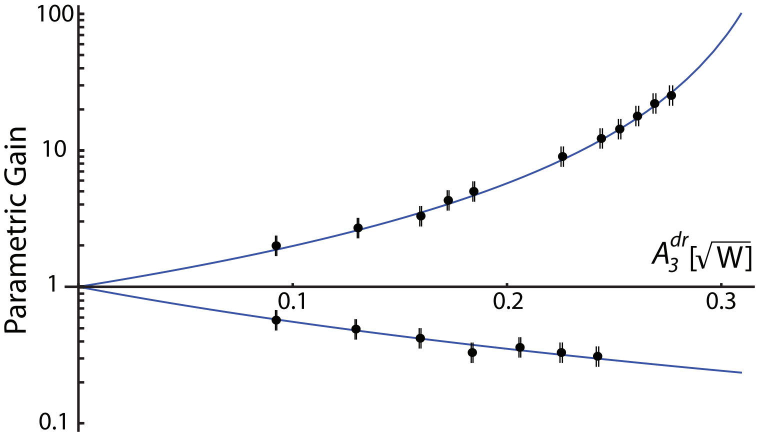

Figure 7.6: Parametric gain as a function of pump amplitude for the ANU squeezer. The points are the data and the blue curve is the best fit to Equation 5.52.

7.1.3 Measuring Intra-Cavity Loss

It has been emphasised many times that the total losses in the cavity, arising from sources such as scatter, absorption and non-unity mirror reflectivities, limit the amount of squeezing that can be produced. To get a reasonable understanding of the experiment, it is therefore necessary to characterise the intra-cavity losses as accurately as possible.

The simplest method to get an estimate for the intra-cavity losses is to measure the transmission of the individual components within the cavity, the mirrors and the crystal, in a single-pass setup. Whilst this will give a rough estimate on the losses, this method cannot provide information on scatter or absorption and the single-pass experiment cannot mimic the exact conditions in the cavity. Local defects, in particular within the non-linear medium, but also from defects in the mirror coatings, are spatially dependent and thus depend upon the beam radius as it interacts with the various loss sources, as well as the positioning of these beams on the mirrors and the positioning through the crystal. The cavity samples these loss sources many times before exiting the cavity so a method of measuring loss that utilises this fact can provide a more accurate measure than single-pass techniques.

Perhaps the most common method for determining intra-cavity losses is to measure the finesse of the cavity. Equation 5.17 shows that the finesse is dependant upon both the coupler reflectivity and the intra-cavity losses. The first step is to determine the properties of the coupler, specifically the power reflectivity. Measuring the transmissivity of an individual mirror, such as the coupler, is simple provided that the mirror is not highly reflective. This is a relative measurement (between input and output powers) and as such, any systematic error from the power meter is subtracted. If the reflectivity of the coupler were much higher, as is the case for the cavity HR mirrors, then the power reflectivity must be inferred from the transmission. By doing this, one must assume that loss from scatter and absorption is negligible, which is often valid, but as the reflectivity of the mirror increases, these effects become more important.

Now that the reflectivity of the input coupler is known, we can infer the losses of the OPO. Note that we infer the total losses of the intra-cavity system, and also that the process by which the loss occurs (such as scatter or absorption) is of no importance because they all have the same effect on the intra-cavity field. We assume a single-ended cavity, feed a field at the fundamental frequency into the input/output coupler and investigate the reflected light as the cavity resonance frequency is scanned. Figure 7.7 shows the power of the reflected field for various intra-cavity losses, using Equation 5.14.

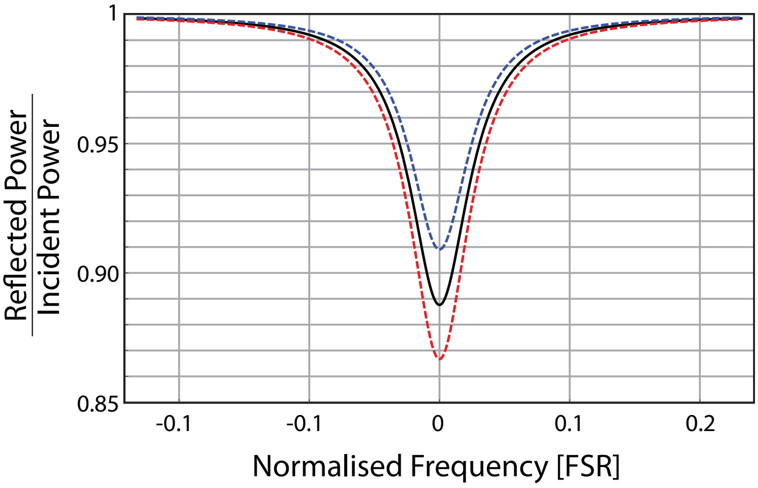

Figure 7.7: Theoretical fundamental field power response ratio of a singly-ended OPO (off phase matching). The cavity resonance conditions is scanned and the response is shown for 3 values of the total intra-cavity loss; 0.5% as the solid black line (finesse of 34.8), 0.4% as the dotted blue line (finesse of 34.6), and 0.6% as the dotted red line (finesse of 35.0).

Figure 7.7 reveals that the finesse is a poor measure of the loss. It is evident that the linewidth of the cavity response varies minutely as the intra-cavity loss changes. The reason for this is evident in how the finesse is defined, see Equation 5.17. By measuring the finesse, we are trying to measure a change in reflectivity of 0.1% on top of a reflectivity of 85% from the input/output coupler.

Additionally, resonance is typically scanned by driving a PZT. This needs to be done over an entire free spectral range in order to evaluate the finesse 5.2.3. The response of these PZTs is not linear, particularly not over a large scanning range [134]. So not only is the signal small, but the non-linear response of the PZT results in a completely unreliable measurement.

Figure 7.7 shows that the power of the reflected field on resonance is a much more sensitive measure of the intra-cavity loss. Working from Equations 5.14 we can determine the reflected power on resonance as a function of the cavity decay rates. We drop the operator notation as we are only interested in the classical behaviour of the fields and write

$$\begin{aligned}\frac{P_1^{ref}}{P_1^{dr}} &= \frac{A_1^{ref*}A_1^{ref}}{A_1^{dr*}A_1^{dr}}\\ &= \left(\frac{2\kappa_1^{in/out}-\kappa_1}{\kappa_1}\right)^2\\ &= \left(\frac{\kappa_1^{in/out}-\kappa_1^{loss}}{\kappa_1^{in/out}+\kappa_1^{loss}}\right)^2 .\end{aligned} \tag{7.1}$$

where we have assumed that the driving power, P_1^{dr} is equal to the amount of reflected power when the cavity is off resonance. This is a valid assumption for small intra-cavity decay rates and when the cavity is far from resonance. The P_1^{ref} term, refers to the amount of power that is reflected from the cavity when it is on resonance.

The result is an equation that resembles the form of the fringe visibility, Equation 3.8.1, which is very sensitive to the loss term, $\kappa_1^{in/out}$. Determining the loss from the reflected power is very sensitive because the drop on reflection is completely due to the intra-cavity loss. In the absence of any intra-cavity loss, the reflected field equals the input field and no dip in reflection is seen. The limitation to determining the intra-cavity loss from this method is how well one can know the reflectivity of the input/output coupler. However, as noted previously, this mirror typically has a moderately low reflectivity and thus the error introduced by being unable to account for scatter and absorption is minimal.

The final note on measuring the intra-cavity loss using the reflected dip in power on resonance is the effect that imperfect mode-matching has. Imperfect mode-matching into the OPO can result in a low estimate for the loss because of the fact that any mode-mismatched light will enter the detection photodiode and provide a DC offset. The situation is shown in Figure 7.8, where the reflected power from the input/output coupler of the ANU cavity was measured as the cavity length was scanned.

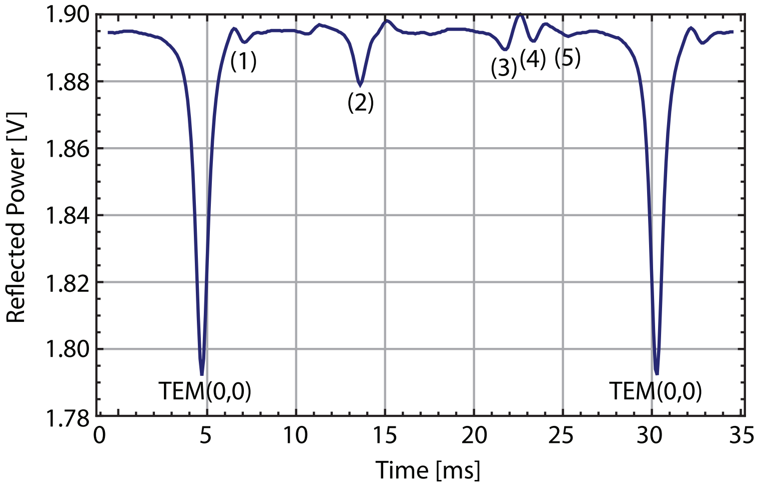

Figure 7.8: Reflected power from the OPO, in Volts, as the OPO length was scanned using a PZT. The higher order modes, modes (1)-(5), do not resonate when the cavity is locked to the TEM(0,0) mode.

We can quantify how well the light field is matched to the resonance of the cavity by defining the mode-matching value, MM, as

$$MM = \frac{MM_{(0,0)}}{MM_{(0,0)} + \sum MM_{(x,y)}}, \tag{7.2}$$

where $MM_{(0,0)}$ is the amount of light in the desired mode, in this case the (0,0) transverse electromagnetic mode, TEM$(0,0)$, and $\sum MM_{(x,y)}$ is the summation of the power in all the remaining modes. All values are measured in voltages and are relative to the maximum reflected value. For Figure 7.8 the mode matching is written as

$$\frac{TEM(0,0)}{TEM(0,0)+((1)+(2)+(3)+(4)+(5))}=0.784\pm0.003. \tag{7.3}$$

Let's assume that the cavity were off resonance, which is to say that we assume all modes $MM_{(x,y)}$ and $TEM(0,0)$ are off resonance. In this case, all of the light is reflected towards the detector. The power measured is therefore the total power of this field. When the cavity is on resonance, the reflected field consists of the reflected TEM(0,0) mode, *plus* the other modes that are not resonant at this particular cavity length. These other modes, in both cases, will result in a DC offset that needs to be subtracted. We can therefore rewrite Equation 7.1 for the case where the modematching is not perfect as

$$\frac{P_1^{ref}-\sum MM_{(x,y)}}{P_1^{dr}-\sum MM_{(x,y)}} \quad = \quad \frac{\left(\kappa_1^{in/out}-\kappa_1^{loss}\right)^2-\sum MM_{(x,y)}}{\left(\kappa_1^{in/out}+\kappa_1^{loss}\right)^2-\sum MM_{(x,y)}}. \tag{7.4}$$

This results in a loss value of 0.0026 ± 0.0001 per round-trip. Using this loss value and the coupling mirror transmission shown in Table 7.1, results in an escape efficiency of 0.985 ± 0.001.

For comparison, we can determine the estimated round-trip loss by multiplying all known loss sources from inside the cavity, the measured mirror transmission, and the expected AR coating and PPKTP absorption losses. The AR coatings on the non-linear crystal are specified at a transmission of 99.99% or higher, the PPKTP absorption was found by Wang [109] to be 0.02%/cm, and the two curved HR mirrors had a measured transmission of approximately 0.5%. The transmission of the coherent locking mirror was measured to be 0.9982 ± 0.0002. The resulting loss equivalent mirror power reflectivity is

$$\underbrace{0.9999*0.9999}_{2*ARCoatings}*\underbrace{0.9998}_{PPKTPAbsorption}*\underbrace{0.9995*0.9995}_{2*CurvedHR}*\underbrace{0.9985}_{Coh.Lock.HR}=0.9971\pm0.0005. \tag{7.5}$$

Equation 7.5 shows that the resulting loss equivalent mirror is 99.71 %. Using the values for the coupling mirror and cavity length from Table 7.1, this results in an escape efficiency of 0.983 ± 0.003. As discussed, this value is not as reliable as found by measuring the ratio of the reflected power on and off resonance but the two methods do agree.

7.2 The ANU experiment

The optical layout and electronic schematic for the ANU squeezer are shown in Figures 7.9 and 7.10 respectively. The majority of the main laser power (Innolight Mephisto) is directed towards the SHG (SHG lock), with the remaining light passing through the modecleaner cavity (MC lock) and providing the light for the LO field at the homodyne detector. A beamsplitter in the LO path taps off some light to be used as a seed for measuring visibility and parametric gain. The SHG passes through a Mach-Zender setup (MZ lock) in order to stabilise the pump power before entering the OPO. The Mach-Zender was only locked when squeezing measurements spanning over many hours were desired. The reflected pump field is detected at the OPO Ref 532 photo-detector and used to control the OPO cavity length via the Pound-Drever-Hall locking technique (OPO lock). The auxiliary laser, phase locked to and frequency shifted from the main laser by

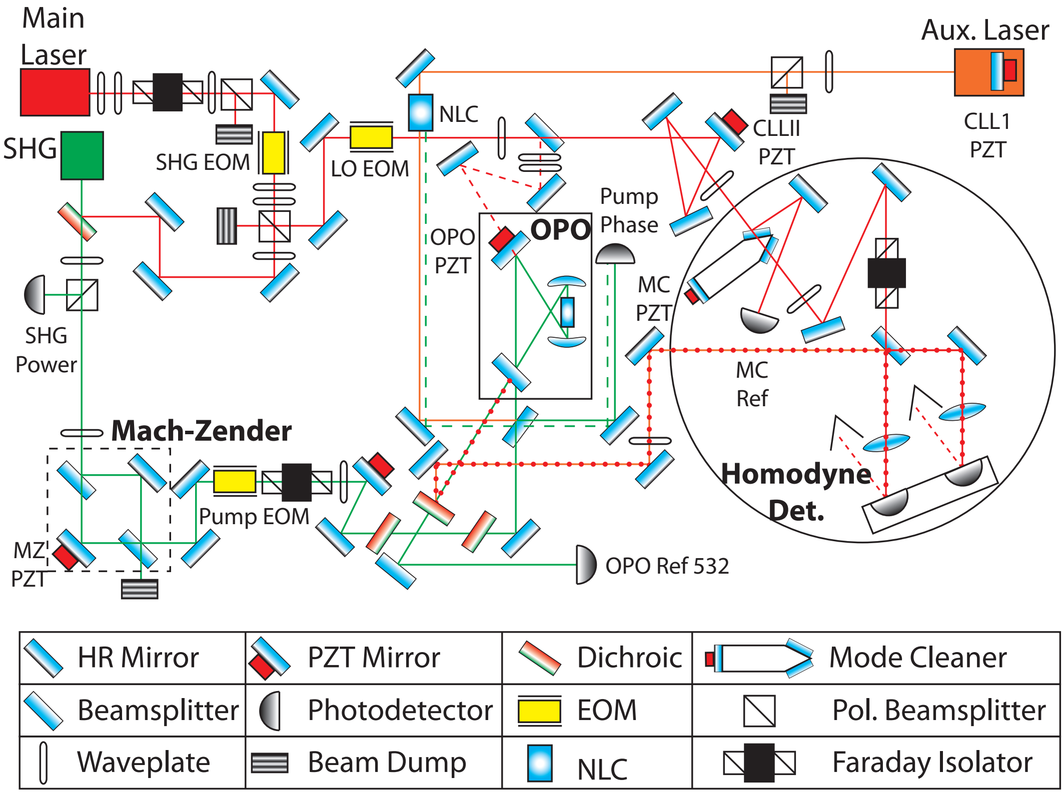

Figure 7.9: The layout of the ANU experiment. All of the optical elements apart from mode-matching lenses have been included. Red, green and orange fields are the fundamental, pump, and frequency offset auxiliary laser fields respectively. The dashed green beam is the auxiliary laser (Aux. Laser) second harmonic field, obtained after traversing a single pass through a non-linear crystal (NLC). The dotted red beam is the squeezed field. EOM is electro-optic modulator, dichroic indicates a dichroic mirror, and Pol. Beamsplitter represents a polarising beamsplitter.

29.8 MHz, makes a single pass through a PPKTP nonlinear crystal, generating a small amount of second harmonic. The second harmonic from the auxiliary laser beats, at 59.6 MHz, with some of the main laser second harmonic at the pump phase detector and is used to lock the phase of the pump field to the phase of the auxiliary laser (CLLI lock). The remaining power from the auxiliary laser enters the OPO, where it senses the nonlinear interaction and a second sideband field is generated, at -29.8 MHz. The beat between these two sidebands and the LO, at 29.8 MHz, is then used to derive an error signal to lock the phase of the LO to the phase of the auxiliary laser (CLLII lock).

The electronic loops for the ANU squeezer are shown in Figure 7.10. The second harmonic generation cavity length (SHG), Mach-Zender phase (MZ), optical parametric oscillator cavity length (OPO), the coherent locking loop phases (CLLI and CLLII), and the local oscillator mode cleaner cavity (MC) loops are all illustrated. The first half of the coherent locking loop, CLLI, locks the phase of the pump to the phase of the auxilliary laser, and the second half, CLLII, locks the phase of the local oscillator to the phase of the auxiliary laser. In the Mach-Zender loop, MZ, the SR560 preamplifier is set with a 6 dB per octave low pass filter at 3 Hz with a gain of 1. In the CLLII loop, the SR560 is set with a 6 dB per octave low pass filter at 100 Hz with a gain of 5. The servos, high voltage

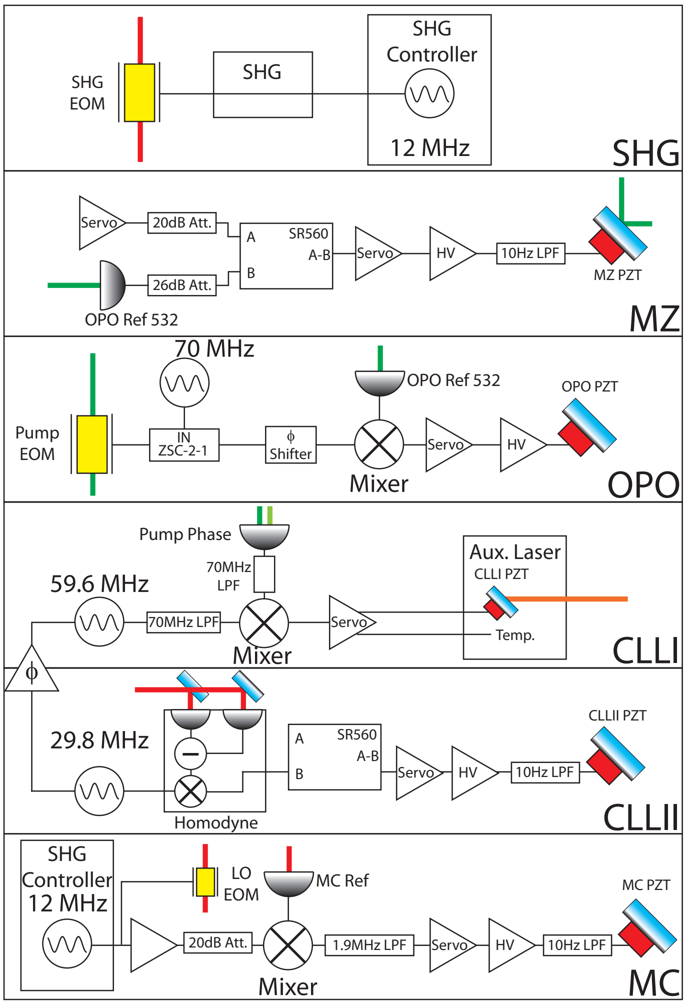

Figure 7.10: The electronics of the ANU experiment, showing the locking loops used. EOM - electro-optic modulator, HV - high voltage amplifier, SR560 - Stanford research systems preamplifier, LPF - low pass filter. Further explanation in text.

amplifiers (HV), and the phase shifter were all constructed in-house. The phase between the 29.8 MHz and 59.6 MHz frequency sources of the coherent locking loops are locked by a function within the frequency generators.

7.3 Squeezed State Control

It was shown by McKenzie *et al.* in 2004 that in order to produce squeezing in the audio detection band and below it was necessary to vacuum seed the OPO in order to remove various noise couplings [63]. This necessity is made apparent in Appendix 1, where the cavity equations of motion have been used to illustrate the relevant noise couplings. However, the presence of a bright seed allows for the use of standard modulation locking techniques in order to control the phase of the squeezing field [116]. Without a bright seed field centred about the squeezing, control of the squeezed state becomes a challenging task. In order to control the vacuum squeezing produced in the first audio-band squeezing measurements, McKenzie used a technique known as quantum noise locking [135]. This technique was shown to work and was capable of controlling vacuum squeezed states. However, it was found that, when locking a bright squeezed state, the performance of the lock was worse than a reference technique, that of standard dither locking. The stability of the lock was shown to be limited by both the amount of squeezing and the squeezing bandwidth [135]. Unfortunately, these two parameters are not easily improved, and the amount by which they can be improved is limited. It was concluded that quantum noise locking was a useful technique but that its performance was limited.

7.4 Coherent Control

In 2006 Vahlbruch *et al.* introduced a new method for locking a vacuum squeezed state. It was a coherent control technique and is now commonly simply called *coherent locking* [66]. This locking technique derives its error signals from a bright field that enters the squeezer, but is detuned from the resonant condition of the cavity, which is at half of the pump frequency. This field can then provide information about the non-linear process within the cavity, and hence the phase of the squeezed vacuum field, without seeding the squeezing. The scheme is illustrated in Figure 7.11.

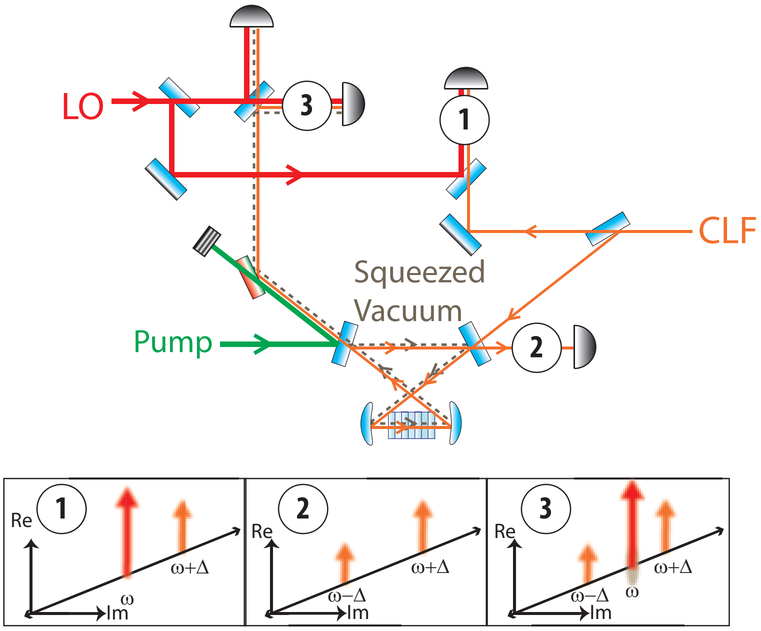

Figure 7.11: The coherent locking scheme. The fields important to the various locking loops are highlighted at locations 1,2,3. Full description of the fields and locking loops can be found in the text.

The final goal of the locking scheme is to lock the phase of the squeezing to the phase of the local oscillator. This occurs in many steps. At location 1 the auxiliary laser field, a single coherent sideband field (CSF), shifted from the fundamental frequency by an amount Δ, beats with a field from the main laser. This signal is used to offset phase lock the two lasers by the frequency Δ. This auxiliary laser is frequency offset so that the field can enter the OPO and undergo non-linear gain without seeding the process at the main laser frequency. Inside the OPO, the CSF experiences the non-linear interaction, resulting in a generated sideband field (GSF) (See § 7.4.1). The beat between the CSF and GSF fields, at a frequency of 2Δ, is detected at location 2 and is used to lock the phase of the pump to the phase of the auxiliary laser. It will be shown in § 7.4.1 that the phase of the GSF depends upon the phase of the pump field, providing the necessary phase information from the pump field for this loop. At location 3, the CSF, GSF and co-propagating squeezing have interfered with the LO at the homodyne detector beamsplitter. The beat at the frequency Δ betweeen the CSF, GSF and LO is used to lock the phase of the LO field to the auxiliary laser. The pump field which exits the OPO is transmitted through a dichroic mirror and dumped such that it does not reach the homodyne detector.

In summary, the coherent locking scheme has one loop to lock the phase of the auxiliary laser to the main laser. It then has a second loop to lock the phase of the pump field to the phase of the auxiliary laser and a final loop to lock the phase of the LO to the phase of the auxiliary laser. This chain of loops results in the phase of the LO being locked to the phase of the pump field. In Chapter 5 it was identified that the phase of the pump field defines the angle of the squeezing. Therefore, the phase of the LO is locked to the angle of the squeezing, as desired.

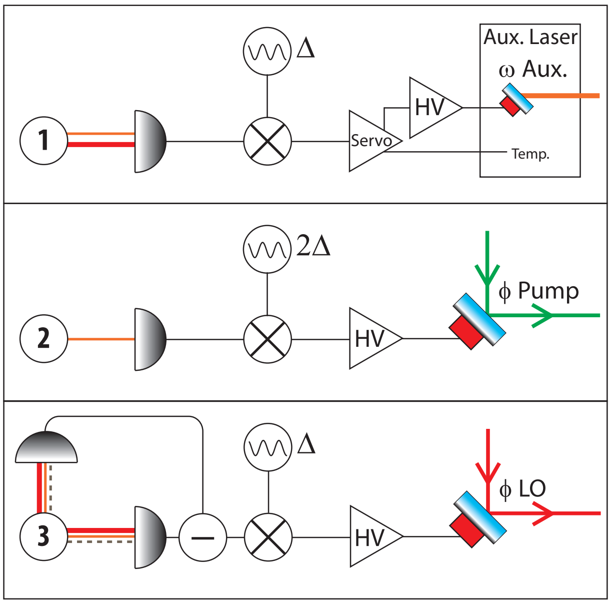

Figure 7.12: Simplified schematic of the locking loops that make up the coherent locking scheme. Fields 2 and 3 are the same as those illustrated in Figure 7.11. The two function generators at Δ and 2Δ are locked to one another to ensure phase stability between the two locking loops.

7.4.1 Coherent Control Model

We note that the coherent locking system is essentially a non-degenerate OPA, a system that we can model using the cavity equations of motion (Equations 5.32). We aim to model the classical behaviour of the CSF and GSF fields present in the coherent locking scheme. We begin by stating the classical equations of motion for the NDOPA and follow similar methods as undertaken by [136, 137, 138]

$$
\begin{aligned}
\dot{a}_1 &= i\Delta_1 a_1 - \kappa_1 a_1 + g a_3 a_2^\dagger + \sqrt{2\kappa_1^{in}} A_1^{dr} \\
\dot{a}_2 &= i\Delta_2 a_2 - \kappa_2 a_2 + g a_3 a_1^\dagger + \sqrt{2\kappa_2^{in}} A_2^{dr} \\
\dot{a}_3 &= i\Delta_3 a_3 - \kappa_3 a_3 - g a_1 a_2 + \sqrt{2\kappa_3^{in}} A_3^{dr}.
\end{aligned} \tag{7.6}
$$

In this case, terms with a subscript 1 represent the properties relating to the CSF, subscript 2 relates to the GSF field and subscript 3 is, as before, the pump field. The first simplification we will make is that the decay rates for the two locking fields, the CSF and the GSF, are equal. This is reasonable provided that the cavity is locked at the squeezing frequency (half of the pump field) because the two fields are symmetric about the fundamental frequency. We will also assume that the pump field is resonant. The detuning terms for the CSF and GSF fields *cannot* be set to zero as in the case of the OPA because these terms describe the detuning of the coherent locking field from half the pump frequency. The CSF field entering the cavity under standard operating conditions is incredibly small, so it is valid to assume that the pump field is not depleted. Finally, the GSF is not driven by an external field and hence we set $A_2^{dr} = 0$. Solving for the steady state of the system allows us to write

$$
\begin{aligned}
(\kappa_1 + i\Delta_1)\alpha_1 &= g\frac{\sqrt{2\kappa_3^{in}}\hat{A}_3^{dr}}{\kappa_3 + i\Delta_3}\alpha_2^* + \sqrt{2\kappa_1^{in}}\hat{A}_1^{dr} \\
(\kappa_2 + i\Delta_2)\alpha_2 &= g\frac{\sqrt{2\kappa_3^{in}}\hat{A}_3^{dr}}{\kappa_3 + i\Delta_3}\alpha_1^*.
\end{aligned} \tag{7.7}
$$

We wish to allow for any pump phase because this is important to the coherent locking scheme. To achieve this, Equations 7.7 are simultaneously solved for the intra-cavity field terms, α_1 and α_2, and their complex conjugates. This results in

$$
\begin{aligned}
\alpha_1 &= \frac{-\sqrt{2\kappa_1^{in}}A_1^{dr}\left(\kappa_2 + i\Delta_2\right)}{\frac{2\kappa_3^{in}g^2 A_3^{dr*}A_3^{dr}}{\kappa_3^2} - \left(\kappa_1 + i\Delta_1\right)\left(\kappa_2 + i\Delta_2\right)} \\
\alpha_2 &= \frac{-2g\sqrt{\kappa_1^{in}\kappa_3^{out}}A_1^{dr}A_3^{dr}\left(\kappa_2 + i\Delta_2\right)}{\kappa_3\left(\frac{2\kappa_3^{in}g^2 A_3^{dr*}A_3^{dr}}{\kappa_3^2} - \left(\kappa_1 + i\Delta_1\right)\left(\kappa_2 + i\Delta_2\right)\right)},
\end{aligned} \tag{7.8}
$$

where the relationship between the detuning of the CSF and GSF fields is such that $\Delta_1 = -\Delta_2$.

Using the input/output relations (Equation 5.9), we can determine the output fields and from this the power of the fields exiting the system (using Equation 5.5). Figure 7.11 shows the setup for the coherent locking field.

The chosen parameters match those for the ANU cavity, given in Table 7.1. It is important to note that for the coherent locking scheme, the input coupler is now the HR mirror that the CLF enters the cavity through, with $R = 0.9982$, and the output coupler is, as before, the mirror where the squeezing and the coherent locking field exit the cavity and travel towards the homodyne detector, with $R = 0.839$. The input coupler was chosen to have a reduced reflectivity, when compared to the other HR mirrors, in order to slightly increase the component of the GSF field at location 2. The reflectivity was chosen such that the additional intra-cavity loss, resulting in a lower escape efficiency, would be small compared to the total intra-cavity loss. The reflected and transmitted fields can thus be written

$$\begin{aligned}
A_1^{ref} &= \sqrt{2\kappa_1^{in}}\alpha_1 - A_1^{dr} & (7.9)\\
A_1^{trans} &= \sqrt{2\kappa_1^{out}}\alpha_1 & (7.10)\\
A_2^{ref} &= \sqrt{2\kappa_2^{in}}\alpha_1 & (7.11)\\
A_2^{trans} &= \sqrt{2\kappa_2^{out}}\alpha_1, & (7.12)
\end{aligned}$$

from which the powers of the fields can be determined using Equations 5.5. Under most circumstances, we can assume $\kappa_1^{in} = \kappa_2^{in}$ and $\kappa_1^{out} = \kappa_2^{out}$, by requiring that $\Delta_1 = -\Delta 2$.

We are now in a position where we can investigate the properties of the fields present in the coherent locking scheme. Figure 7.13 shows the power and phase properties of the transmitted and reflected CSF and GSF fields as a function of pump power and phase. The figure illustrates many important features of the coherent locking scheme. With no pump power, there is no generated sideband field. This is expected as there is no non-linear interaction to transfer photons to this field. As the pump power is increased, the non-linear gain of the system increases and photons are added to the CSF and GSF fields. The gain in the figure is limited because of the large detuning of the fields. It is necessary to ensure that the powers in the CSF and GSF do not become too large, otherwise noise on these fields will be detected by the homodyne detector, adversely affecting the squeezed state measurement.

As the phase of the pump field is varied, the phase of the CSF does not change but the phase of the GSF varies linearly for both the reflected and transmitted fields. This is a very important feature for the coherent locking scheme. The phase of the GSF is linearly related to the phase of the pump and this is what facilitates the locking of the phase of the auxiliary laser to the phase of the pump field.

The power seen in the reflected CSF and GSF fields highlights the limitation to this coherent locking scheme as it was constructed in this experiment. The reflected field consists of two components, the promptly reflected field and a component that escapes the cavity. The issue is that due to the fact that we are coupling in via an HR mirror, the promptly reflected component is much larger than the small amount that escapes the cavity. This is very clear in Figure 7.13, where the reflected CSF has a power of 99 μW and the reflected GSF has a power of 0.8 nW. The beat between these fields is small due to the very minor contribution from the GSF. The small amount of intra-cavity field leaking through this HR mirror results in a lock with a suboptimal signal to noise ratio and limited bandwidth.

It was experimentally seen that when the power of the auxiliary laser (or CSF field) was increased above hundreds of micro-Watts the squeezing degraded. The mechanism by which this happens is believed to be due to direct detection of the noise from the locking field on the very sensitive homodyne detector but is not fully understood. The effect this has, however, is to set a limit on the strength of the coherent locking field that can enter the cavity. In particular, this sets a limit on the amount of GSF field that exits the cavity, limiting the size of the beatnote used for the various locking loops.

One might ask whether the locking loop which locks the phase of the pump to the

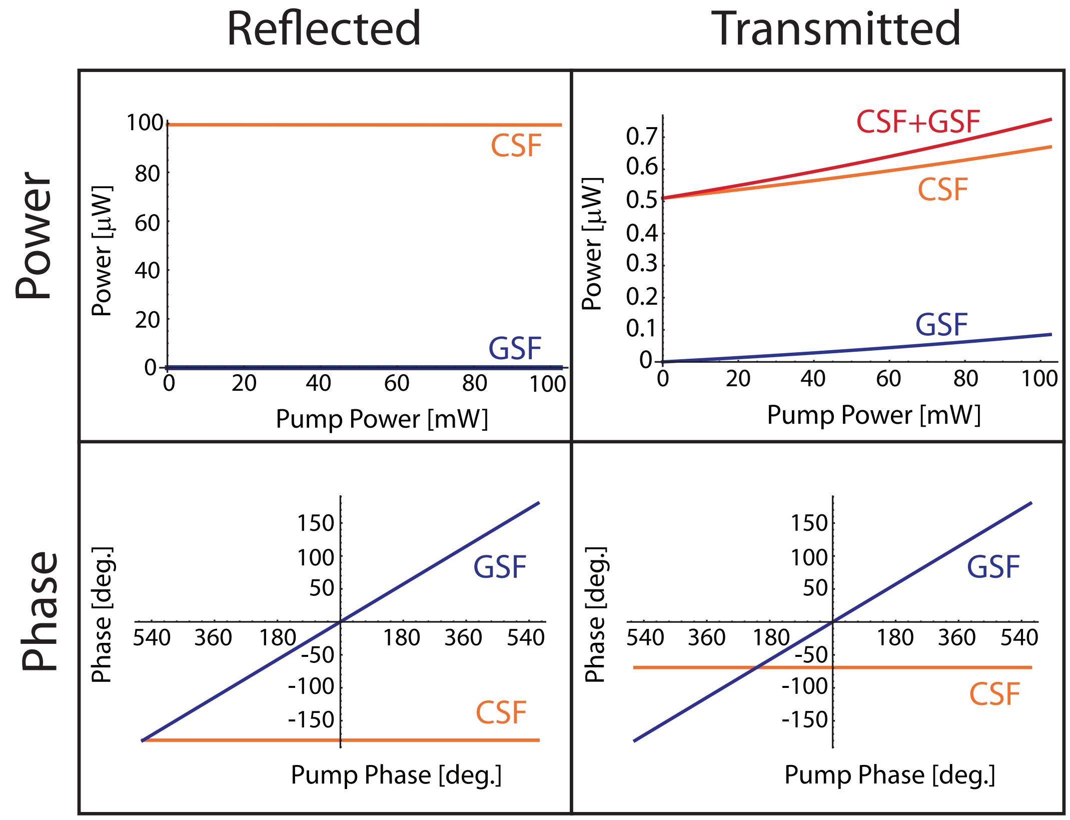

Figure 7.13: The powers of the transmitted and reflected CSF and GSF fields as the pump is increased up to OPO threshold and the phase of the CSF and GSF fields as the phase of the pump field is varied. The system is modelled on the ANU squeezer and as such all parameters are chosen to match those given in Table 7.1; cavity length $L = 0.273m$, non-linear interaction strength, $g = 1891$, reflectivity of the input/output coupler at the pump and fundamental wavelengths, $R_3^{in/out} = 0.722$ and $R_1^{in/out} = 0.839$, respectively, and intra-cavity loss at fundamental and pump, 0.26% and 4.6%, respectively. The coherent locking field power was set to 100 μW with a detuning of $\Delta_1 = 2\pi \times 29.8\,\mathrm{MHz}$. For the phase diagrams, a pump power of 90 mW is assumed.

phase of the auxiliary laser, location 2 in Figure 7.11, could instead be derived from the field that exits the front coupler, where transmission is orders of magnitude larger than those for the HR mirrors. However, this field also carries the squeezed light and as such detection of this field before the homodyne detector cannot be made without degrading the squeezing. It might then be possible to derive the error signal for this lock at the homodyne detector. The homodyne detector is already used to lock the LO phase to the coherent locking fields but it could also be used to lock the CSF to the pump phase provided that the extra path length from the squeezer to the homodyne detector were stable. This should theoretically produce a much stronger lock because of the increased field strength exiting through the front coupler. The issue that arises, however, is that the homodyne detector must now detect in the gravitational-wave audio-band, at Δ_1 and at $2\Delta_1$. This is technically challenging to do without affecting the performance of the detection circuit in measuring the squeezed state and of the locks themselves. In particular, second harmonics of the lock at Δ_1 may affect the stability of the second lock at $2\Delta_1$.

The coherent locking scheme was the original scheme used to control the angle of the squeezing in the ANU squeezer. With this scheme, the unity gain frequency of the loop that locked the phase of the auxiliary laser to the pump phase was approximately 20 Hz and the bandwidth of the loop that locked the LO phase to the CLF was 40 kHz. The very poor bandwidth of the fist loop was the limiting factor in our control scheme and so it was desirable to determine if a new method could be devised in order to improve the stability of our squeezed state control.

7.4.2 Modified Coherent Locking

The concept of the modified coherent locking scheme was that instead of locking the phase of the CLF to the pump phase by sensing the non-linear interaction, the phase between these two fields could be locked by first up-converting some small portion of the auxiliary laser field and then beating the pump field with this second harmonic CSF field. This would also lock the phase of the auxiliary laser to the phase of the main laser in the same locking loop, removing one of the locking loops from the original coherent locking scheme.

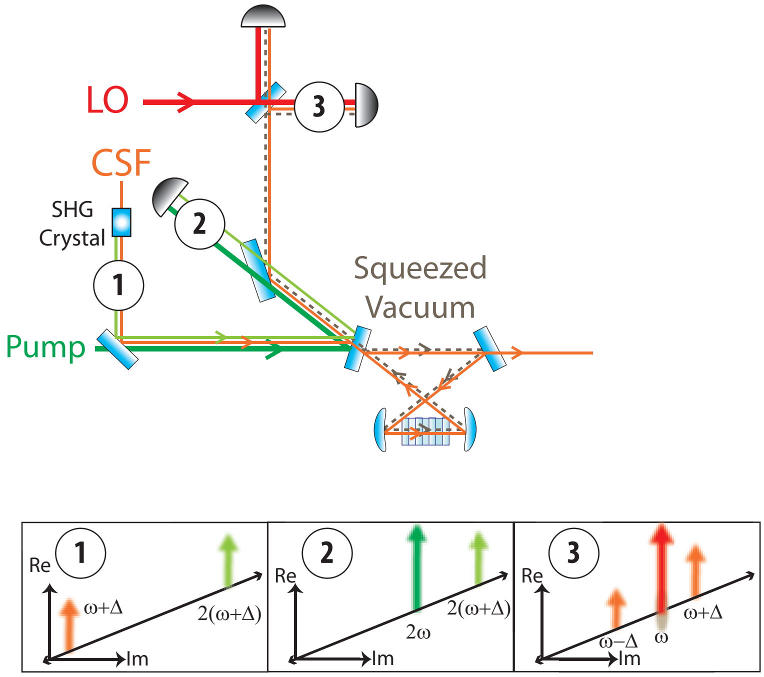

Figure 7.14: The modified coherent locking scheme. The important fields are highlighted at locations 1,2,3. A full description of the fields and locking loops can be found in the text.

The experimental setup for the modified coherent locking scheme is shown in Figure 7.14. At location 1 the coherent sideband field (CSF), shifted from the fundamental frequency by an amount Δ, and its second harmonic are present. The second harmonic is generated using a single-pass non-linear medium. At location 2 the green light reflected from the OPO and transmitted through a dichroic beamsplitter is detected. The beat, at a frequency of 2Δ, between the up-converted CSF and the pump field is used to offset phase lock the frequency of the auxiliary laser to the main laser using a standard offset phase lock [139]. At location 3 the fields are unchanged from the original coherent locking scheme, the CSF, GSF, squeezing and LO fields are all present at this location.

By moving to this modified coherent locking scheme, the first locking loop can now be optimised by varying parameters that do not affect the squeezing. In particular, the power in the frequency doubled CLF field can be tailored for the locking loop. The already strong second half of the lock, the loop that locks the phase of the LO to the phase of the auxiliary laser, remains unchanged. The electronic loop of the modified coherent lock, which locks the phase of the auxiliary laser to the phase of the pump, is shown in Figure 7.15.

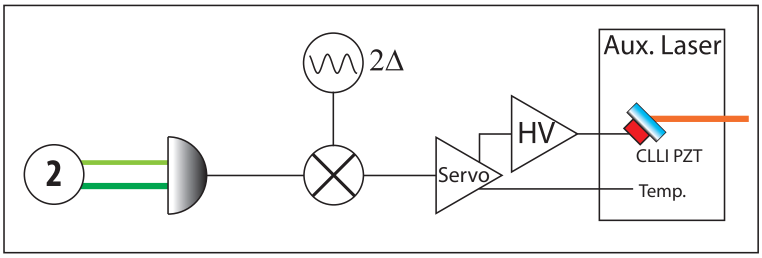

Figure 7.15: The modified coherent locking electronics scheme. The beat between the pump and up-converted auxiliary laser fields is used to derive an error signal. This error signal locks the phase of the the auxiliary laser field to the phase of the pump field. Note that this loop also locks the frequency of the auxiliary laser to the frequency of the main laser, with an offset of Δ.

With this modified coherent locking scheme, the bandwidth of the loop locking the auxiliary laser phase to the pump phase was 2.5 kHz. The larger bandwidth results in better suppression of the phase fluctuations on the squeezed field, reducing phase jitter. This lock is more flexible due to two reasons; the amount of frequency doubled CSF can be varied and; the fundamental CSF field power is only used for the stronger lock at the homodyne detector, allowing for reduction of the the power in the CSF is so desired. The CSF power used in the experiment for this locking loop was not changed from the original coherent locking scheme, retaining its bandwidth of 40 kHz.

Both of these coherent locking schemes share an inherent weakness. This is that the coherent locking schemes do not strictly force the lock to the angle of squeezing. It merely ensures that the phase of the local oscillator in the homodyne detection scheme is locked to the phase of the pump. In both the original and modified coherent locking schemes, if the temperature of the non-linear medium changes in a way that cannot be compensated for, as is the case with localised thermal heating due to drifts in pump power, then the cavity is no longer perfectly resonant for both the pump and squeezed fields. This condition results in a shift between the angle of the squeezed light and the local oscillator. Nonetheless, even with this limitation, stability has been shown over many hours after recognising local heating due to pump field fluctuations were a major source of noise, first identified and overcome through stabilisation of the pump field power by Khalaidovski [140]. Stable squeezing, controlled using the coherent locking scheme,in this paper was shown to have a duty cycle of 99 % over 20 hours.

Chapter 8

Detection of Squeezed States

This chapter introduces the challenge of the detection of the states described thus far. The first measurements of squeezing in the audio-frequency band were limited by excess noise at low frequencies [63]. A "roll-up" in the frequency spectrum was seen towards lower frequencies. This noise was evident on both the shot noise and squeezing measurements [63, 66]. This led to the interesting situation where it could not be determined whether the squeezing itself was degrading at low frequencies, or whether it was simply a limitation of the measurement device. It was later shown that it was indeed possible to measure white shot noise at frequencies down to below one hertz [141]. Beam jitter, electronics, local oscillator noise coupling [64], non-stationary events in the balanced homodyne detector output [65], and parasitic interference [141, 142] have all been shown to contribute to the excess noise at low frequencies. In this chapter we present our findings on low-frequency noise sources and the steps by which the various sources were identified and mitigated. This chapter is based largely on the work presented in a paper recently written on this topic [87].

8.1 Balanced Homodyne Detection Noise Couplings

We investigate the noise coupling by modelling the photocurrents in the balanced homodyne detector in the same way as introduced in § 3.8. The model is set up as shown in Figure 8.1. A bright local oscillator, $\hat{A} = \alpha + \delta\hat{a}$, and the weak signal beam, $\hat{B} = \delta\hat{b}$, of interest interfere on a beamsplitter of power splitting ratio, η_{bs}, that is close to, but not precisely, 50 %. We assume that the signal field has no coherent amplitude, and is thus a vacuum or squeezed vacuum state. The two photo-detectors have differing quantum efficiencies, $\eta_1(x, y)$ and $\eta_2(x, y)$, that vary in the transverse plane. A loss term, η_l, is added to one arm of the balanced homodyne detector to simulate loss from sources such as dust (location 2). We define the δ_V terms as the vacuum fluctuation contributions entering due to the the losses from the various loss sources, the inefficient photodiodes, δV_1 and δV_2, and the loss introduced in one of the balanced homodyne detector arms, δV_0.

The fields incident on the two photo-detectors, $F_{1,2}$, are written

$$\hat{F}_1 = \sqrt{\eta_1}\left(\sqrt{1-\eta_l}\left(\sqrt{\eta_{\mathrm{bs}}}\hat{A} + \sqrt{1-\eta_{\mathrm{bs}}}\hat{B}\right) + \sqrt{\eta_l}\delta\hat{V}_0\right) + \sqrt{1-\eta_1}\delta\hat{V}_1, \quad (8.1)$$

$$\hat{F}_2 = \sqrt{\eta_2}\left(\sqrt{\eta_{\mathrm{bs}}}\hat{B} - \sqrt{1-\eta_{\mathrm{bs}}}\hat{A}\right) + \sqrt{1-\eta_2}\delta\hat{V}_2, \quad (8.2)$$

where the explicit spatial dependence of the photodiode efficiencies have been removed for succinctness. The ideal photocurrent produced by photodiode 1 is then proportional to $\hat{F}_1^\dagger\hat{F}_1$ and similarly for the photocurrent in photodiode 2. The two photocurrents can

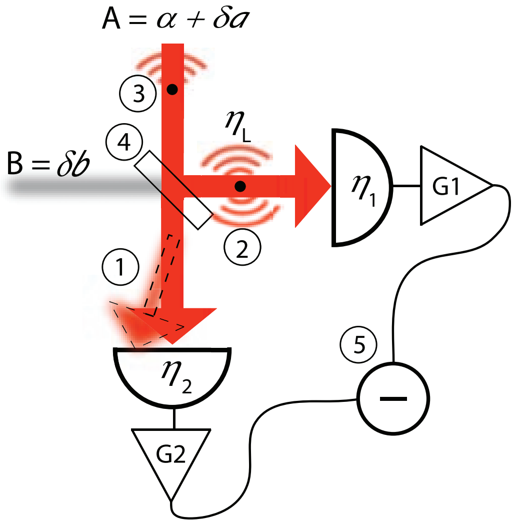

Figure 8.1: Conceptual view of the major issues arising in low-frequency measurements with a balanced homodyne detector setup; 1 - beam pointing, 2 - scatter resulting in loss and/or mode shape disortion, 3 - scatter leading to parasitic interference, 4 - the splitting ratio of the beamsplitter, 5 - the subtraction of the photocurrents. All other terms are described in the text.

thus be written

$$\begin{aligned}
\mathrm{i}_{\mathrm{HD1}} &= \eta_1\eta_{\mathrm{bs}}(1-\eta_l)\alpha^2 + \eta_1\eta_{\mathrm{bs}}(1-\eta_l)\alpha\delta\hat{X}_a^+ + \\
&\quad \eta_1\sqrt{\eta_{\mathrm{bs}}}\sqrt{1-\eta_{\mathrm{bs}}}\sqrt{1-\eta_l}\alpha\delta\hat{X}_b^+ + \sqrt{\eta_1}\sqrt{\eta_{\mathrm{bs}}}\sqrt{1-\eta_1}\sqrt{1-\eta_l}\alpha\delta\hat{X}_{V1}^+ + \\
&\quad \eta_1\sqrt{\eta_{\mathrm{bs}}}\sqrt{1-\eta_l}\sqrt{\eta_l}\alpha\delta X_{V0}^+ \qquad (8.3)\\
\mathrm{i}_{\mathrm{HD2}} &= \eta_2\sqrt{1-\eta_{\mathrm{bs}}}\alpha^2 + \eta_2(1-\eta_{\mathrm{bs}})\alpha\delta\hat{X}_a^+ - \eta_2\sqrt{\eta_{\mathrm{bs}}}\sqrt{1-\eta_{\mathrm{bs}}}\alpha\delta\hat{X}_b^+ - \\
&\quad \sqrt{\eta_2}\sqrt{1-\eta_{\mathrm{bs}}}\sqrt{1-\eta_2}\alpha\delta\hat{X}_{V2}^+, \qquad (8.4)
\end{aligned}$$

where the $\delta\hat{X}_a^+ = \delta\hat{a}^\dagger + \delta\hat{a}$ terms are the amplitude quadrature fluctuation operators for the field fluctuation term $\delta\hat{a}$ and similarly for $\delta\hat{X}_b^+$. It is the subtraction of these two photocurrents, limited by experimental imperfections, that gives the output of the balanced homodyne detector. Many of the coupling mechanisms for the various noise sources can be seen in these equations and will be discussed in the following sections.

8.2 Electronic Issues

In an attempt to organise the various noise sources, the issues have been divided into those of an electronic nature, and those of an optical nature. However, the distinction is not always clear because many of these issues have a source in one of these origins but couple in via some mechanism in the other. We begin by discussing the issues of an electronic nature that limit the low-frequency measurement of squeezed states.

8.2.1 Balanced Homodyne Photo-Detector Electronics Designs

Two differing electronic designs for balanced homodyne photo-detectors were investigated. Their simplified schematics are shown in Figure 8.2. The first is a twin photo-detector, variable gain design. In this design, the measured photocurrents are immediately amplified through a trans-impedance stage on separate electronic boards and an electronic subtractor then takes the difference between these two signals [63]. The gain between the two detectors can be varied to allow the subtraction of the photocurrents to be optimised electronically, allowing for the compensation of uneven optical powers and differences in the photodiode responses. This allows for the compensation of unequal $\eta_1(x, y)$ and $\eta_2(x, y)$ terms as well as an imperfect $\eta_{\rm bs}$ term from § 8.1. This design, henceforth known as the *variable gain* design, is given in detail in [108], and the first measurements of audio-band squeezing were made using this balanced homodyne detector design.

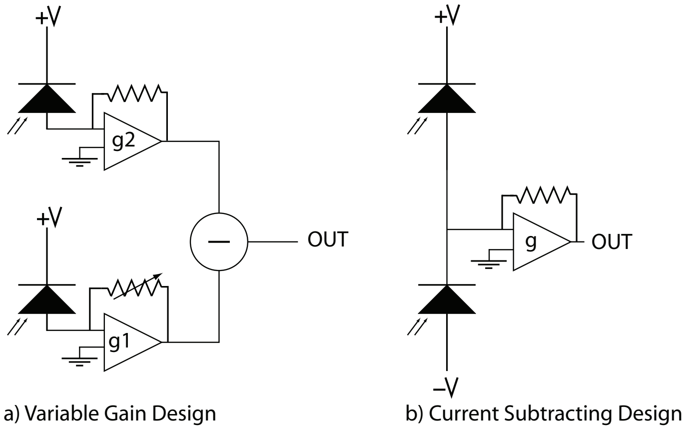

Figure 8.2: The two balanced homodyne detector schemes: a) The variable gain design. The photocurrents from the two photodiodes undergo separate transimpedance gain stage, g1 and g2, and the two output signals are then subtracted. b) The current subtracting design. The two photocurrents are subtracted before undergoing any electronic gain, g.

The second design is a single electronic board design, also shown in Figure 8.2. In this design the photocurrents of both photodiodes are immediately subtracted from each other before undergoing any amplification. There is no longer a variable electronic gain and thus, balancing of the subtraction must be done optically, through manipulation of the $\eta_{\rm bs}$ term. This is typically achieved by rotating the polarisation of the local oscillator and/or signal field. A homodyne detector utilising this design, henceforth known as the *current subtracting* design, is given in detail in [143]. A detector utilising this design was constructed at the Max Planck Institute for Gravitational Physics in Hannover, Germany and was provided to the ANU for use in the ANU squeezing experiment, to be later used in the LIGO squeezed light injection. This detector had already been shown to measure squeezing down to below 10 Hz [141] and was used in most of the homodyne detector measurements presented in this thesis. The current subtracting design has reduced classical noise due to the fact that all of the electronic components after the photodiodes are common.

The current subtracting design also eliminates a second noise source, flicker noise. This is not the case, however, for the variable gain design and as such it is necessary to address the issue. Flicker noise is a noise source found in resistors that is proportional to the amount of current passing through the resistor [144]. Flicker noise results in a pink noise spectrum, or a 1/f roll-up towards low frequencies. The source of flicker noise is not well known, but it can be mitigated using wire wound or metal film type resistors [145]. Figure

8.3 shows shot noise measurements for the variable gain design constructed with standard carbon film and with low flicker noise metal electrode leadless face (MELF) type resistors. An experiment was devised where shot noise was measured in three separate cases. The first two cases involved two identical homodyne photodetectors, the same as that presented in [108], set up to work as a variable gain homodyne detector. One measurement was taken with carbon film resistors and the other with MELF resistors. In the third case, one of these photodetectors was modified by adding a second photodiode and having current subtraction between these two photodiodes occur before the first gain stage, as shown in Figure 8.2. This was done on a board using standard carbon film resistors to show that the current subtracting design mitigates flicker noise. The results of these tests are shown in Figure 8.3.

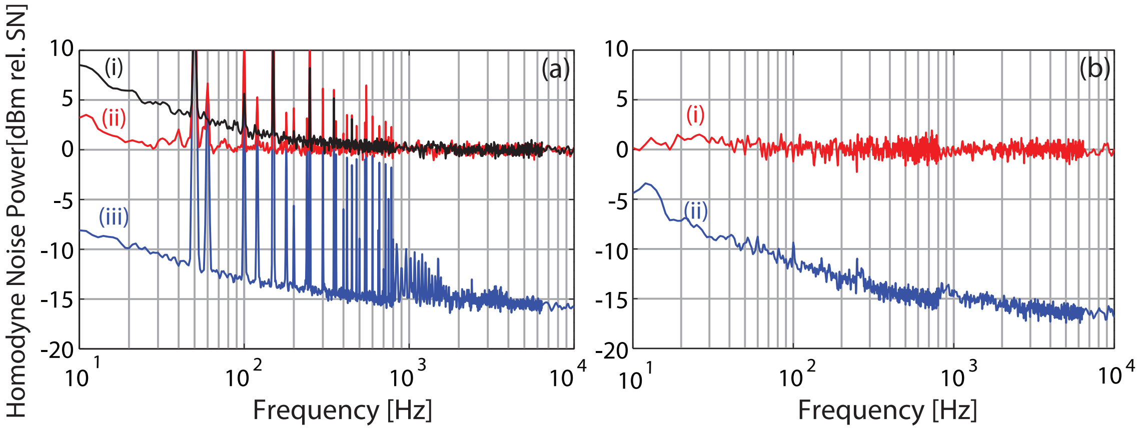

Figure 8.3: Figure (a) shows the dark noise, (iii), and two shot noise traces, (i) and (ii), for the variable gain balanced homodyne detector design with a local oscillator power of approximately 1.9 mW. In trace (i), standard carbon film resistors are used and the shot noise is seen to deviate strongly at lower frequencies. Replacing these resistors with low flicker noise resistors results in the near flat shot noise measurement seen in trace (ii). The deviation seen near 10 Hz is believed to be caused by parasitic interference, as it was seen to have a time dependence (See § 8.3.4). Figure 3(b) shows the normalised dark noise (ii) and shot noise (i) for the current subtracting design, constructed by adding a photodiode to one of the photodetectors used in the variable gain homodyne detector. As expected, even with standard carbon film resistors, flat shot noise was measured to 10 Hz. All traces are pieced together from 3 FFT windows: 0-800 Hz, 0-6.4 kHz, 0-102.4 kHz with 800 FFT lines, resulting in resolution bandwidths of 1 Hz, 8 Hz, and 128 Hz respectively. 200 RMS averages were taken for all traces. The noise spikes seen in (a) are due to mains harmonics that could not be removed.

The homodyne detector board design used to produce the traces in Figure 8.3 was the same as that used in the first measurement of squeezing in the audio-band [63]. Flicker noise had not yet been identified as a limiting noise source and as such, the measurements, taken with a variable gain board, had a very similar roll-up to that illustrated in Figure 8.3 (a) trace (i). Flicker noise was almost certainly the major noise contributor in this early experiment. As shown in Figure 8.3, the use of low flicker noise components is enough to reduce the flicker noise to a level that no longer affects the measurements at the frequencies we are interested in.

8.2.2 Dark Noise

Dark noise, the electronic noise of the detection system when no light is incident on the photodiodes, can also limit the measurement of shot noise and even more so squeezing. This is typically worse at lower frequencies where electronics tend to have increased noise. The problem is a technical one but it is worth briefly mentioning. Depending upon the operating conditions, the current and voltage noise in the op-amps, and less so the the dark current of the photodiode, are the sources of dark noise. Correct selection of readily available components ensures that the dark noise does not limit the measurement. The dark noise is typically measured relative to the shot noise level. The required clearance between the two is dependent upon the amount of squeezing one wishes to measure. Typical detectors can be made and bought with the shot noise approximately 10 dB above the dark noise for normal operating conditions, but more advanced designs have the shot noise around 20 dB or greater above the dark noise [143]. The clearance between shot noise and dark noise can be increased in the balanced homodyne detector by increasing the power of the LO field, thereby increasing the amount of measured shot noise. The limitations to this however, are the amount of power that the photodiode can receive before damage occurs and the fact that a greater LO field strength leads to a larger amount of classical noise. This increases the amount of subtraction the balanced homodyne detector needs to achieve in order to operate in the quantum noise limited regime.

Dark noise degrades shot noise and squeezing measurements because the noise of the electronics adds to the measured shot noise or squeezing and makes them appear noisier than they actually are. For the purpose of estimating the amount of squeezing incident on the detector, one can correct for dark noise by simply subtracting it from all other traces. For some signal, S, we can write its dark noise corrected value, S_{DNcor}, in dBm as

$$S_{\mathrm{DNCor}}[\mathrm{dBm}] = 10\log_{10}(10^{S/10} - 10^{\mathrm{DN}/10}), \tag{8.5}$$

where S[dBm] is the measured signal strength in dBm, and DN is the measured dark noise, in dBm.

8.3 Optical Issues

Many optical issues also need to be addressed in order to achieve flat shot noise across the audio-frequency spectrum. These optical issues and their solutions were investigated on a simple tabletop experiment, shown in Figure 8.4. The output of an ND:YAG 1064nm laser, after passing through a Faraday isolator, was directed into a steel chamber through an anti-reflection (AR) coated window. Within the chamber, the light underwent spatial filtering with a triangular ring mode-cleaner cavity or modecleaner with a linewidth of approximately 4.7 MHz. The modecleaner was locked using the Pound-Drever-Hall technique [146]. The light travels through a half-wave plate and is then incident on the beamsplitter which directs the light towards a current subtracting balanced homodyne detector [143]. The half-wave plate is used to tune the beamsplitter power splitting ratio, η_{bs}.

8.3.1 Optical Balancing

Balancing the optical splitting ratio of the beamsplitter is crucial to the performance of the balanced homodyne detector. A high common mode rejection ratio (CMRR), the

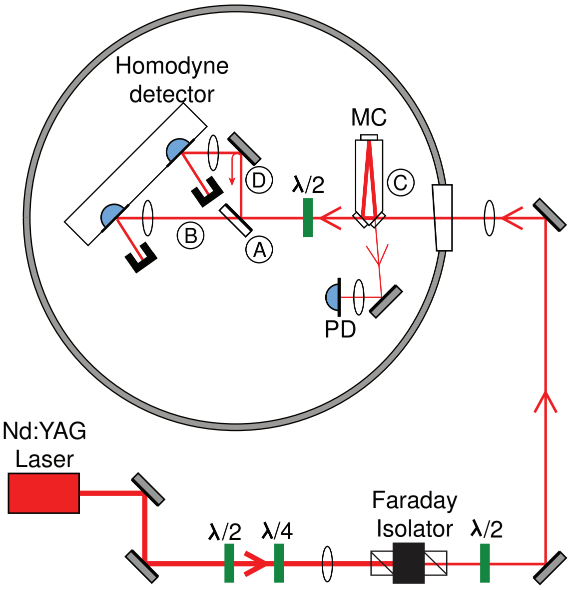

Figure 8.4: The optical layout of the experiment designed to detect low-frequency noise sources in the balanced homodyne detector setup. A high-speed photo-detector (PD) was used to lock the modecleaner cavity (MC). The core components are enclosed in a steel chamber with an AR coated window. The circled labels refer to the locations of issues discussed in following sections; (A) 8.3.1 - Optical Balancing; (B) 8.3.2 - Scattering Loss (C); 8.3.3 - Beam Pointing (D); 8.3.4 - Parasitic Interference.

measure of the ability of the balanced homodyne detector to reject signals common to both photodiodes, is necessary such that classical noise present on *both* fields entering the beamsplitter, the local oscillator and the signal field, is subtracted to a level well below the shot noise level by the balanced homodyne detector. This issue is highlighted in Equation 8.3. It is seen that with optimisation of the $\eta_{1,2}(x,y)$ and $\eta_{\rm bs}$ terms, the subtraction of these two photocurrents can completely remove all terms proportional to δX_a^+, which is the noise on the local oscillator field. This is a necessary condition for the balanced homodyne detector setup to ensure that one is accurately measuring the signal field, absent unwanted classical noise sources.

The importance of balancing the beam splitting ratio becomes even more critical when the signal field itself carries noise which needs to be subtracted, such as in the coherent locking scheme [66]. The optical balancing is firstly tuned with the splitting ratio of the beamsplitter, primarily through tuning of the angle. The coatings on the beamsplitters typically do not allow for a perfect splitting ratio, and as such, the final balancing is done through adjustment of the polarisation of the input fields using a half-wave plate. Alternatively, if a variable gain design were used, then this adjustment could be made through varying the gain. Optimising for the local oscillator arm, a stable CMRR of up to 80 dB was consistently achieved. Figure 8.5 shows that this level of subtraction should be enough to adequately to suppress the classical laser noise from the local oscillator across the entire spectrum. With this setup, a CMRR of 50 dB was obtained for the signal field. This is sufficient because the power in the signal field is many orders of magnitude less than the local oscillator.

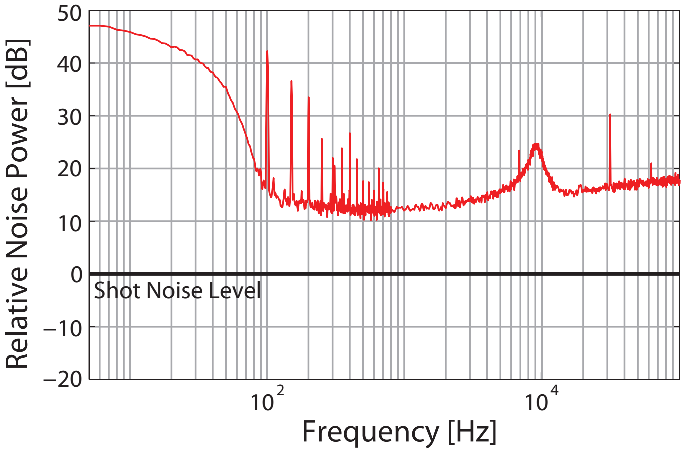

Figure 8.5: Relative intensity noise of the local oscillator field incident on the balanced homodyne detector. At low frequencies, local oscillator intensity noise is more than 40dB greater than shot noise. The trace is pieced together from 3 FFT frequency ranges: 0-800 Hz with 50 root mean square averages, 0-6.4 kHz and 0-102.4 kHz both with 100 averages. All traces taken with 800 FFT lines, resulting in resolution bandwidths of 1 Hz, 8 Hz and 128 Hz respectively.

8.3.2 Scattering Loss

We define scattering loss as an event occurring in the beam path which causes the scattered light to exit the beam path and be lost to the system. Scattering events before the beamsplitter will not affect the splitting ratio, but can couple noise in through changes in mode shape (this is further discussed in § 8.3.3). However, problems can arise if the loss originates in one of the balanced homodyne detector arms after the beamsplitter. This loss, η_l, is illustrated in Figure 8.1 and in Equations 8.3. Dust particles, originating from many sources such as clothing and skin, passing through the beam due to air currents or gravity, will result in a non-zero loss term and momentarily reduce the magnitude of the photocurrent, i_{HD1}. This momentary change in the photocurrent occurs at frequencies characteristic of the speed of the particle and will unbalance the homodyne detector setup. This will result in a reduction of the CMRR, the transient value of which may not be adequate to cancel the classical intensity noise of the laser.

If the dust particle in the beam path reduces the power in one of the beams by one percent, the subtraction is reduced from 80 dB to 40 dB. Figure 8.5 shows that this reduction in CMRR is enough to couple classical intensity noise into the output of the balanced homodyne detector. In addition, intensity noise at frequencies characteristic of the time taken for the dust particle to traverse the beam, will couple directly to the output. Prior work has shown that settling of dust does in fact improve the noise statistics of shot noise measured using a balanced homodyne detector [65].

The effect of loss due to scattering in the homodyne detector arm was investigated by first setting the optical power on each photodiode to 7V. With light on both photodiodes, the DC voltage was subtracted to less than 1 mV. An air puffer was then used to disturb the dust that had settled on various optics mounts. During this process, the subtracted output of the detector was monitored on an oscilloscope. With this configuration, substantial spikes in the subtracted output were observed for a few seconds after dust was excited with the puffer at a location after the beamsplitter.

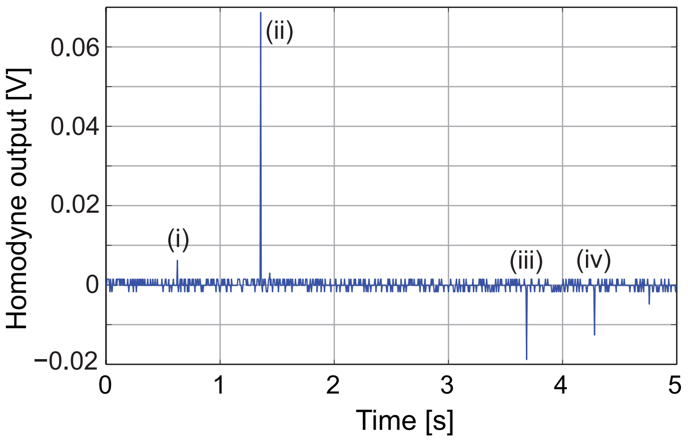

Figure 8.6: The DC output of the balanced homodyne detector as a function of time. At time t=0 a puffer was used to excite dust on a lens mount in the beam path. The spikes in the output, (i)-(iv), are individual dust events affecting the balancing of the homodyne detector.

Figure 8.6 shows the voltage measured on the balanced homodyne detector over time after one such excitation. Four spikes were observed, the largest causing a 0.07 V, or 1 %, change in the voltages between the two photodiodes. The typical voltage seen from these disturbances was approximately 0.01 V. These spikes would occur over a few seconds following the excitation.

We also excited dust activity before the beamsplitter to see what effect this has on the balanced homodyne detector. As expected, no spikes in the subtracted signal were observed because the dust-induced loss is now common to both arms. Isolation against scattering loss post homodyne detector beamsplitter is therefore crucial. The best way to stop dust is to ensure the cleanliness of the environment. Clean rooms, suitable clothing and enclosures all aid in reducing the amount of dust present in an experiment. However, there always will be some dust present in air, therefore eliminating the air currents that carry the dust through the beam paths, such as with an enclosure, is the next step. The steel tank placed around the detection optics in our experiment both reduced the dust present and the air currents. Once the tank was in place and sealed, the spikes in the DC output of the balanced homodyne detector were no longer seen.

8.3.3 Beam Pointing and Mode Shape

A fundamental limitation to the photocurrent subtraction of the balanced homodyne detector is provided by the spatially non-uniform response of the two photodiodes in the detection scheme. This is represented by photodiode quantum efficiencies that are a function of position, $\eta_{1,2}(x, y)$. An investigation into the response of typical photodiodes has shown that there are differences in the quantum efficiency across the photodiode surface and also indicated that small “dead regions” are common [147, 148]. This inhomogeneity allows for beam pointing and mode shape changes to couple into the measurement as a noise source.

Beam pointing, also known as beam jitter, is a change in the trajectory of the beam, which results in a translation of the intensity profile on the photodiode surface. Beam pointing originates from forces acting on optical components, such as acoustic vibrations

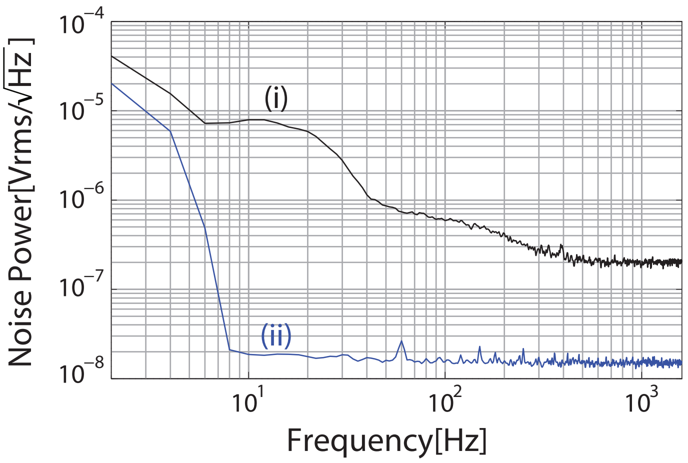

Figure 8.7: Balanced homodyne detector output traces illustrating a beam pointing event. Trace (ii) is the regular shot noise level and trace (i) is the output of the balanced homodyne detector during a typical blow-out event. The experimental setup is that shown in Figure 8.4, with the lid of the steel tank removed. Blow-outs such as that seen in trace (i) occurred every few seconds, with flat traces seen for most of the remaining time. All traces are measured with a span of 0-1.6 kHz with 800 FFT lines, resulting in a resolution bandwidth of 2 Hz. 100 root mean square averages were taken for both traces.

and air currents, or from changes in air density in the beam path resulting in varying refractive indices - the Schlieren effect [75]. If the transverse profile or positioning of the beam changes (see § 8.3.3), then the photocurrent from the photodiode will vary due to the spatial dependence of the diode efficiencies. Writing the spatial dependency on the quantum efficiency in radial coordinates, $\eta(r,\theta)$, the intensity measured by the photodiode is the integral over the entire diode surface, assumed to be circular, of the quantum efficiency multiplied by the intensity profile, and can be written

$$\int_0^{d/2}\int_0^{2\pi} I(r,\theta)\eta(r,\theta)\,d\theta\,dr, \tag{8.6}$$

where d is the diameter of the photodiode surface and $I(r,\theta)$ is the intensity profile of the incident field in radial coordinates.

This will directly modulate the photocurrent of the detectors and will be uncommon to both signals due to the differing responses of the photodiodes, hence it cannot be subtracted. The frequency dependence of this noise will be determined by the specifics of the photodiode inhomogeneities and the speed of the beam translation. The frequency characteristics are illustrated in [64] and show that the noise becomes larger at lower frequencies. The effect of beam pointing can be seen by disturbing the air near to the beam path, anywhere on the table. Many large blow-outs in the spectrum at frequencies up to about 1 kHz can be seen in the output spectrum when this disturbance is introduced. One of these events is shown in Figure 8.7.

These effects can be reduced by designing the experiment to be robust to pointing fluctuations by using short, shielded beam paths, and mechanically stable optics mounts. This effect can also be reduced by enlarging the spot size on the photodiode surface in order to better average these inhomogeneities, whilst ensuring that all of the light is still detected. To completely solve the issue, a mode-cleaning optical cavity was placed in the balanced homodyne detector setup [141]. Beam pointing can be thought of as the coupling of some fraction of the original beam power into different spatial modes. The cavity is designed such that these modes are non-degenerate, and as such, the higher order modes do not resonate and are reflected from the cavity's input coupler. By this mechanism, pointing noise is converted into intensity noise. This intensity noise has occurred *before* the beamsplitter and is now common to both arms of the homodyne detector, allowing large CMRR of the balanced homodyne detector to remove this intensity modulation.

The modecleaner cavity also filters changes in mode shape, which may occur due to dust passing through the beam. Changes in the mode shape will also couple into intensity noise through the photodiode inhomogeneity. As with beam pointing, the modecleaner cavity will convert mode shape fluctuations into intensity fluctuations which can then be subtracted.

Once the mode cleaner was introduced, it was seen that air disturbances before the modecleaner did not result in low-frequency blow-outs. The experiment is still sensitive to pointing noise which occurs downstream of the modecleaner. By placing the modecleaner inside the homodyne detector system's steel tank, the steel tank then stabilised air currents and reduce dust in this section of the experiment, solving the issues of beam pointing and varying mode shape.

8.3.4 Parasitic Interference

Parasitic interference, also commonly known as a parasitic interferometer, was recognised as the limiting factor in the first measurements of flat shot noise across the entire audio-band [141]. Parasitic interference occurs when some light is scattered from the original beam path, through dust or surface imperfections, reflects off an object such as a mirror mount or another optical element, and re-enters the original beam path. Interference will occur between the original field and the scattered field at the point where these two fields overlap. Any change in the path length of the scattered field, caused by vibrations in the object that the scattered light is reflecting off or by the Schlieren effect will modulate the intensity of the light. If this modulation occurs after the beamsplitter then, much like beam pointing, it cannot be subtracted. Since the balanced homodyne detector is capable of measuring vacuum fluctuations, small fractions of a single photon on average per bandwidth Hz are clearly visible.

It is possible for the scattered light to exit the beam path completely upon scattering and it is possible for the scattered light to reverse direction but travel within the original beam path. If the scattered light exits the beam path, then careful placement of beam dumps will be enough to ensure that parasitic interference does not occur. However, if the scattered light does not exit the beam path, then it is more difficult to correct. This situation is shown schematically in Figure 8.8 for different scattering locations. The scattering is assumed to originate from either arm of the balanced homodyne detector and could occur at the photodiode or from one of the focussing lenses, illustrated in the Figure 8.8 as location 'S'. This *backscattered light* will traverse down the path of the main beam in the opposite direction. When the backscattered field scatters for a second time, it may again scatter into the beam path and then travel in the forward direction, resulting in interference between what we call the *forward scattered* field and the local oscillator field. The spurious interference converts motion of optics and air currents in the scattered beam path into intensity noise. Figure 8.8 shows the possible locations where scattering can occur. We discuss the effect that parasitic interference, originating from different locations, will have on the shot noise.

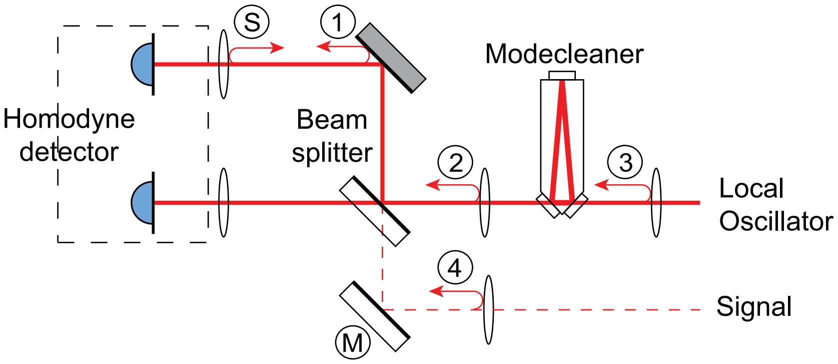

Figure 8.8: Scatter in the balanced homodyne detector leading to parasitic interference. The backscattering occurs in one of the detector arms, chosen here to be location S, and the scattered light travels along the beam path in the opposite direction. Forward scattering can then occur off a second surface, locations 1-4. The location of the forward scattering determines the effect on the balanced homodyne detector output, described in the text.

First we note that interferometric effects which occur between the beamsplitter and the laser source will result in intensity noise that is common to both arms of the balanced homodyne detector, which will be suppressed by the CMRR. This is the case for the forward scattering locations 2 and 3. Additionally, location 3 may be afforded some filtering effect by the modecleaner cavity. Parasitic interference in the experiment was detected here, and although it was not seen to negatively affect homodyne detector measurement (due to the CMRR being high enough to subtract these fluctuations) the ANU squeezer eventually had a Faraday isolator located near position 2 to remove interference at this location and ensure the CMRR was as high above the required level as possible. The forward scattering seen at location 1 will set up a parasitic interference in one arm of the balanced homodyne detector. The intensity noise on the optical field due to this parasitic interference is incident on only one photodiode, and hence cannot be subtracted. If the magnitude of this noise is large enough compared to the shot noise, then it will be seen in the output spectrum. The final location is forward scattering from location 4, in the path where the signal field enters the balanced homodyne detector setup. Scattering from this location will have a substantial impact since the balanced homodyne detector system is designed to be maximally sensitive to any light that enters through the signal port. Scattering in this path will interfere at the beamsplitter with the local oscillator field and the resulting intensity fluctuations will be anti-correlated in the two arms of the balanced homodyne detector, resulting in anti-correlated noise in each of the two photodiodes.

To determine whether parasitic interference was a limiting source of noise in our setup, shot noise spectra were taken with a beam dump in the signal port at location 4 in Figure 8.8 and with the signal port open but with no laser fields present in this path, shown in Figure 8.9. The beam dump was placed such that there were no optical components between it and the beamsplitter.

The difference between the shot noise for the two cases illustrated in Figure 8.9, with and without a beam dump in the signal path, is strong evidence for the presence of parasitic

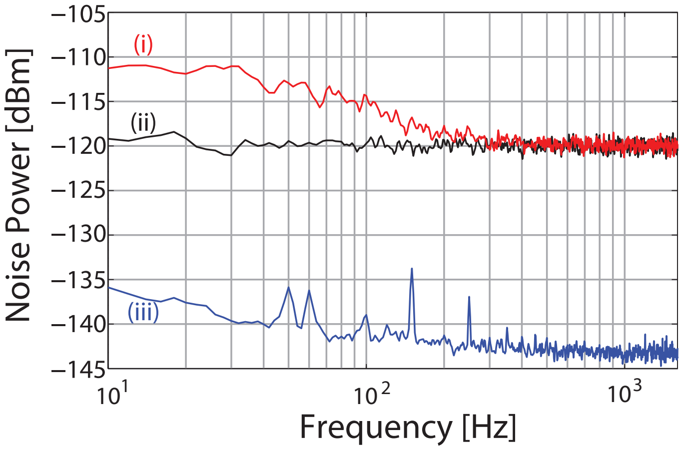

Figure 8.9: Parasitic interference from the signal port of the balanced homodyne detector. Only the local oscillator field was present. Trace (i) is the homodyne detector output with the signal port open, trace (ii) is the balanced homodyne detector output with the beam dump in place and trace (iii) is the dark noise of the balanced homodyne detector.

interference. A more conclusive method for determining the presence of scattered light is presented in § 8.3.5. Flat shot noise is seen when the beam dump is in place but excess noise is seen when it is absent. A Faraday isolator with approximately 22dB of isolation was inserted in place of the beam dump but the excess noise did not noticeably change, indicating that perhaps greater isolation is required or that scatter off the Faraday isolator itself was enough to cause these effects. The beam dump was moved up the signal path to try and determine if there was a single point where most of the forward scattering was occurring but it seemed to be a cumulative effect from several locations in this path.

8.3.5 Detecting the Presence of Parasitic Interference

Using a method known as opto-mechanical frequency shifting, or cyclic averaging, it is possible to determine with certainty whether a low-frequency roll-up is due to the presence of scattered light or otherwise [149]. This technique has been used in many situations to remove the noise from scattered light out of the detection band of interest [150, 151, 152]. The mirror M in Figure 8.8 is actuated with a PZT that is driven with a triangle wave. Now consider what happens to light that is scattered from position S, backwards to position 4, where a scattering plate has been introduced, and then forwards to the balanced homodyne detection. The PZT is set up such that it sweeps the phase of the scattered light through an integer number of cycles, time-averaging the scattered light to zero. The signal due to the motion of the scatter sources now appears at the dither frequency of the PZT and its harmonics. A simple classical model illustrates this effect. We start with an electric field, E, and write

$$E = A + Ce^{i\phi_s}, \tag{8.7}$$

where A represents the local oscillator field and we have chosen a reference frame such that we do not require a phase term for this field. The amplitude of the scattered light, C with phase ϕ_s, will interfere with the local oscillator field. The phase of the scattered

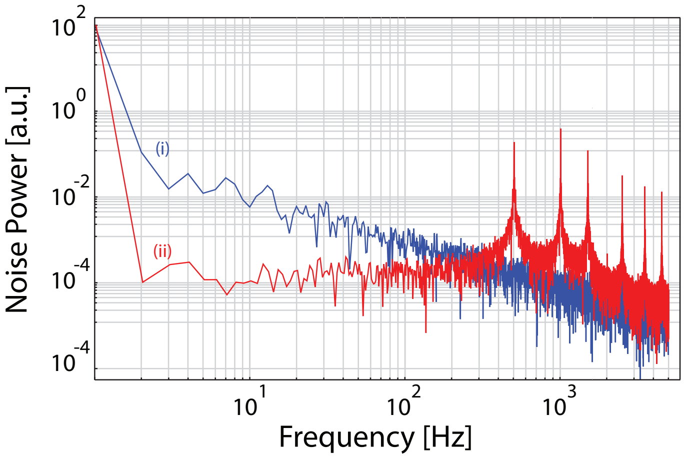

Figure 8.10: Simulated results of the cyclic averaging technique. Trace (i) shows the intensity noise of the LO field with some scattering present, resulting in a low-frequency roll-up. Trace (ii) shows that the low-frequency noise can be shifted up to the dither frequency and harmonics above it by driving a PZT in the scattering path with a triangle wave. Parameters are; local oscillator amplitude, $A = 1$, scattered light amplitude, $C = 0.01$, dithering frequency, $f = 500\,Hz$, and a standard deviation of the scattered phase of 0.01.

light is written

$$\phi_s = \sum R, \tag{8.8}$$

where $\sum R$ is the cumulative sum of normally distributed random noise about zero, with the standard deviation of this noise defining the degree of phase modulation due to air currents or mirror motion. The spectrum of such a field is shown in Figure 8.10.

In order to shift the intensity noise due to scattering out of the band of interest requires one to modulate the scattered field with a triangle wave. This provides a linear sweep on individual ramps, a necessary feature. The amplitude of this modulation is set such that one sweep of the dither progresses the phase an integer number of fringes. We can thus write for the dithered field

$$E_{\text{dither}} = A + Ce^{i\phi_d}, \tag{8.9}$$

where ϕ_d is the scattered phase plus the phase due to the dither. The phase of the field including the dithering is written

$$\phi_d = \phi_s + nD(f), \tag{8.10}$$

where n is the number of fringes wrapped by the dither and $D(f)$ is a triangle wave dither with some frequency, f. The spectra of the dithered scattered field is shown in Figure 8.10.

Figure 8.10 shows the spectra for the local oscillator field with scattered light present, trace (i), and with a PZT, dithered with a triangle wave present in the scattering path, trace (ii). The figure shows that even with scattering present, by dithering the scattered light we should be able to recover flat shot noise below the dithering frequency.

The experiment was then constructed as shown in Figure 8.8, with the mirror M being driven by a triangle wave. The amplitude of the dither was varied until the noise below the dithering frequency was at a minimum, this is the point at which the dither is shifting the phase by an integer number of fringes.

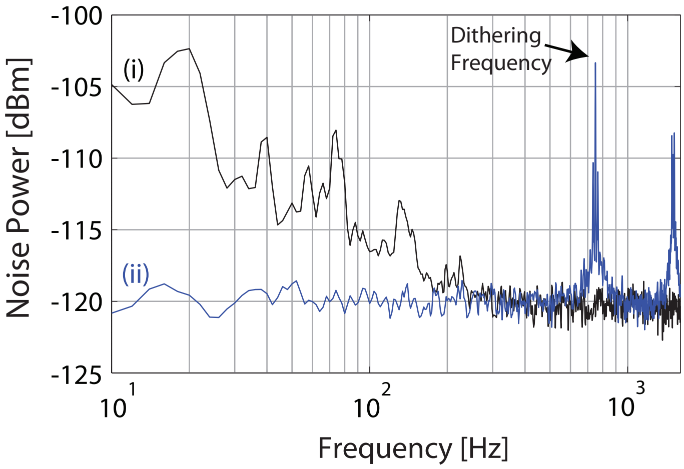

Figure 8.11: The cyclic averaging technique applied to the balanced homodyne detector with a scatter source placed in the signal path. Trace (i) shows the measured shot noise when a scatterer was placed in location 4 in Figure 8.8. With this scatterer in place, the PZT placed between this scatterer and the detector's beamsplitter was dithered at a frequency of 750 Hz. The amplitude of the dither was adjusted until all of the low-frequency noise was seen to shift up to the dither frequency and its harmonic as seen in trace (ii).

Figure 8.11 shows that the opto-mechanical frequency shifting-method has indeed confirmed the presence of scattered light in our setup. The scattered light noise has been mixed up to the dithering frequency and the shot noise is now flat below this frequency. This method has also provided additional information. The fact that the dithering results in flat shot noise has provided information on the location of the scattering and it signifies that the forward scatter originates in this beam path. If one were to move the position of the PZT in this beam path progressively further away from the balanced homodyne detector at some point it might be seen that the signal at the dither frequency decreased. This would indicate that scattering has not undergone the phase shifts introduced by the PZT and hence scattering has occurred nearer to the balanced homodyne detector than the current location of the PZT.

Parasitic interference can be overcome in 3 ways; by reducing the amount of scattering through the use of components with minimal surface roughness, by dumping the scattered photons through careful placement of beam dumps, and by reducing the phase fluctuations in the scattered fields through reduction of vibrations in the experimental setup. The use of super-polished optics and an enclosure around the entire experiment aids greatly in all of these endeavours.

8.3.6 Phase Jitter

The final detection issue is phase jitter. The effect that this has on the squeezing has been recognised previously by Takeno *et al.* [97]. Phase fluctuations on the vacuum squeezed field result in a rotation of the squeezed field relative to the local oscillator field. The phase control loop designed to control the squeezing angle, such as coherent locking, will provide some finite suppression of this rotation but some rotation will still occur. This rotation results in a suboptimal detection angle for the homodyne detector setup, resulting in the measurement of a noise projection that does not align with the squeezed quadrature. This is shown in Figure 8.12.

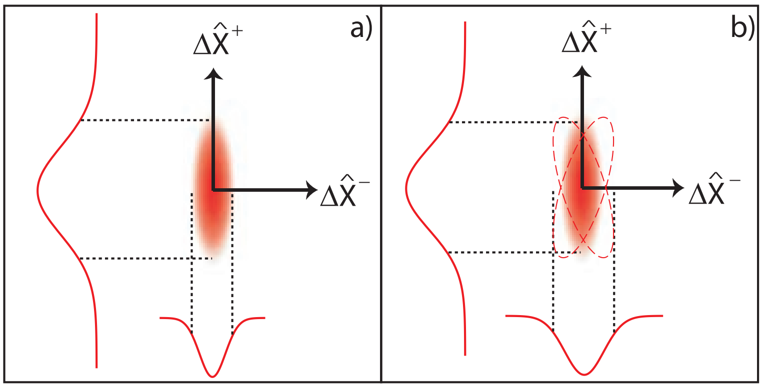

Figure 8.12: The effect of phase jitter on the measurement of a vacuum squeezed state. In case a) the phase is steady and measurement of either the amplitude or phase quadrature squeezed state, which is the projection onto one the quadrature axes, yields its properties. In case b), where the phase is fluctuating, and hence the squeezing ellipse is rotating, the projection of the state onto the two axes is averaged, resulting in different results to those found in the absence of jitter. In particular, the projection of the squeezing onto its axis, in this case the phase quadrature, increases. In the presence of phase jitter, the measured squeezing does not reflect the statistics of the original state.

Assuming some root mean square (RMS) fluctuations of the angle, determining the effect this has on the measured squeezing and anti-squeezing, $V^{\pm'}$, can be found via [97]

$$V^{\pm'} \approx V^{\pm}\mathrm{Cos}^2\theta + V^{\mp}\mathrm{Sin}^2\theta, \tag{8.11}$$

where $V^{\pm}$ is the squeezing/anti-squeezing level in the absence of phase jitter and θ is the rms phase fluctuations of the state. The larger the anti-squeezing, the greater the effect that phase fluctuations have. This is due to the fact that when rotated at the same angle, the projection of a longer ellipse will be proportionally larger for that rotation. This means that as the system is driven closer to threshold, and the anti-squeezing increases, it become increasingly important to stably control the phase of the squeezing relative to the local oscillator. The effect on measured squeezing due to phase fluctuations for an OPO with the ANU squeezer parameters is shown in Figure 8.13.

Figure 8.13 shows the degradation of measured squeezing for various rms phase jitter values. The squeezed state produced by this system mimics that we would expect from our ANU squeezer as the parameters have been chosen to match the ANU squeezer properties. We note that as the system gets closer to threshold, the rms phase jitter has a greater effect due to the increased anti-squeezing. The main source of phase jitter is changes in the refractive index of free space due to air currents, the Schlieren effect [75]. Hence the best way of reducing phase jitter is by reducing these air currents. The steel isolation tank placed around the detection part of the experiment helps in this regard but it is also

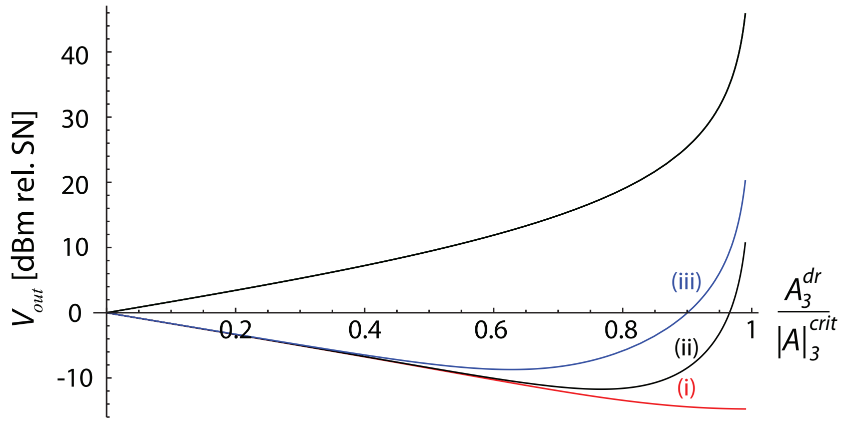

Figure 8.13: The variance at the output of an OPO as the system is driven towards threshold power, A_3^{crit}. The variance of the squeezing and anti-squeezing is shown for the same system with varying phase jitter of 0 degrees, trace (i), 1 degree, trace (ii) and 3 degrees, trace (iii). Parameters are; optical path length $L = 0.279\,\mathrm{m}$, non-linear interaction strength, $g = 1891$, reflectivity of the input/output coupler at the pump and fundamental wavelengths, $R^b_{co} = 0.722$ and $R^b_{co} = 0.839$, respectively, and intra-cavity loss at fundamental and pump, 0.26% and 4.6%, respectively.

necessary to place the rest of the experiment in an airtight (or close to airtight) enclosure in order to isolate the experiment from the typical air currents in the lab, as shown in Figure 8.15. Furthermore, optimisation of the locking loops, in particular increasing the gain at low frequencies, can aid in reducing the rms phase jitter of these states.

8.4 Squeezing from the ANU Squeezer

Now that the technical limitations to measuring shot noise and squeezing in the low-frequency regime are understood, we can move onto measuring these states of light. In this section, we will investigate the history of squeezing results from the ANU squeezer. In this way, we can directly see the effect that various changes to the setup has had. Shown in Figure 8.14 is the squeezing produced by the ANU squeezer over the course of two and a half years.

8.4.1 March 2009 Squeezing

The experiment at this time was in its early stages and many of the high quality components were not yet integrated into the table. Of particular importance is that the homodyne detector from the Max Planck Institute for Gravitational Physics had not yet arrived and in its place a voltage subtracting homodyne detector was used to measure all results. Low flicker noise resistors had not yet replaced the noisy carbon film resistors that were present from its original design. As such, low-frequency flicker noise accounted for much of the roll-up seen in the squeezing trace below about 2 kHz and also resulted in a shot noise measurement that was not flat across the entire spectrum (See § 8.2).

The squeezing magnitude was poor because a PPKTP crystal from Raicol with cheap in-house AR coatings was used. The loss on this crystal, using the method described in § 7.1.3 was found to be around 1.4 % per round trip at the fundamental frequency. This

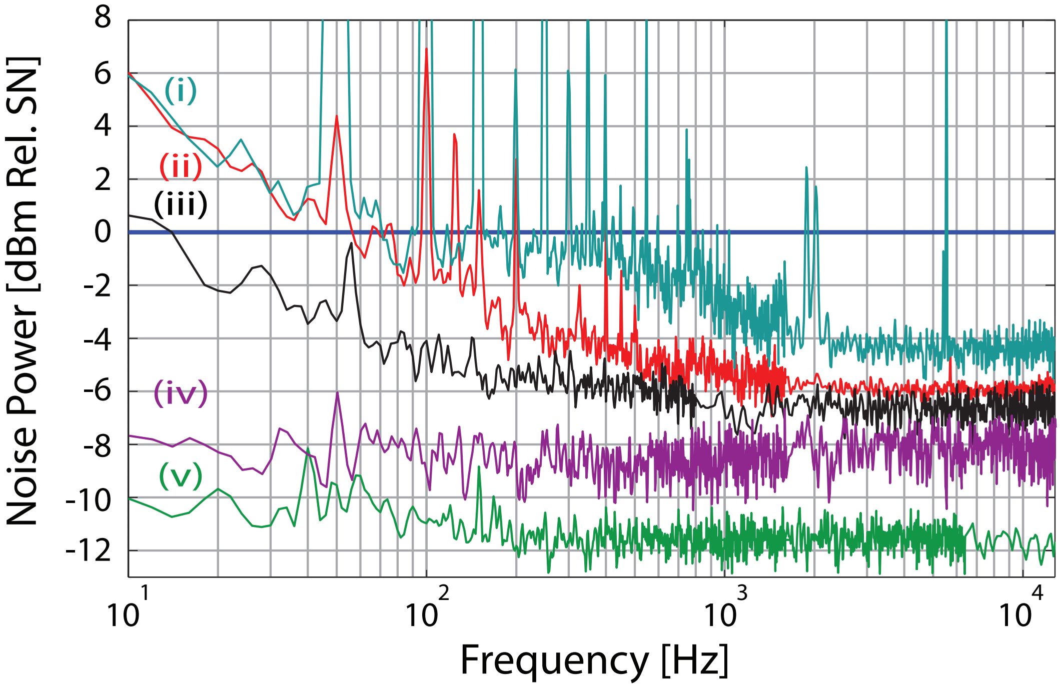

Figure 8.14: A snapshot of squeezing in the ANU squeezer over the years. (i) is the squeezing produced in March 2009 with a squeezing plateau (the lowest squeezing measured over some span) of 4.4 dB, (ii) is the squeezing produced in May 2009 that has a squeezing plateau of 6.0 dB, (iii) is the squeezing produced in January 2010 that has a squeezing plateau of 6.7 dB, (iv) is the squeezing produced in April 2011 that has a squeezing plateau of 8.6 dB and trace (v) is the squeezing produced in November 2011 with a plateau of 11.6 dB. Traces (i)-(iv) are constructed from two spans of 0-1.6 kHz (RBW = 2 Hz) and 0-12.8 kHz (RBW = 16 Hz). Trace (v) is constructed from three spans of 0-1.6 kHz (RBW = 2 Hz), 0-6.4 kHz (RBW = 8 Hz) and 0-102.4 kHz (RBW = 128 Hz). All traces have at least 100 averages except for traces (i) and (iv) which have 50. Dark noise has not been subtracted from any of the data. The dark noise clearance of traces (i) and (ii) was approximately 6 dB and the dark noise clearance of the remaining traces was greater than 10 dB as illustrated in Figure 8.16.

large loss value is enough to explain much of the very poor squeezing seen at this time, the theoretical effect of which can is discussed in § 5.6.

8.4.2 May 2009 Squeezing

The new components had still not arrived but much work had gone into increasing the stability of the locks. In particular, it was seen that noise was coupled into the squeezing at low frequencies via the coherent locking field. Low incident power levels, of 10s of micro-Watts hitting the CLF coupling mirror, were required in order to reduce this coupling to a level where the coherent field was not seen to degrade the squeezing (Theoretically investigated in § 7.4). Ground loops in these locks and the homodyne detector were also worked on, by having the detectors run from their own power supply which was plugged in at different locations until an optimum was found, such that the mains coupling into the measurements was drastically reduced. The phase lock between the primary and CLF lasers was also optimised by varying optical powers and electronic gains. These improvements resulted in much less low-frequency noise coupling, reducing the roll-up seen at low frequencies, and the increased stability of the locking reduced in an improvement in squeezing magnitude due to a reduction in phase jitter. At this stage, the homodyne detector performance was still limited primarily by the flicker noise. The shot noise at this stage still exhibited a low-frequency roll-up.

8.4.3 January 2010 Squeezing

Many changes were made at this time. A new OPO was constructed that had a higher beam height to replicate the needs of the LIGO squeezing injection. Following advice from Roman Schnabel, new PPKTP crystals that were provided by Raicol, superpolished by Photon LaserOptik GMBH (with a micro-roughness < 0.2rms) and coated by LaserOptik GMBH (with reflectivity $< 0.1\%$ at 1064 nm and $< 0.5\%$ at 532 nm) were ordered. One of these crystals was placed in the new cavity and the intra-cavity loss due to the crystal dropped to the value shown in Table 7.1 of 0.26%.

Much work had been done on a separate experiment to determine the sources of the roll-up seen in the shot noise at low frequencies as discussed previously in this Chapter. The experiment was very successful, and flat shot noise was achieved to below 10 Hz. Flicker noise (§ 8.2), beam jitter (§ 8.3.3), dust and parasitic interference (§ 8.3.4) were found to be the major contributors to low-frequency noise, agreeing with previous findings from prior experiments. At this stage, a new homodyne detector, designed and supplied by Henning Vahlbruch from the Max Planck Institute for Gravitational Physics [143] was swapped in for the previous homodyne detector.

With the introduction of a modecleaner cavity in the LO path, and an isolation tank around the detection components of the setup, the shot noise was finally measured flat down to below 10 Hz. Parasitic interference was present in the squeezing spectrum but was not seen in the shot noise spectrum due to the beam path of the squeezing being blocked when measuring the squeezing.

8.4.4 April 2011 Squeezing

In order to measure flat squeezing then required comprehensive work on the reduction of parasitic interference locations which were initially believed, and later confirmed, to be a major source of noise (See § 8.3.4). It was also postulated that phase jitter may be playing a role in degradation of squeezing, however, it was difficult to confirm this postulate the second harmonic generator would often not produce enough power to reach threshold, where the phase jitter can be measured (See § 8.3.6). A semi-air-tight enclosure was built around the optical table in order to simultaneously reduce phase noise, beam jitter and protect the entire experiment from dust. The enclosure is shown in Figure 8.15.

At this stage, one of the ETX500 diodes in the homodyne detector had failed and was replaced. The efficiency of a number of these diodes were compared to one another and the one with the highest quantum efficiency was chosen. Between diodes from the same batch, only minor variance in efficiency was found, but a recently ordered batch of diodes showed an efficiency of approximately 10 % less than the ones in the older batch (ordered at least 1 year prior). The reduction of parasitic interference, and the box around the table, resulted in the first measurements of flat squeezing. Unfortunately, phase jitter on the beam was not measured at this time so it is difficult to say how much of the improvement in squeezing was due to the new diode, which could not be compared with the broken one, and how much was due to reduced phase jitter, as there was not enough power to get

Figure 8.15: The box encasing the ANU experiment. The primary purpose is to reduce air currents, which in turn reduces noise coupling of beam pointing and phase jitter. It also protects the experiment from dust.

close enough to threshold to characterise it sufficiently. In any case the enclosure certainly aided in stabilising the locks and reducing phase jitter.

8.4.5 November 2011 Squeezing

The final improvement to the experiment was the replacement of Epitaxx ETX500 photodiodes with high quantum efficiency (quoted at $> 99\%$) photodiodes from Laser Components GmbH. These photodiodes were measured to have a quantum efficiency which was approximately 4 % greater than that of the ETX500's. This was determined by constructing a small experiment in which a laser beam was incident on a beamsplitter, with one output field directed towards a detector where the diodes were switched in and out of the same electronic circuit, and the second output field directed towards a reference detector. As expected, this reduction in loss resulted in the detection of much more squeezing with greater purity. The full measurement of this squeezing is shown in Figure 8.16, illustrating the purity, flat shot noise, and dark noise clearance. The optical parametric oscillator was operated with 90 mW of input power (76 % of threshold). The expected propagation loss on the squeezed state is approximately 0.7 % and the balanced homodyne detector had a visibility of 99.4±0.2 %. The squeezing is seen to degrade slightly below 200 Hz due to the presence of parasitic interference that could not be removed. Small factors, such as the slightly altered detector alignment after the diodes were replaced, can have a large effect on the parasitic interference in the experiment and after this change there was difficulty in reducing interference such that it did not degrade the squeezing measurement.

Figure 8.16 shows that with a local oscillator power of approximately 1.9 mW, the shot noise of our detector is greater than 20 dB above the electronic noise. The anti-squeezing is 17.5±0.4 dB above the shot noise and is flat. Below 200 Hz, 10 dB of squeezing is seen and above this frequency 11.6±0.4 dB of squeezing is observed. The measurement shows that noise due to parasitic interference was suppressed down to a level approximately 10 dB below the shot noise. Correcting for dark noise (see § 8.5), the squeezing level becomes 11.9±0.4 dB.

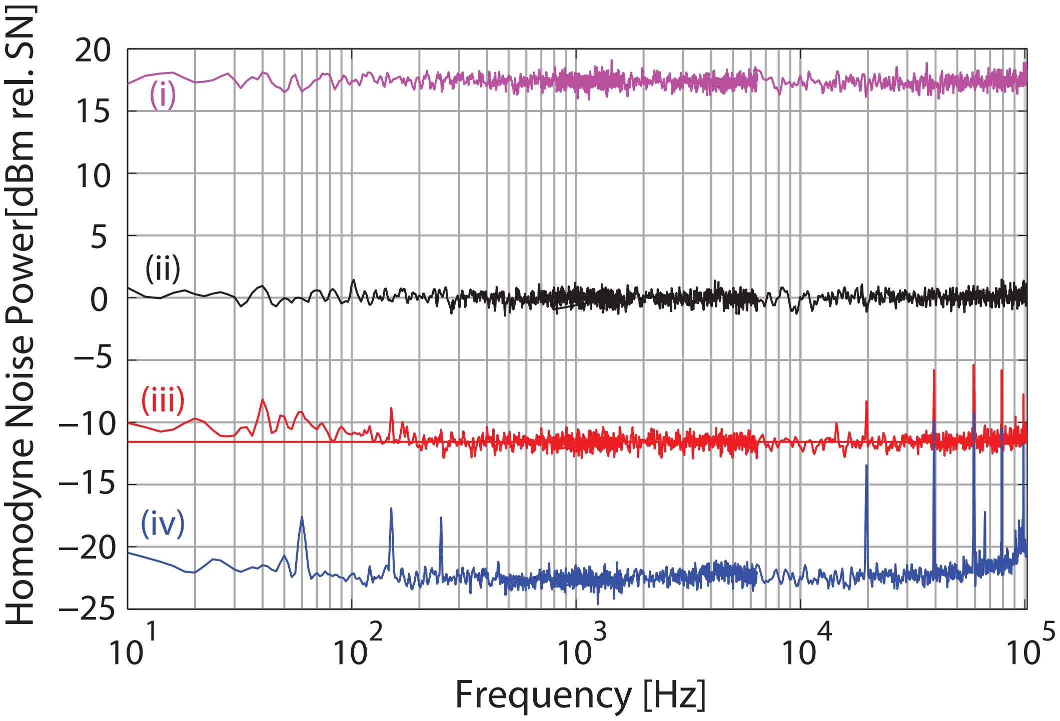

Figure 8.16: Measured squeezing from the ANU squeezer using quantum noise limited balanced homodyne detection showing the anti-squeezing (i), shot noise (ii), squeezing (iii), and dark noise (iv). A red line at -11.6 dB has been added to show the average of the squeezing from 1.6 kHz to 6.4 kHz. All traces are pieced together from 3 FFT windows: 0-1.6 kHz, 0-6.4 kHz, 0-102.4 kHz with 800 FFT lines, resulting in resolution bandwidths of 2 Hz, 8 Hz, and 128 Hz respectively. 100 RMS averages were taken for all traces. Dark noise has not been subtracted from the data.

8.4.6 Correcting for Detection Losses

Using the measured squeezing and anti-squeezing levels, we can infer the total loss on the state by assuming production of a pure state and determining the losses that result in the measured data. This value provides an estimate to the amount of squeezing injected into an interferometer, as the detection scheme is bypassed when the squeezed state is directed towards the interferometer. We can write for the measured squeezing, Sqz[dBm], and measured anti-squeezing, Asqz[dBm],

$$\begin{aligned} \mathrm{Sqz[dBm]} &= 10 * \mathrm{Log}_{10}\left[10^{\mathrm{Sqz}_0/10}\eta_{tot} + (1-\eta_{tot})\right] \\ \mathrm{Asqz[dBm]} &= 10 * \mathrm{Log}_{10}\left[\frac{1}{10^{\mathrm{Sqz}_0/10}}\eta_{tot} + (1-\eta_{tot})\right]. \end{aligned} \tag{8.12}$$

We then simultaneously solve these equations for the total detection efficiency, η_{tot}, and pure intra-cavity squeezing, Sqz_0. This equation accounts only for propagation losses and does not account for other detection issues such as phase jitter. The measured squeezing, Sqz[dBm], should be corrected for dark noise and the initial squeezing is the theoretical value of the squeezing before exiting the cavity. Multiplying Sqz_0 by the escape efficiency results in the amount of squeezing exiting the OPO. Using the measured values from

Figure 8.16, a total loss on the squeezed state of 0.048 ± 0.004 is found, which agrees well with the expected losses. After accounting for the escape efficiency of 0.985 ± 0.001, the amount of squeezing exiting the cavity is found to be approximately $15.0\pm0.1\,$dB.

Chapter 9

The LIGO Injection

In this section the LIGO injection experiment is introduced. This project was a large international effort most notably involving the LIGO Scientific Collaboration, the ANU, the Max Planck Institute for Gravitational Physics, Caltech and MIT. The main focus of the input from the ANU was to supply a suitable squeezer, and as such, detail is directed towards the performance and properties of the squeezed light source. This squeezed light source was designed and constructed by Sheon Chua, Conor Mow-Lowry, Sheila Dwyer and I at the ANU. My personal responsibilities were in the design of the cavity geometry, modelling of the non-linear interactions, and investigation of noise sources in the balanced homodyne detection scheme.

The results of the LIGO injection experiment are then revealed. The injection experiment involved many people from all of the aforementioned institutions and will be detailed in the paper soon to be released on this work [153]. My contribution to this experiment was to firstly produce, as part of the group at the ANU, a travelling-wave squeezer that met strict performance benchmarks. Once this was achieved at the ANU, I then spent 6 months at MIT with Sheila Dwyer under the supervision of Prof. N. Mavalvala and Dr. D. Sigg building and characterising a replica of the ANU system. Finally, I spent approximately 2 months aiding in the integration of this squeezer with LIGO in Washington state. During this time I aided in integrating and characterising the squeezer, integrating the control electronics and taking the first measurements of the squeezing enhanced interferometer.

Further information on noise sources, scattered light measurements and interferometer performance with squeezed light injection will be given in more detail by Sheon Chua and Sheila Dwyer in their theses as well as future LIGO working notes and additional papers that are currently under construction.

9.0.7 LIGO Injection Aims

Squeezed light has already been shown to reduce the shot noise in interferometers, including the GEO600 device [68]. The aim of the LIGO H1 injection was not to demonstrate that squeezing could reduce shot noise, instead the goals were to investigate noise, scattered light and integration issues in the more sensitive LIGO interferometer. In particular, the sensitivity of LIGO at frequencies below about 500 Hz allows for investigation of these phenomena at low frequencies, inaccessible in previous experiments. With LIGO H1, it could be ensured that the reduction of shot noise through the injection of squeezed light did not degrade the performance of the device at lower frequencies. It was also decided that it would be beneficial to test a travelling wave bow-tie OPO geometry to complement the findings from GEO600, where a linear OPO geometry was used [100, 120]. The experimental setup for the injection of squeezed states into H1 is shown in Figure 9.1.

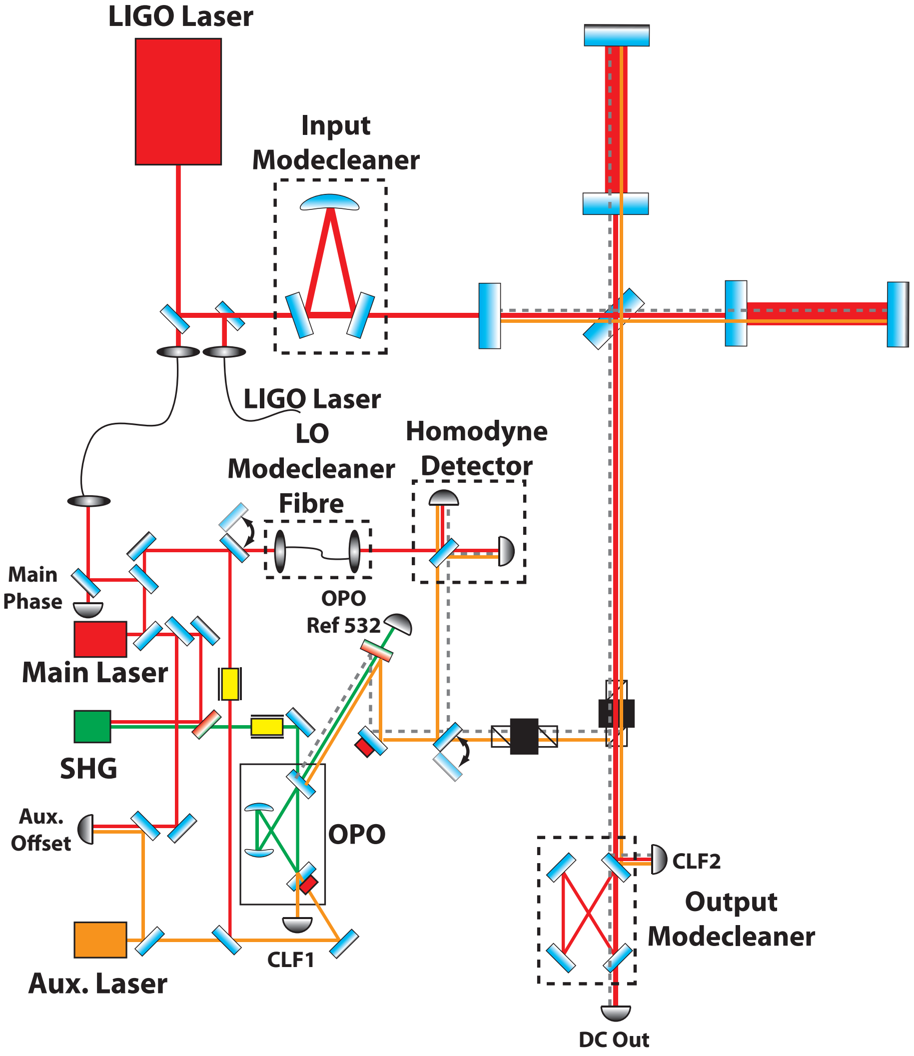

Figure 9.1: Schematic of the squeezed light injection experiment into H1 at LIGO. Pump field is in green, main laser and LIGO laser are both in red, the auxiliary laser is in orange and the squeezing is denoted by a dashed grey line. Full description in text.

The LIGO injection scheme involves three laser sources. The LIGO laser [154], the main squeezing laser (a decommissioned LIGO laser source operating without the amplifier [155]), and an auxiliary laser (Lightwave) for coherent control of the vacuum squeezed state. The phase of the main laser is locked to the phase of the LIGO laser by directing a tap-off from the LIGO laser into a fibre and beating this with a small amount of light from the main laser. Most of the main laser power is directed towards an SHG cavity, where the 1064 nm light is frequency doubled to 532 nm. The SHG cavity was provided by the Max Planck Institute for Gravitational Physics using the same design as that described in [143]. The pump field is incident on the coupling mirror of the OPO. The 532 nm field is then transmitted through a dichroic mirror while the squeezing and auxiliary beams are directed towards either the homdodyne detector or the LIGO interferometer. The transmitted 532 nm light is detected in order to derive a PDH locking signal for the cavity length. The light from the main laser which is not used for SHG can be passed through a fibre optic cable and used as the local oscillator for the balanced homodyne detector. The fibre optic cable works in much the same way as the modecleaning cavity introduced in Chapter 8 to reduce beam pointing noise. Alternatively, a tap-off from the LIGO laser, directed through a second 100 m long fibre, could be used as the local oscillator for the homodyne detector by swapping the fibre connections at the end of modecleaner fibre setup, this fibre is marked as the LIGO laser LO. The LO from the LIGO laser could ideally be used to characterise the phase lock between the main laser and the LIGO laser when measuring squeezing, although the fibre noise in this LO plays a significant role. With the use of a flipper mirror the main laser field, instead of being used as the LO, can be directed towards the coherent locking coupling mirror in order to seed the OPO for gain and visibility measurements. A tap-off is also used to lock the frequency offset of the auxiliary laser to the main laser.

The auxiliary laser, which is frequency offset locked to the main laser, enters the OPO cavity through the coherent locking mirror. Within the cavity, it senses the non-linear interaction and a sideband field is generated. The reflected auxiliary laser and some small portion of the intra-cavity field is then detected at CLF1 and used to derive the first half of the coherent locking scheme. The auxiliary field and the generated sideband field also transmit through the OPO input coupler, along with the squeezed field, propagating through one Faraday isolator and reflecting off a second isolator, entering the interferometer. When it returns from the interferometer, the coherent locking field reflects off the output mode cleaner and is detected at CLF2. This field is used to derive the locking signal for the second half of the coherent locking. The squeezing passes through the output mode cleaner and is detected at the DC output of the interferometer. This detector is where the gravitational wave signals are also detected. The presence of squeezed light at this detector reduces the shot noise, thus increasing the sensitivity of the interferometer.

9.1 LIGO Squeezer Properties

The LIGO cavity was constructed taking into account the experience provided by the ANU prototype. The major differences were the purchase of higher quality cavity mirrors and the reflectivity of both the pump and squeezed fields on the input/output coupler. It was decided that the high escape efficiency of the ANU squeezer was not necessary for the LIGO cavity, seeing as losses inside the interferometer would limit the enhancement of the squeezing anyway, and as such the reflectivity of the input coupler at the fundamental was increased slightly. Whilst this decreases the escape efficiency, it also decreases the threshold power, reducing photothermal effects and increasing the thermal stability of the OPO slightly. Unfortunately, the modified coherent locking scheme was not developed in time to implement it in this experiment.

9.1.1 Mirror Properties

For reference, the properties of some of the intra-cavity mirrors and coatings bought from Advanced Thin Films are shown in Table 9.1. These mirrors were coated using the Ion Beam Sputtering (IBS) method and are of higher quality than those used in the ANU experiment.

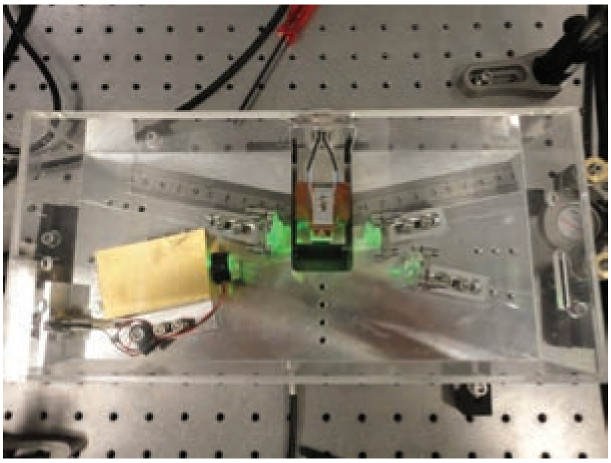

Figure 9.2: The LIGO squeezer, an almost exact replica of the ANU squeezer design.

Mirror Parameter	Value	Units
532 nm HR Reflectivity	>99.99%	-
1064 nm HR Reflectivity	>99.9%	-
532 nm AR Reflectivity	<0.2%	-
1064 nm AR Reflectivity	<0.1%	-
1064 HR Coating Absorption	<0.001%	-
RoC	-38	mm
Substrate Surface Roughness (Curved Surface)	<0.1	nm

Table 9.1: Specified mirror properties for the curved HR OPO mirrors from the manufacturer. The back of the mirrors are AR coated to allow for the injection of fields through these mirrors. All coatings are for an angle of incidence of 6 degrees.

9.1.2 Threshold

The threshold power of the system was measured using the same method as introduced in § 7.1.2. The mode matching of the pump field to the cavity was 74.5 %. The best fit to this data results in a threshold of 75.0±0.1 mW for the amplification regime and a threshold of 74±0.1 mW for the de-amplification regime. Using this information, we can determine the non-linear interaction strength, g, using Equation 5.36. We find that the non-linear interaction strength is 1880 $\pm 9\, s^{-\frac{1}{2}}$, which is very similar to the value found for the ANU squeezer. We expect this to be the case owing to the fact that the geometry of the two squeezers is nearly identical.

9.1.3 Losses

Using the same method as that shown for the ANU squeezer (see § 7.1.3), the reflected power of a seed directed into the front coupler was found to be 84.8 % after correcting for mode matching and dark noise. This results in an intra-cavity loss of 0.0056 ± 0.0001 for the squeezed field. The loss of this cavity was also measured by constructing the cavity without the crystal. The reflected power from the cavity without the crystal loss was 88.8 % after correcting for mode matching and dark noise, resulting in an intra-cavity loss of 0.0041 ± 0.0001. From these values, we can infer that the total crystal loss, consisting

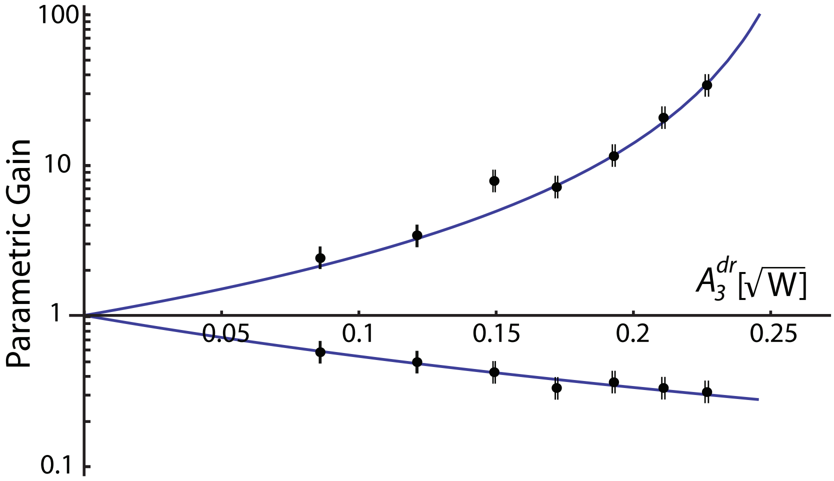

Figure 9.3: Parametric gain as a function of pump amplitude for the LIGO squeezer. The points are the data and the blue curve is the best fit to Equation 5.52.

of the two AR coatings and the absorption, is 0.0015 ± 0.0002. These losses, coupled with the reflectivity of the coupling mirror, of 0.868 ± 0.009, result in an escape efficiency of the cavity of 0.961 ± 0.002. The uncertainty is dominated by the uncertainty in the measurement of the coupling mirror reflectivity by the power meter.

The same process was repeated for the pump field. The reflected power of the pump directed into the front coupler was found to be 61.8 % after correcting for mode matching and dark noise. This implies an intra-cavity loss of 0.039 ± 0.001 for the pump field. The reflected power of the cavity without the crystal loss was 72.7 % after correcting for mode matching and dark noise. This results in an intra-cavity loss of 0.026 ± 0.001. From these values, we can infer that the total crystal loss for the pump, consisting of the two AR coatings and the absorption, is 0.013 ± 0.002.

9.1.4 Cavity Parameters

Table 9.2 shows the parameters of the LIGO squeezed light source. The main difference between this cavity and the prototype ANU cavity is the increase in reflectivity of the input/output coupler at the fundamental wavelength. As expected, this reduced the threshold of the LIGO cavity to 75 mW but also decreased the escape efficiency to 96.1 %.

9.1.5 Squeezing

The squeezing produced by the LIGO squeezed light source is illustrated in Figure 9.4. The squeezer was operated with 850 μW of local oscillator and 50 mW of pump light. The homodyne detector is the same as that used in the ANU squeezing experiment, with ETX500 diodes, and the dark noise lies greater than 20 dB below shot noise.

Figure 9.4 shows that the squeezing plateaus at 5.6±0.4 dB below the shot noise above 1 kHz and the anti-squeezing is 8.8±0.2 dB above shot noise. Using the methods detailed in §8.4.6, the total detection efficiency is found to be 81.4 %. This implies that there is 8.4±0.1 dB of squeezing exiting the cavity. Much of this loss can be attributed to the ETX photodiodes, which we expect to have a quantum efficiency anywhere from 86 % to

Cavity Parameter	**Symbol**	**Value**	**Uncert.**	**Units**
Fundamental Wavelength	λ_1	1064	-	nm
Second Harmonic Wavelength	λ_3	532	-	nm
Input/Output Coupler Fundamental Reflectivity	$R_1^{in/out}$	0.868	0.009	-
Input/Output Coupler Pump Reflectivity	$R_3^{in/out}$	0.696	0.002	-
Coherent Locking Mirror Reflectivity	R_1^{cl}	0.998	-	-
PPKTP Loss for Fundamental	T_1^{cr}	0.0015	0.0002	-
PPKTP Loss for Pump	T_3^{cr}	0.013	0.002	-
Total Intra-Cavity Loss for Fundamental	T_l^a	0.0056	0.0001	-
Total Intra-Cavity Loss for Pump	T_l^b	0.039	0.001	-
Finesse at Fundamental	$\mathcal{F}_1$	42.5	1.5	-
Finesse at Pump	$\mathcal{F}_3$	15.6	0.1	-
Linewidth at Fundamental	$\Delta\nu_1$	26	1	MHz
Linewidth at Pump	$\Delta\nu_3$	70.0	0.7	MHz
Auxiliary Laser Detuning	Δ_{Aux}	29.8	-	MHz
Optical Path Length	L	0.279	0.001	m
Threshold Power	P_3^{crit}	75	0.1	mW
Escape Efficiency	η_{esc}	0.961	0.002	-
Non-linear Coupling Strength	g	1880	9	$s^{-\frac{1}{2}}$
Curved Mirror Radius of Curvature	RoC	-38	-	mm

Table 9.2: Properties of the LIGO squeezer. The loss values given are the transmission values of loss equivalent high reflectivity mirrors. Uncertainties are given for measured values.

96 % (See § 8.4.5). The degradation in squeezing below about 1 kHz is believed to be due to parasitic interference, however, due to time constraints on the project there was not enough time to hunt down the noise sources at these frequencies.

9.2 LIGO Enhancement

Figure 9.5 shows the LIGO strain sensitivity both with, blue trace (ii), and without, red trace (i), squeezed light enhancement. The sensitivity of LIGO has been increased by up to 2 dB in the shot noise limited regime. As expected, the amount of sensitivity improvement diminishes at lower frequencies. Importantly, the sensitivity of the device is not seen to decrease in the low-frequency regime, below about 200 Hz. This is an important result. It shows that scatter, electronic noise couplings and any other noise coupling mechanism has not degraded LIGO's performance at low frequencies. It also indicates that the increase in radiation pressure, the dominating quantum noise source at these frequencies, due to the presence of phase quadrature squeezing is still well below other noise sources. This is not expected to be the case for aLIGO, as shown in Figure 2.5.

9.2.1 Injection Losses

The main limitation to the amount of sensitivity improvement in this experiment was the losses on the squeezed state within the interferometer. One of the major sources of loss were the Faraday isolators in the path of the squeezed field. Each of the Faraday isolators, shown in Figure 9.1, introduced a 6 % loss upon transmission. The Faraday isolator in the LIGO output path is also traversed twice by the squeezed field, doubling this loss.

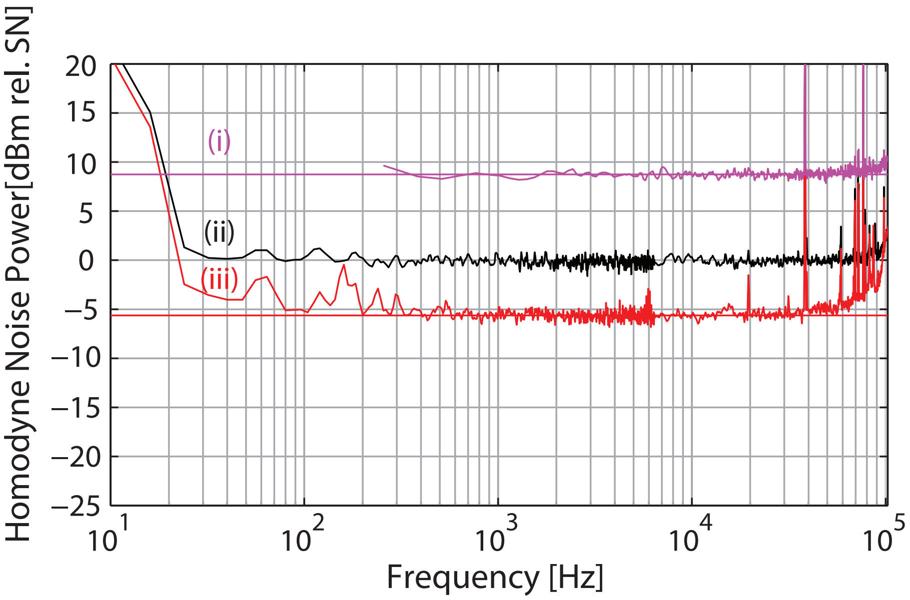

Figure 9.4: Measured squeezing from the LIGO squeezer using a quantum noise limited balanced homodyne detector showing the anti-squeezing (i), shot noise (ii), and squeezing (iii). A red line at -5.6 dB has been added to show the average of the squeezing from 1 kHz to 6 kHz. The shot noise and squeezing traces are pieced together from 2 FFT windows: 0-6.4 kHz, and 0-102.4 kHz with 800 FFT lines, resulting in resolution bandwidths of 8 Hz and 128 Hz respectively. The additional noise seen below 30 Hz is due to DC noise entering the measurements due to the large resolution bandwidths. The anti-squeezing trace has a 0-102.4 kHz bandwidth with 800 FFT lines and a bandwidth of 128 Hz. The first few data points have been removed. 100 RMS averages were taken for all traces. Dark noise has not been subtracted from the data.

The propagation efficiency between the squeezing cavity and the output mode cleaner was measured both in chamber with a power meter at various locations and using the power calibrated CLF2 diode from Figure 9.1 whilst under vacuum. The propagation efficiency determined by both of these measurements agreed and was found to be approximately 80 %.

The element producing the most loss was the output mode cleaner. The transmission through this cavity was measured for a well matched mode and was found to be 82 %. Mode matching to this cavity is difficult because it is near impossible to mode match with the interferometer at full power, therefore it is done at low power and then the power is increased to operational levels. Thermal effects, particularly thermal lensing, from the increased circulating laser power will alter the mode matching when moving from low power to standard operating conditions. The mode matching was measured in a low power configuration to be 74 %. These losses result in a total loss on the squeezed state of approximately 48 %. As shown in Figure 3.8, the most squeezing we could ever hope to measure with a 50 % loss is 3 dB. A more complete summary of these results is expected to be available in the near future [156].

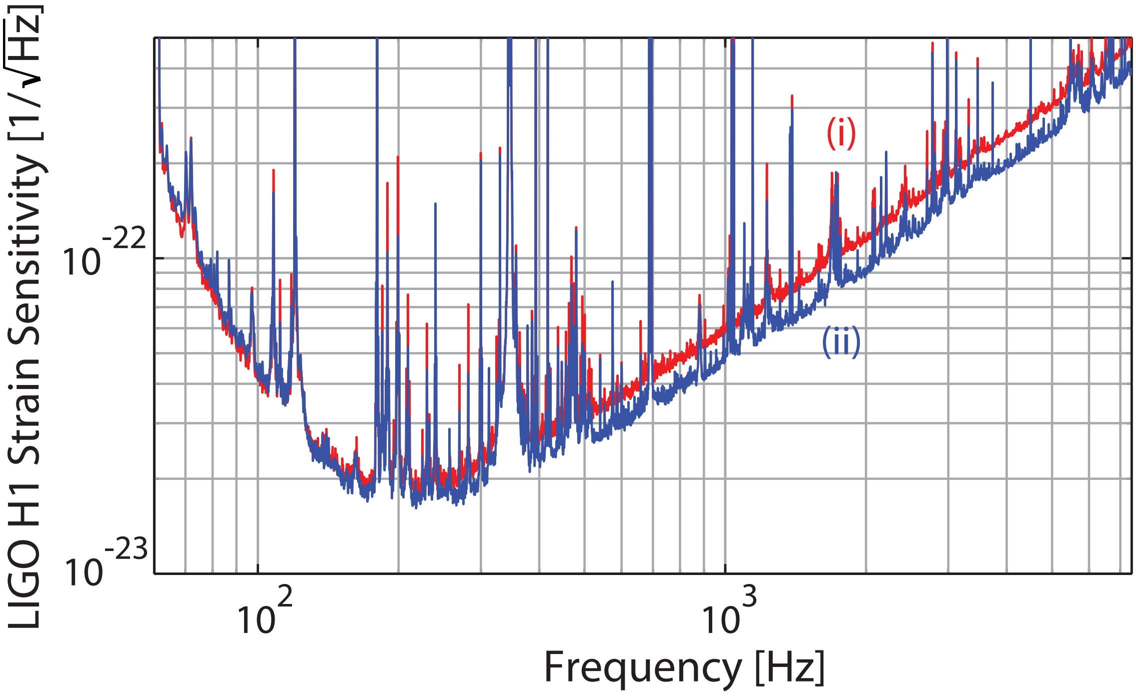

Figure 9.5: LIGO H1 detector squeezing sensitivity without, (i), and with, (ii), squeezing enhancement. Trace (i) shows the typical 6th science run (S6) operating sensitivity.

9.2.2 Travelling Wave Cavity Backscatter Isolation

It was previously mentioned that each pass through the Faraday isolator resulted in an approximately 6 % loss on the squeezed state. Figure 9.1 shows that the squeezing passes through one Faraday isolator before it enters the beam path of the interferometer's field. This isolator is placed in this location in order to reduce backscatter from the interferometer travelling towards the squeezer. The isolator is critical in ensuring that no scattered light re-enters the interferometer, which would reduce the sensitivity of the device.

In the GEO600 squeezed light experiment, where a linear OPO was used, two Faraday isolators were required in this path to reduce the scattering to an acceptable level [68]. The second Faraday isolator adds additional loss to the squeezed state, reducing the amount of squeezing injected into the interferometer. The travelling wave design used in the LIGO H1 experiment provides isolation to backscattering of greater than 40 dB, which is on par with the isolation offered by a single high-quality large-aperture Faraday isolator [102, 157]. The advantage of the travelling wave cavity is that this isolation is gained without introducing the additional losses of the Faraday isolator. As squeezing becomes a common technique for enhancing the sensitivity of gravitational-wave detectors, effort will be focussed towards decreasing the loss on the squeezed state. As the losses within the interferometer are reduced, the loss due to the Faraday isolators will become increasingly significant.

Chapter 10

Conclusions and Further Work

In this chapter, brief summary of the key results resulting from the ANU squeezer experiment and the H1 LIGO squeezed light injection are provided. From these results, a number of future goals and investigations are identified.

10.1 Summary of Squeezed Light Generation and Control for Gravitational-Wave Detection

- An optical parametric oscillator was designed and constructed as a prototype for the H1 squeezing experiment. The cavity was different to previous designs used in the enhancement of interferometers in that it was a doubly resonant, travelling wave system. Importantly, the travelling wave design was expected to provide a high level of immunity to backscattered light from integration into an interferometer and indeed this was found to be the case. A detailed discussion of the final cavity parameters was presented, and with them the reasoning behind choosing these parameters. Even with the additional intra-cavity loss introduced by the travelling wave design, this squeezer attained record levels of squeezing in the audio band. Down to 200 Hz the squeezing was directly observed at 11.6 dB below shot noise. Parasitic interference degraded the squeezing below this frequency but even so, 10 dB was still directly observed at 10 Hz. The progression of the squeezing results over the life of the experiment was presented and the steps taken to improve these results were discussed.

- A brief investigation of coherent locking was presented. Using the cavity equations of motion, the coherent locking scheme was modelled as a non-degenerate optical parametric oscillator and, using this method, the field amplitudes and phases were determined. It was found that one half of the coherent locking scheme was limiting the stability of the entire system and an alternative solution to this locking loop proposed. This alternative solution required second harmonic generation of the coherent locking field but allowed for the optimisation of this lock without negatively affecting the squeezing, as was found to be the case for the original scheme.

- An investigation into the various noise sources limiting low-frequency balanced homodyne detection was presented. Most of these noise sources had previously been identified but this work discussed all known noise sources and how they relate to each other. A method for detecting and eliminating parasitic interference was presented and the technique was experimentally shown to work as expected. The methods used to overcome the remaining noise sources was presented.

- Finally, a replica of the ANU squeezer was built in the United States and later moved to the LIGO Hannford site. The team at the LIGO site then installed and operated this squeezer in order to enhance the sensitivity of the device to levels never before seen. The noise couplings and integration issues were investigated by the science team at Hanford and will be detailed in later work and the theses of Sheon Chua and Sheila Dwyer.

10.2 Further Work

With the work presented in this thesis, a squeezing goal set around a decade ago has been reached [60, 49]. Squeezing of 10 dB down to frequencies of 10 Hz have been directly observed and should soon become readily reproducible. With the current amount of loss in gravitational-wave detectors, squeezed states of greater magnitude provide very little additional benefit over states such as the one presented here. This illuminates the fact that progression in this field of squeezed states for gravitational-wave detection needs to move towards the investigation of integration and stability, rather than squeezing magnitude. A number of issues that will need to be addressed in the near future are discussed below.

10.2.1 Squeezing Stability

As explained in § 7.4.2, the coherent locking field does not strictly lock to the angle of squeezing. It locks to some arbitrary angle that we choose to align to the angle of the squeezing. It was also discussed that the phase reference can drift, with changes in the temperature of the non-linear medium for example, and this will reduce the amount of squeezing enhancement in the interferometer. Ideally, the squeezer should provide stable squeezing for as long as possible in order to minimise the impact of integration on a fully operational gravitational wave detector. This will require further investigation along the lines of work previously conducted by Khalaidovski [140], possible introduction of a digital control loop to ensure the squeezed light angle does not drift over time, or perhaps the development of a new locking scheme. Further investigation into the coherent locking model presented in this thesis will aid in understanding the direction that needs to be taken.

One possible avenue for improving squeezed state control is to investigate the integration of a phase-matching locking loop into the system [158]. This technique reads out the phase matching condition from within the non-linear medium and if it were somehow integrated, perhaps by use of the frequency shifted auxiliary laser, then it might be able to increase the temperature stability of the system, thus stabilising the angle of the squeezing [140].

10.2.2 Dithering to Remove Parasitic Interference

It was shown in § 8.3.4 that noise due to parasitic interference could be averaged out at lower frequencies and shift the noise up to higher frequencies by dithering the phase of the scattered light. In this case, a mirror was placed in the beam path of the squeezing and therefore dithering of this mirror whilst attempting to measure squeezing would introduce a source of phase jitter, reducing the measured squeezing. By placing a second mirror in the path and feeding-forward the dither to the local oscillator phase, it should be possible to have the squeezing and local oscillator follow each other. This would allow one to measure the full amount of squeezing, whilst still removing the noise due to the scattered light from the detection band. An investigation into whether this technique would be viable in a gravitational wave detector would be beneficial.

10.2.3 Noise Coupling of the Coherent Locking Field

It was mentioned in § 7.4.1 that as the coherent locking field power was increased, the squeezing was seen to degrade. The reason for this is believed to be due to the presence of intensity noise on the coherent locking field, but further investigation into the matter is required. By understanding how the power of this field leads to degradation in the squeezing, it might be possible to increase the performance of the coherent locking scheme by finding ways in which the generated field can be maximised.

10.2.4 Frequency Dependent Squeezing

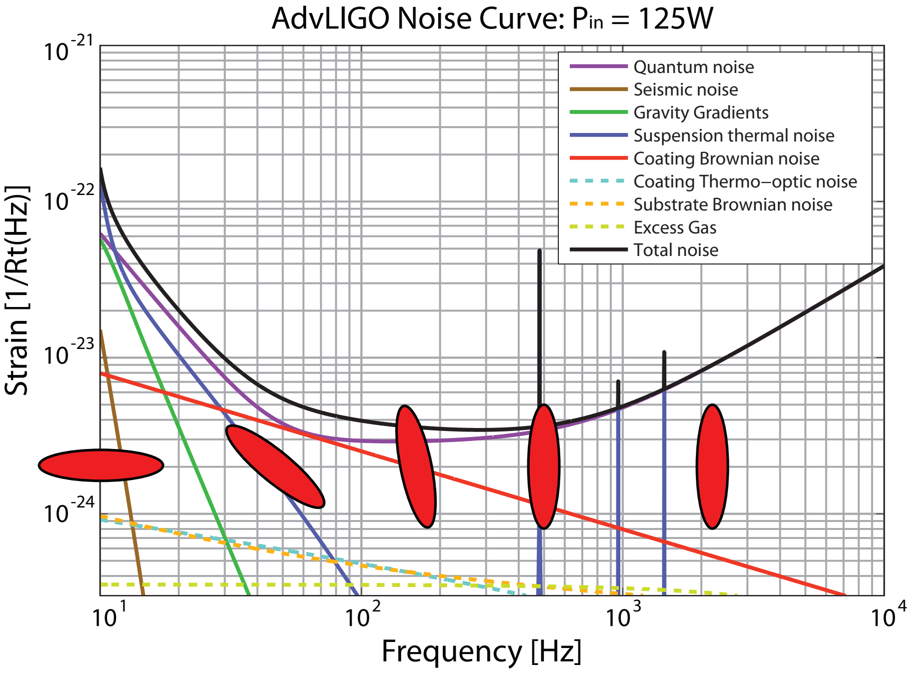

Figure 10.1: The Advanced LIGO expected noise budget showing roughly how frequency dependent squeezing would integrate. The red ellipses indicate the angle of the injected squeezing at the corresponding frequencies, where the phase quadrature is in the x-axis. At high frequencies the squeezed state is squeezed in the phase quadrature, whilst at lower frequencies the squeezing rotates and eventually aligns in the amplitude quadrature. With such a frequency dependent state, the quantum noise can be reduced at all frequencies.

Finally, now that ideal squeezing magnitudes have been achieved, and as the stability and noise couplings are better understood, the next logical step is the production of frequency dependent squeezing. In this work, the squeezing was uniform across all frequencies and as such, decreasing the shot noise at high frequencies also increases the radiation pressure at low frequencies. Currently, radiation pressure noise is not the limiting noise source at low frequencies and as such increasing its magnitude by introducing phase squeezing has little effect. In the next generation of detectors. however, the radiation pressure noise is expected to be the dominant noise source below many tens of Hertz. Hence, the introduction of a phase squeezed state would improve the high frequency performance, as shown in this thesis, but would also decrease the low-frequency performance of the device.

The exception to this is if frequency dependent squeezed light is utilised, as illustrated in Figure 10.1. Such a state would exhibit amplitude squeezing below some frequency, and would gradually rotate to phase squeezing at higher frequencies. It seems as though this is the next big challenge facing squeezing for gravitational wave detection. It has been shown that filter cavities can rotate the squeezing in the necessary way, but that this will require very large cavities [51]. It needs to either be shown that this technique is practical or another method for rotating the squeezing needs to be developed. A new technique will require a system that can provide dispersion at very low frequencies without introducing substantial loss, and very few, if any, systems currently exist with both of these properties. However, with the squeezing magnitude problem solved, the stability currently being worked on, and the noise coupling currently under investigation from the H1 squeezing experiment and also at GEO600, effort now needs to be directed towards producing these frequency dependent states.

Appendix 1

We begin at Equations 5.39

$$\begin{aligned} i\omega\delta\check{X}_1 &= -\kappa_1\delta\check{X}_1 + g\alpha_1\delta\check{X}_3 + g\alpha_3\delta\check{X}_1^\dagger + \sqrt{2\kappa_1^{in}}\delta\check{X}_1^{dr} + \sqrt{2\kappa_1^{out}}\delta\check{X}_1^{vout} + \sqrt{2\kappa_1^{l}}\delta\check{X}_1^{vl} \\ i\omega\delta\check{X}_3 &= -\kappa_3\delta\check{X}_3 - g\alpha_1\delta\check{X}_1 + \sqrt{2\kappa_3^{in}}\delta\check{X}_3^{dr} + \sqrt{2\kappa_3^{out}}\delta\check{X}_3^{vout} + \sqrt{2\kappa_3^{l}}\delta\check{X}_3^{vl}. \qquad (10.1) \end{aligned}$$

We solve this set of equations by first rearranging these equations into matrix form

$$\begin{aligned} \begin{pmatrix} \delta\check{X}_1^{dr} \\ \delta\check{X}_3^{dr} \end{pmatrix} &= \begin{pmatrix} \frac{i\omega+\kappa_1-g\alpha_3}{\sqrt{2\kappa_1^{in}}} & \frac{-g\alpha_1}{\sqrt{2\kappa_1^{in}}} \\ \frac{g\alpha_1}{\sqrt{2\kappa_1^{in}}} & \frac{i\omega+\kappa_3}{\sqrt{2\kappa_3^{in}}} \end{pmatrix} \begin{pmatrix} \delta\check{X}_1 \\ \delta\check{X}_3 \end{pmatrix} + \\ & \begin{pmatrix} -\frac{\sqrt{2\kappa_1^{out}}}{\sqrt{2\kappa_1^{in}}}\,\delta\check{X}_1^{vout} - \frac{\sqrt{2\kappa_1^{l}}}{\sqrt{2\kappa_1^{in}}}\,\delta\check{X}_1^{vl} \\ -\frac{\sqrt{2\kappa_3^{out}}}{\sqrt{2\kappa_3^{in}}}\,\delta\check{X}_3^{vout} - \frac{\sqrt{2\kappa_3^{l}}}{\sqrt{2\kappa_3^{in}}}\,\delta\check{X}_3^{vl} \end{pmatrix}. \qquad (10.2) \end{aligned}$$

The next step is to solve for the intra-cavity fields, resulting in

$$\begin{aligned} \begin{pmatrix} \delta\check{X}_1 \\ \delta\check{X}_3 \end{pmatrix} &= \begin{pmatrix} \frac{\sqrt{2\kappa_1^{in}}(\kappa_3+i\omega)}{\alpha_1\alpha_1 g^2-(g\alpha_3-\kappa_1-i\omega)(\kappa_3+i\omega)} & \frac{\sqrt{2\kappa_3^{in}}\,g\alpha_1}{\alpha_1\alpha_1 g^2-(g\alpha_3-\kappa_1-i\omega)(\kappa_3+i\omega)} \\ -\frac{\sqrt{2\kappa_1^{in}}\,g\alpha_1}{\alpha_1\alpha_1 g^2-(g\alpha_3-\kappa_1-i\omega)(\kappa_3+i\omega)} & \frac{\sqrt{2\kappa_3^{in}}(g\alpha_3-\kappa_1-i\omega)}{-\alpha_1\alpha_1 g^2+(g\alpha_3-\kappa_1-i\omega)(\kappa_3+i\omega)} \end{pmatrix}. \\ & \begin{pmatrix} \delta\check{X}_1^{dr} + \frac{\sqrt{2\kappa_1^{out}}}{\sqrt{2\kappa_1^{in}}}\,\delta\check{X}_1^{vout} + \frac{\sqrt{2\kappa_1^{l}}}{\sqrt{2\kappa_1^{in}}}\,\delta\check{X}_1^{vl} \\ \delta\check{X}_3^{dr} + \frac{\sqrt{2\kappa_3^{out}}}{\sqrt{2\kappa_3^{in}}}\,\delta\check{X}_3^{vout} - \frac{\sqrt{2\kappa_3^{l}}}{\sqrt{2\kappa_3^{in}}}\,\delta\check{X}_3^{vl} \end{pmatrix}. \qquad (10.3) \end{aligned}$$

We now have a solution for the intra-cavity fields, allowing us to determine the output fields using the input/output relations from Equation 5.9, which are rewritten as

$$\delta\check{X}^{ref} = \sqrt{2\kappa^{in}}\,\delta\check{X} - \delta\check{X}^{dr} \qquad (10.4)$$

$$\delta\check{X}^{trans} = \sqrt{2\kappa^{out}}\,\delta\check{X} - \delta\check{X}^{vout}. \qquad (10.5)$$

At this point we no longer need to investigate the properties of the pump field and so we will only calculate the output field properties of the squeezed field, resulting in

$$\begin{aligned} \delta\check{X}_1^{out} &= \begin{pmatrix} \frac{2\sqrt{\kappa_1^{in}\kappa_1^{out}}(\kappa_3+i\omega)}{\alpha_1\alpha_1 g^2-(g\alpha_3-\kappa_1-i\omega)(\kappa_3+i\omega)} \\ \frac{2\sqrt{\kappa_3^{in}\kappa_1^{out}}\,g\alpha_1}{\alpha_1\alpha_1 g^2-(g\alpha_3-\kappa_1-i\omega)(\kappa_3+i\omega)} \end{pmatrix}. \\ & \begin{pmatrix} \delta\check{X}_1^{dr} + \left(\frac{\sqrt{2\kappa_1^{out}}}{\sqrt{2\kappa_1^{in}}} - (\alpha_1\alpha_1 g^2 - (g\alpha_3 - \kappa_1 - i\omega)(\kappa_3 + i\omega))\right)\delta\check{X}_1^{vout} + K \\ \delta\check{X}_3^{dr} + \frac{\sqrt{2\kappa_3^{out}}}{\sqrt{2\kappa_3^{in}}}\,\delta\check{X}_3^{vout} - \frac{\sqrt{2\kappa_3^{l}}}{\sqrt{2\kappa_3^{in}}}\,\delta\check{X}_3^{vl} \end{pmatrix}, \end{aligned}$$

where K is given by K $= \frac{\sqrt{2\kappa_1^{l}}}{\sqrt{2\kappa_1^{in}}}\,\delta\check{X}_1^{vl}$.

At this point, these equations can be used to investigate how noise from the two driving fields, the pump and seed fields, couples into the output squeezed state. Up until now, the coherent amplitude of the seed field has not been removed in order to illustrate a point. From Equation 10.6 we see that the two elements in the first matrix can be regarded as coupling constants for the elements in the second matrix. Of note is that the first element of the second matrix consists entirely of noise terms from the seed field, and the second element of this matrix consists entirely of noise terms from the pump field. One can write

$$\delta\check{X}_1^{out} = \begin{pmatrix} C1 & \alpha_1 C2 \end{pmatrix} . \begin{pmatrix} \delta 1 \\ \delta 3 \end{pmatrix},$$

where;

$$\begin{aligned}
C1 &= \frac{2\sqrt{\kappa_1^{in}\kappa_1^{out}}(\kappa_3 + i\omega)}{\alpha_1\alpha_1 g^2 - (g\alpha_3 - \kappa_1 - i\omega)(\kappa_3 + i\omega)}, \\
C2 &= \frac{2\sqrt{\kappa_3^{in}\kappa_1^{out}}\, g}{\alpha_1\alpha_1 g^2 - (g\alpha_3 - \kappa_1 - i\omega)(\kappa_3 + i\omega)}, \\
\delta 1 &= \delta\check{X}_1^{dr} + \left(\frac{\sqrt{2\kappa_1^{out}}}{\sqrt{2\kappa_1^{in}}} - (\alpha_1\alpha_1 g^2 - (g\alpha_3 - \kappa_1 - i\omega)(\kappa_3 + i\omega)) \right) \delta\check{X}_1^{vout} + K, \\
\delta 2 &= \delta\check{X}_3^{dr} + \frac{\sqrt{2\kappa_3^{out}}}{\sqrt{2\kappa_3^{in}}}\delta\check{X}_3^{vout} - \frac{\sqrt{2\kappa_3^{l}}}{\sqrt{2\kappa_3^{in}}}\delta\check{X}_3^{vl}.
\end{aligned}$$

$C1$ can be considered as the coupling constant for the sum of all noise terms originating from fields at the fundamental frequency, $\delta 1$, and in much the same way, $C2$ can be considered as the coupling constant for all noise terms at the pump frequency $\delta 3$. The explicit dependence of the coupling of the noise terms at the pump frequency on α_1 has been highlighted. It becomes clear that the noise of the pump field is completely decoupled from the noise of the output squeezed field when the seed field has no coherent amplitude, as in the case of the OPO. It was this insight that led to the first measurements of squeezing in the audio band [63]. The details of this noise coupling are discussed in detail by McKenzie [108].

The final step is to calculate the spectrum of the amplitude quadrature noise operator. Using Equation 3.7 we can write for the variance of the output field at the fundamental frequency, V_1^{out},

$$V_1^{out} =< \delta\check{X}_1^{out\dagger}\delta\check{X}_1^{out} > . \tag{10.6}$$

This is simple to calculate due to the fact that the average of the first order noise terms is zero. Due to this fact, the average of the multiplication of uncorrelated noise terms will also result in an answer of zero. Also, the variances of all of the vacuum terms are replaced with their value of unity. At this point the coherent amplitude of the seed field is set to zero. This results in a variance for the amplitude quadrature of the squeezed field of

$$V_{out}^{+} = 1 + \frac{4g\kappa_1^{out}\alpha_3}{(\kappa_1 - g\alpha_3)^2 + \omega^2},$$

where the the subscript 1 has been dropped because it is clear that the equation is for the variance of the squeezed field. The superscript has been reintroduced to specify that this equation is for the amplitude quadrature variance. The result shown in Equation 10.7 is equivalent to the solution found for the case of an OPA under the assumption that the pump field can be treated classically (see [83]). This is because, as we have just shown, the noise from the pump field does not couple to the output state in the absence of a bright seed field. The fact that noise does not couple from this field means that we can treat it classically to simplify the situation.

The phase quadrature variance can be calculated by following the same methods presented here. However, it is possible to derive the phase quadrature variance from the variance of the amplitude quadrature. It can be shown that in the case of the OPA, where a bright seed is present, phase squeezing corresponds to amplification of the seed field, and amplitude squeezing corresponds to de-amplification of the seed field. The system can be moved from amplification to de-amplification by rotating the phase of the pump field by 180 degrees. This is equivalent to changing the sign of all the terms containing the coherent amplitude of the pump field, resulting in a variance for the phase quadrature of

$$V_{out}^{-} \quad = \quad 1 - \frac{4g\kappa_1^{out}\alpha_3}{(\kappa_1 + g\alpha_3)^2 + \omega^2}.$$

Bibliography

[1] T. H. Maiman. Stimulated optical radiation in ruby masers. *Nature*, 187:493, 1960.

[2] D. F. Welch. A brief history of high-power semiconductor lasers. *IEEE J. Sel. Topics Quantum Electron.*, 6:1470, 2000.

[3] J. L. E. Dreyer. *The Scientific Papers of Sir William Herschel, Volume 1.* Thoemmes Continuum, Bristol, 2003.

[4] R. A. Ong. Very high-energy gamma-ray astronomy. *Phys. Rep.*, 305:93, 1998.

[5] A. R. Thompson, J. M. Moran, and G. W. Swenson. *Interferometry and synthesis in radio astronomy.* Wiley-Interscience, New York, 1986.

[6] A. Einstein. *Ann. Phys. Lpz*, 49:769, 1916.

[7] A. Einstein. *Preuss. Akad. Wiss. Berlin*, page 688, 1916.

[8] The LIGO Scientific Collaboration and the Virgo Collaboration. An upper limit on the stochastic gravitational-wave background of cosmological origin. *Nature*, 460:990, 2009.

[9] B. S. Sathyaprakash and B. F. Schutz. Physics, astrophysics and cosmology with gravitational waves. *Living Reviews in Relativity*, 12, 2009.

[10] B. C. Barish and R. Weiss. LIGO and the detection of gravitational waves. *Phys. Today*, 52:44, 1999.

[11] B. P. Abbott et al. Searches for gravitational waves from known pulsars with science run 5 LIGO data. *Astrophys. J.*, 713:671, 2010.

[12] J. Abadie et al. All-sky search for gravitational-wave bursts in the first joint LIGO-GEO-Virgo run. *Phys. Rev. D*, 81:102001, 2010.

[13] J. Abadie et al. Search for gravitational waves from compact binary coalescence in LIGO and Virgo data from S5 and VSR1. *Phys. Rev. D*, 82:102001, 2010.

[14] R. A. Hulse and J. H. Taylor. Discovery of a pulsar in a binary system. *Astrophys. J. (Letters)*, 195:L51, 1975.

[15] A. Einstein and N. Rosen. *J. Franklin Inst.*, 223:43, 1937.

[16] J. Weber. Detection and generation of graviational waves. *Phys. Rev.*, 117:306, 1960.

[17] A. Giazatto. Interferometric detection of gravitational waves. *Phys. Rep.*, 182:365, 1989.

[18] http://www.auriga.lnl.infn.it.

[19] J. Weber. Evidence for discovery of gravitational radiation. *Phys. Rev. Lett.*, 22:1320, 1969.

[20] K. S. Thorne. Gravitational-wave research: Current status and future prospects. *Rev. Mod. Phys.*, 52:285, 1980.

[21] A. de Waard, L. Gottardi, J. van Houwelingen, A. Shumack, and G. Frosatti. Minigrail, the first spherical detector. *Class. Quantum Grav.*, 20:143, 2003.

[22] M. Bartusiak. *Einstein's Unfinished Symphony: Listening to the Sounds of Space-Time.* Joseph Henry Press, Washington DC, 2000.

[23] A. Abramovici, W. E. Althouse, R. W. P. Drever, Y. Gursel, S. Kawamura, F. J. Raab, D. Shoemaker, L. Sievers, R. E. Spero, K. S. Thorne, R. E. Vogt, R. Weiss, S. E. Whitcomb, and M. E. Zucker. LIGO: the laser interferometer gravitational-wave observatory. *Science*, 256:325, 1992.

[24] W. A. Edelstein, J. Hough, J. R. Pugh, and W. Martin. Limits to the measurement of displacement in an interferometric gravitational radiation detector. *J. Phys. E: Sci. Instrum.*, 11:710, 1978.

[25] C. M. Caves. Quantum-mechanical noise in an interferometer. *Phys. Rev. D.*, 23:1693, 1981.

[26] P. F. Michelson. On detecting stochastic background gravitational radiation with terrestrial detectors. *Mon. Not. R. astr. Soc.*, 227:933, 1987.

[27] S. Rowan and J. Hough. Gravitational wave detection by interferometry (ground and space). *Living Reviews in Relativity*, 3, 2000.

[28] J. R. Smith for the LIGO Scientific Collaboration. The path to the enhanced and advanced LIGO gravitational-wave detectors. *Class. Quantum Grav.*, 26:114013, 2009.

[29] G. M. Harry for the LIGO Scientific Collaboration. Advanced LIGO: the next generation of gravitational wave detectors. *Class. Quantum Grav.*, 27:084006, 2010.

[30] B. F. Schutz. Gravitational-wave sources. *Class. Quantum Grav.*, 13:A219, 1996.

[31] B. P. Abbott et al. Search for gravitational waves from low mass binary coalescences in the first year of LIGO's S5 data. *Phys. Rev. D*, 79:122001, 2009.

[32] F. Acernese et al. The VIRGO interferometric gravitational antenna. *Opt. Lasers Eng.*, 45:478, 2007.

[33] B. Willke *et al.* The GEO 600 gravitational wave detector. *Class. Quantum Grav.*, 19:1377, 2002.

[34] C. M. Caves. Quantum limits on noise in linear amplifiers. *Phys. Rev. D*, 26:1817, 1982.

[35] A. M. Gretarsson, G. M. Harry, S. D. Penn, P. R. Saulson, W. J. Startin, S. Rowan, G. Cagnoli, and J. Hough. Pendulum mode thermal noise in advanced interferometers: a comparison of fused silica fibers and ribbons in the presence of surface loss. *Phys. Lett. A*, 270:108, 2000.

[36] Y. Levin. Internal thermal noise in the ligo test masses: A direct approach. *Phys. Rev. D*, 57:659, 1998.

[37] G. M. Harry, A. M. Gretarsson, P. R. Saulson, S. E. Kittelberger, S. D. Penn, W. J. Startin, S. Rowan, M. M. Fejer, D. R. M. Crooks, G. Cagnoli, J. Hough, and N. Nakagawa. Thermal noise in interferometric gravitational wave detectors due to dielectric coatings. *Class. Quantum Grav.*, 19:897, 2002.

[38] G. M. Harry, H. Armandula, E. Black, D. R. M. Crooks, G. Cagnoli, J. Hough, P. Murray, S. Reid, S. Rowan, P. Sneddon, M. M. Fejer, R. Route, and S. D. Penn. Thermal noise from optical coatings in gravitational wave detectors. *Appl. Opt.*, 45:1569, 2006.

[39] H. B. Callen and R. F. Greene. On a theorem of irreversible thermodynamics. *Phys. Rev.*, 86:702, 1952.

[40] K. Kuroda. Status of LCGT. *Class. Quantum Grav.*, 27:084004, 2010.

[41] K. Somiya. Detector configuration of KAGRA - the Japanese cyrogenic graviatational-wave detector. *arXiv:gr-qc/1111.7185v2*, 2012.

[42] S. Miyoki *et al.* Status of the CLIO project. *Class. Quantum Grav.*, 21:S1173, 2004.

[43] P. Fritschel. Second generation instruments for the laser interferometer gravitational wave observatory (LIGO). *arXiv:gr-qc/0308090v1*, 2003.

[44] M. G. Beker, G. Cella, R. DeSalvo, M. Doets, H. Grote, J. Harms, E. Hennes, V. Mandic, D. S. Rabeling, J. F. J. van den Brand, and C. M. van Leeuwen. Improving the sensitivity of future GW observatories in the 1-10 Hz band: Newtonian and seismic noise. 43:623, 2011.

[45] R. Abbott, R. Adhikari, G. Allen, S. Cowley, E. Daw, D. Debra, J. Giaime, G. Hammond, M. Hammond, C. Hardham, J. How, W. Hua, W. Johnson, B. Lantz, K. Mason, R. Mittleman, J. Nichol, S. Richman, J. Rollins, D. Shoemaker, G. Stapfer, and R. Stebbins. Seismic isolation for Advanced LIGO. *Class. Quantum Grav.*, 19:1591, 2002.

[46] S. Sato, S. Miyoki, S. Telada, D. Tatsumi, A. Araya, M. Ohashi, Y. Totsuka, M. Fukushima, and M. Fujimoto. Ultrastable performance of an underground-based laser interferometer observatory for gravitational waves. *Class. Quantum Grav.*, 60:102005, 2004.

[47] P. Amaro-Seone *et al.* Low-frequency gravitational-wave science with eLISA/NGO. *arXiv:gr-qc/1202.0839.v1*, 2012.

[48] F. Antonucci *et al.* LISA pathfinder: mission and status. *Class. Quantum Grav.*, 2008:094001, 2011.

[49] T. Corbitt and N. Mavalavala. Quantum noise in gravitational-wave interferometers. *J. Opt. B: Quantum Semiclass. Opt.*, 6, 2004.

[50] R. Lawrence, D. Ottaway, M. Zucker, and P. Fritschel. Active correction of thermal lensing through external radiative thermal actuation. *Opt. Lett.*, 29:2635, 2004.

[51] S. Chelkowski, H. Vahlbruch, B. Hage, A. Franzen, N. Lastzka, K. Danzmann, and R. Schnabel. Experimental characterization of frequency-dependent squeezed light. *Phys. Rev. A*, 71:013806, 2007.

[52] V. B. Braginsky, S. E. Strigin, and S. P. Vyatchanin. Parametric oscillatory instability in Fabry-Perot interferometer. *Phys. Lett. A*, 287:331, 2001.

[53] S. Ballmer, V. Frolov, R. Lawrence, W. Kells, G. Moreno, K. Mason, D. Ottaway, M. Smith, C. Vorvick, P. Willems, and M. Zucker. Thermal compensation system description. *Open access LIGO document LIGO-T050064-00-R*, 2005.

[54] R. Lawrence, M. Zucker, P. Fritschel, P. Marfuta, and D. Shoemaker. Adaptive thermal compensation of test masses in advanced ligo. *Class. Quantum Grav.*, 19:1803, 2002.

[55] N. Treps, U. Andersen, B. Buchler, P. K. Lam, A. Maître, H. A. Bachor, and C. Fabre. Surpassing the standard quantum limit for optical imaging using nonclassical multimode light. *Phys. Rev. Lett*, 88, 2004.

[56] E. S. Polzik, J. C. Carri, and H. J. Kimble. Spectroscopy with squeezed light. *Phys. Rev. Lett.*, 68:3020, 1992.

[57] R. E. Slusher, L. W. Hollberg, B. Yurke, J. C. Mertz, and J. F. Valley. Observation of squeezed states generated by four-wave mixing in an optical cavity. *Phys. Rev. Lett.*, 55:2409, 1985.

[58] H. J. Kimble. Squeezed states of light: an (incomplete) survey of experimental progress and prospects. *Phys. Rep.*, 219:227, 1992.

[59] K. McKenzie, D. A. Shaddock, D. E. McClelland, B. C. Buchler, and P. K. Lam. Experimental demonstration of a squeezing-enhanced power-recycled michelson interferometer for gravitational wave detection. *Phys. Rev. Lett.*, 88:231102, 2002.

[60] K. Goda. *Development of Techniques for Quantum-Enhanced Laser-Interferometric Gravitational-Wave Detectors.* PhD thesis, Massachusetts Institute of Technology, Cambridge, 2007.

[61] K. Goda, K. McKenzie, E. E. Mikhailov, P. K. Lam, D.E. McClelland, and N. Mavalvala. Photothermal fluctuations as a fundamental limit to low-frequency squeezing in a degenerate optial parametric oscillator. *Phys. Rev. A*, 72:043819, 2005.

[62] W. P. Bowen, R. Schnabel, N. Treps, H-A. Bachor, and P. K. Lam. Recovery of continuous wave squeezing at low frequencies. *J. Opt. B: Quantum Semiclass. Opt.*, 4:421, 1992.

[63] K. McKenzie, N. Grosse, W. P. Bowen, S. E. Whitcomb, M. B. Gray, D. E. McClelland, and P. K. Lam. Squeezing in the audio gravitational-wave detection band. *Phys. Rev. Lett.*, 93:161105, 2004.

[64] K. McKenzie, M. B. Gray, P. K. Lam, and D. E. McClelland. Technical limitations to homodyne detection at audio frequencies. *Appl. Optics*, 46:3389, 2007.

[65] S. Chua, K. McKenzie, B.C. Buchler, and D.E. McClelland. Impact of non-stationary events on low frequency homodyne detection. *Journ. Phys.: Conf. Ser.*, 122:012023, 2008.

[66] H. Vahlbruch, S. Chelkowski, B. Hage, A. Franzen, K. Danzmann, and R. Schnabel. Coherent control of vacuum squeezing in the gravitational-wave detection band. *Phys. Rev. Lett.*, 97:011101, 2006.

[67] S. Chelkowski, H. Vahlbruch, K. Danzmann, and R. Schnabel. Coherent control of broadband vacuum squeezing. *Phys. Rev. A*, 75:043814, 2007.

[68] The LIGO Scientific Collaboration. A gravitational wave observatory operating beyond the quantum shot-noise limit. *Nat. Phys.*, 2083, 2011.

[69] M. Xiao, L.-A. Wu, and H. J. Kimble. Precision measurement beyond the shot-noise limit. *Phys. Rev. Lett.*, 59:279, 1987.

[70] K. Goda, O. Miyakawa, E. E. Mikhailov, S. Saraf, R. Adhikari, K. McKenzie, R. Ward, S. Vass, A. J. Weinstein, and N. Mavalvala. A quantum-enhanced prototype gravitational-wave detector. *Nat. Phys.*, 4:472, 2008.

[71] N. Christensen. LIGO S6 detector characterization studies. *Class. Quantum Grav.*, 27:194010, 2010.

[72] F. Acernese *et al.* Virgo status. *Class. Quantum Grav.*, 25:184001, 2008.

[73] D. F. Walls and G. J. Milburn. *Quantum Optics.* Springer-Verlag, Berlin, 1994.

[74] H. R. Lewis Jr. Classical and quantums systems with time-dependent harmonic-oscillator-type hamiltonians. *Phys. Rev. Lett.*, 18:510, 1967.

[75] E. Hecht. *Optics.* Addison-Wesley, Reading, 2 edition, 1987.

[76] H.-A. Bachor. *"A guide to experiments in quantum optics".* VCH Publishers, New York, 1998.

[77] T. Kane. Intensity noise in diode-pumped single-frequency Nd:YAG lasers and its control by electronic feedback. *IEEE Photon. Technol. Lett.*, 2:244, 1990.

[78] G. Jaeger. *Quantum Information: An Overview.* Springer, New York, 2006.

[79] C. Silberhorn, P. K. Lam, O. Weiß, F. König, N. Korolkova, and G. Leuchs. Generation of continuous variable Einstein-Podolsky-Rosen entanglement via the kerr nonlinearity in an optical fiber. *Phys. Rev. Lett.*

[80] N. B. Grosse, S. Assad, M. Mehmet, R. Schnabel, T. Symul, and P. K. Lam. Observation of entanglement between two light beams spanning an octave in optical frequency. *Phys. Rev. Lett.*, 100:243601, 2008.

[81] W. P. Bowen, R. Schnabel, P. K. Lam, and T. C. Ralph. Experimental investigation of criteria for continuous variable entanglement. *Phys. Rev. Lett.*, 90:043601, 2003.

[82] M. J. Collett, R. Loudon, and C. W. Gardiner. Quantum theory of optical homodyne and heterodyne detection. *J. Mod. Optic.*, 34:881, 1987.

[83] B.E. Buchler. *Electro-optic control of quantum measurements.* PhD thesis, The Australian National University, 2001.

[84] C. F. McCormick, V. Boyer, E. Arimondo, and P. D. Lett. Strong relative intensity squeezing by four-wave mixing in rubidium vapor. *Opt. Lett.*, 32:178, 2007.

[85] R. M. Shelby, M. D. Levenson, S. H. Perlmutter, R. G. DeVoe, and D. F. Walls. Broad-band parametric deamplification of quantum noise in an optical fiber. *Phys. Rev. L.*, 57:692, 1986.

[86] T. Eberle, S. Steinlechner, J. Bauchrowitz, V. Händchen, H. Vahlbruch, M. Mehmet, H. Müller-Ebhardt, and R. Schnabel. Quantum enhancement of the zero-area sagnac interferometer topology for gravitational wave detection. *Phys. Rev. Lett.*, 104:251102, 2010.

[87] M. S. Stefszky, C. M. Mow-Lowry, S. S. Y. Chua, D. A. Shaddock, B. C. Buchler, H. Vahlbruch, A. Khalaidovski, R. Schnabel, P. K. Lam, and D. E. McClelland. Balanced homodyne detection of optical quantum states at audio-band frequenices and below. *Class. Quantum Grav. (submitted)*, 2012.

[88] C. F. McCorick, A. M. Marino, V. Boyer, and P. D. Lett. Strong low-frequency quantum correlations from a four wave-mixing amplifier. *Phys. Rev. A*, 78:043816, 2008.

[89] C. Liu, J. Jing, Z. Zhou, R. C. Pooser, F. Hudelist, L. Zhou, and W. Zhang. Realization of low frequency and controllable bandwidth squeezing based on a four-wave-mixing amplifier in rubidium vapor. *Opt. Lett.*, 36:2979, 2011.

[90] L.-A. Wu, H. J. Kimble, J. L. Hall, and H. Wu. Generation of squeezed states by parametric down conversion. *Phys. Rev. Lett.*, 57:2520, 1986.

[91] E. S. Polzik, J. Carri, and H. J. Kimble. Atomic spectroscopy with squeezed light for sensitivity beyond the vacuum-state limit. *Appl. Phys. B*, 55:279, 1992.

[92] Z. Y. Ou, S. F. Pereira, H. J. Kimble, and K. C. Peng. Realization of the einstein-podolsky-rosen paradox for continuous variables. *Phys. Rev. Letts.*, 68:3663, 1992.

[93] K. Schneider, R. Bruckmeier, H. Hansen, S. Schiller, and J. Mlynek. Bright squeezed-light generation by a continuous-wave semimonolithic parametric amplifier. *Opt. Lett.*, 21:1396, 1996.

[94] K. Schneider, M. Lang, J. Mlynek, and S. Schiller. Generation of strongly squeezed continuous-wave light at 1064 nm. *Opt. Ex.*, 2:59, 1998.

[95] P. K. Lam, T. C. Ralph, B. C. Buchler, D. E. McClelland, H.-A. Bachor, and J. Gao. Optimization and transfer of vacuum squeezing from an optical parametric oscillator. *J. Opt. B*, 1:469, 1999.

[96] S. Suzuki, H. Yonezawa, F. Kannari, M. Sasaki, and A. Furusawa. 7db quadrature squeezing at 860 nm with periodically poled KTiOPO$_4$. *Appl. Phys. Lett.*, 89:061116, 2006.

[97] Y. Takeno, M. Yukawa, H. Yonezawa, and A. Furusawa. Observation of -9 db quadrature squeezing with improvement of phase stability in homodyne measurement. *Opt. Exp.*, 15:4321, 2007.

[98] H. Vahlbruch, S. Chelkowski M. Mehmet, B. Hage, A. Franzn, N. Lastzka, S. Goßler, K. Danzmann, and R. Schnabel. Observation of squeezed light with 10-dB quantum-noise reduction. *Phsy. Rev. Lett.*, 100:033602, 2008.

[99] M. Mehmet, H. Vahlbruch, N. Lastzka, K. Danzmann, and R. Schnabel. Observation of squeezed states with strong photon-number oscillations. *Phys. Rev. A*, 81:013814, 2010.

[100] A. Khalaidovski, H. Vahlbruch, N. Lastzka, C. Gräf, H. Lück, K. Danzmann, H. Grote, and R. Schnabel. Status of the GEO 600 squeezed-light source. *arXiv:quant-ph/1112.0198v1*, 2011.

[101] M. Mehmet, S. Ast, T. Eberle, S. Steinlechner, H. Vahlbruch, and R. Schnabel. Squeezed light at 1550nm with a quantum noise reduction of 12.3 dB. *Opt. Exp.*, 19:25763, 2011.

[102] S.S.Y. Chua, M.S. Stefszky, C.M. Mow-Lowry, B.C. Buchler, S. Dwyer, D.A. Shaddock, P.K. Lam, and D.E. McClelland. Backscatter tolerant squeezed light source for advanced gravitational-wave detectors. *Opt. Lett.*, 36:4680, 2011.

[103] R. W. Boyd. *Nonlinear Optics.* Academic Press, Orlando, 2003.

[104] P. A. Franken, A. E. Hill, C. W. Peters, and G. Weinreich. Generation of optical harmonics. *Phys. Rev. Lett.*, 7:118, 1961.

[105] M. D. Reid. Demonstration of the Einstein-Podolsky-Rosen paradox using nondegenerate parametric amplification. *Phys. Rev. A*, 40:913, 1989.

[106] A. S. Villar, L. S. Cruz, K. N. Cassemiro, M. Martinelli, and P. Nussenzveig. Generation of bright two-color continuous variable entanglement. *Phys. Rev. Lett*, 95:243603, 2005.

[107] R.S. Klein, G.E. Kugel, A. Maillard, K. Polgár, and A. Péter. Absolute non-linear optical coefficients of $LiNbO_3$ for near stoichiometric crystal compositions.

[108] K. McKenzie. *Squeezing in the Audio Gravitational Wave Detection Band.* PhD thesis, Physics Department, Australian National University, Canberra, Australia, 2008.

[109] S. Wang. *Fabrication and characterization of periodcially-poled KTP and Rb-doped KTP for applications in the visible and UV.* PhD thesis, Laser Physics Division, Department of Physics, Royal Institute of Technology, Stockholm, Sweden, 2005.

[110] P. D. Drummond, K. J. McNeil, and D. F. Walls. Non-equilibrium transitions in sub/second harmonic generation I. semiclassical theory. *Optica Acta*, 27:321, 1980.

[111] C. W. Gardiner and M. J. Collett. Input and output in damped quantum systems: Quantum stochastic differential equations and the master equation. *Phys. Rev. A*, 31:3761, 1985.

[112] A. G. White. *Classical and quantum dynamics of optical frequency conversion.* PhD thesis, Physics Department, Australian National University, Canberra, Australia, 1995.

[113] M. J. Collett and C. W. Gardiner. Squeezing of intracavity and travelling-wave light fields produced in parametric amplification. *Phys. Rev. A*, 30:1386, 1984.

[114] A. E. Siegman. *Lasers.* University Science Books, Mill Valley, California, 1986.

[115] A. Yariv. *Quantum Electronics.* John Wiley & Sons., Singapore, 3 edition, 1989.

[116] N. B. Grosse. *Harmonic Entanglement & Photon Anti-Bunching.* PhD thesis, Physics Department, Australian National University, Canberra, Australia, 2009.

[117] R. Blachman, P. F. Bordui, and M. M. Fejer. Laser-induced photochromic damage in potassim titanyl phosphate. *Appl. Phys. Lett.*, 64:1318, 1994.

[118] J. C. Jacco, D. R. Rockafellow, and E. A. Teppo. Bulk-darkening threshold of flux-grown $KTiOPO_4$. *Opt. Lett.*, 16:1307, 1991.

[119] J. K. Tyminski. Photorefractive damage in KTP used as second-harmonic generator. *J. Appl. Phys.*, 70:5570, 1991.

[120] H. Vahlbruch, A. Khalaidovski, N. Lastzka, C. Gräf, K. Danzmann, and R. Schnabel. The GEO 600 squeezed light source. *Class. Quantum Grav.*, 27:084027, 2010.

[121] G. D. Boyd and D. A. Kleinman. Parametric interaction of focussed gaussian light beams. *J. Appl. Phys.*, 39:3597, 1968.

[122] I. Shoji, T. Kondo, A. Kitamoto, M. Shirane, and R. Ito. Absolute scale of seond-order nonlinear-optical coefficients. *J. Opt. Soc. Am. B*, 14:2268, 1997.

[123] R. C. Eckardt, C. D. Nabors, W. J. Kozlovsky, and R. L. Byer. Optical parametric oscillator frequency tuning and control. *J. Opt. Soc. Am. B*, 8:646, 1991.

[124] S. Pearl, H. Lotem, and Y. Shimony. Optimization of laser intracavity second-harmonic generation by a linear dispersion element. *J. Opt. Soc. Am. B*, 16:1705, 1999.

[125] A.L. Alexandrovski, M.M. Fejer, R.P. Route, and R.L. Byer. UV and visible absorption in $LiTaO_3$. In *SPIE Conference on Laser Material Crystal Growth and Nonlinear Materials and Devices (SPIE 1999)*, 1999.

[126] L. E. Myers, R. C. Eckardt, M. M. Fejer, and R. L. Byer. Quasi-phase-matched optical parametric oscillators in bulk periodically poled $MgO{:}LINbO_3$. *J. Opt. Soc. Am.*, 12:2102, 1995.

[127] Y. Furukawa, K. Kitamura, A. Alexandrovski, R. K. Route, M. M. Fejer, and G. Foulon. Green-induced infrared absorption in MgO doped $LiNbO_3$. *Appl. Phys. Lett.*, 78:1970, 2001.

[128] V. Pasiskevicius, S. Wang, J. A. Tellefsen, F. Laurell, and H. Karlsson. Efficient nd:yag laser frequency doubling with periodically poled KTP. *Appl. Opt.*, 37:7116, 1998.

[129] A. L. Alexandrovski, M. M. Fejer, R. P. Route, and R. L. Byer. Photothermal absorption measurements in optical materials. In *Lasers and Electro-Optics (CLEO 2000)*, 2000.

[130] L. E. Busse, L. Goldberg, and M. R. Surette. Absorption losses in Mg-O-doped and undoped potassium niobate. *J. Appl. Phys.*, 75:1102, 1993.

[131] P. K. Lam. *Applications of quantum electro-optic control and squeezed light.* PhD thesis, Physics Department, Australian National University, Canberra, Australia, 1998.

[132] R.G. Batchko, G.D.Miller, A.L. Alexandrovski, M.M. Fejer, and R.L. Byer. Limitations of high-power visible wavelength periodically poled lithium niobate devices due to green-induced infrared absorption and thermal lensing. In *(CLEO 1998)*, 1998.

[133] N. Grosse, W.P. Bowen, K. McKenzie, and P.K. Lam. Harmonic entanglement with second-order nonlinearity. *Phys. Rev. Lett.*, 96:063601, 2006.

[134] S. Li, W. Cao, and L. E. Cross. The extrinsic nature of nonlinear behavior observed in lead zirconate titanate ferroelectric ceramic. *J. Appl. Phys.*, 69:7219, 1991.

[135] K. McKenzie, E. E. Mikhailov, K. Goda, P. K. Lam, N. Grosse, M. B. Gray, N. Mavalvala, and D. E. McClelland. Quantum noise locking. *J. Opt. B*, 7, 2005.

[136] M. D. Reid and P. D. Drummond. Quantum correlations of phase in nondegenerate parametric oscillation. *Phys. Rev. Lett*, 60:2731, 1988.

[137] G. Björk and Y. Yamamoto. Generation and amplification of number states by nondegenerate parametric oscillators with idler-measurement feedback. *Phys. Rev. A*, 37:4229, 1988.

[138] P. D. Drummon and M. D. Reid. Correlations in nondegenerate parametric oscillation. II. Below threshold results. *Phys. Rev. A*, 41:3930, 1990.

[139] D. A. Shaddock. *Advanced Interferometry for Gravitational Wave Detection.* PhD thesis, Physics Department, Australian National University, Canberra, Australia, 2000.

[140] A. Khalaidovski, H. Vahlbruch, N. Lastzka, C. Gräf, K. Danzmann, H. Grote, and R. Schnabel. Long-term stable squeezed vacuum state of light for gravitational wave detectors. *arXiv:quant-ph/1109.3731v1*, 2011.

[141] H. Vahlbruch, S. Chelkowski, K. Danzmann, and R. Schnabel. Quantum engineering of squeezed states for quantum communication and metrology. *New J. Phys.*, 9:371, 2007.

[142] R. Schnabel, N. Mavalvala, D. E. McClelland, and P.K. Lam. Quantum metrology for gravitational wave astronomy. *Nat. Commun.*, 1.

[143] H. Vahlbruch. *Squeezed Light for Gravitational Wave Astronomy.* PhD thesis, The Albert Einstein Institute and the Institute of Gravitational Physics of Leibniz Universität Hannover, Hannover, Germany, 2008.

[144] P. Horrowitz and W. Hill. *The Art of Electronics.* Cambridge University Press, Cambridge, 2 edition, 1991.

[145] F. Seifert. Resistor current noise measurments. *Open access LIGO document LIGO-T0900200-v1*, 2009.

[146] E. D. Black. An introduction to pound-drever-hall laser frequency stabilization. *Am. J. Phys.*, 69:79, 2001.

[147] P. Kwee. *Laser characterization and stabilization for precision interferometry.* PhD thesis, Gottfried Wilhelm Leibniz Universität Hannover, Germany, 2010.

[148] F. Seifert. *Power stabilization of high power lasers for second generation gravitational wave detectors.* PhD thesis, Gottfried Wilhelm Leibniz Universität Hannover, Germany, 2010.

[149] H. Lück, J. Degallaix, H. Grote, M. Hewitson, S. Hild, B. Willke, and K. Danzmann. Opto-mechanical frequency shifting of scattered light. *J. Opt. A*, 10:085004, 2008.

[150] C. N. Man, A. Brillet, and P. Cerez. Suppression of optical feedback effects on saturated absorption signals by phase modulation of the reflected light. *J. Phys. E: Sci. Instrum.*, page 19, 1978.

[151] R. Schilling, L. Schnupp, W. Winkler, H. Billing, K. Maischberger, and A. Rüdiger. A method to blot out scattered light effects and its application to a gravitational wave detector. *J. Phys. E: Sci. Instrum.*, 14:65, 1981.

[152] G. A. Cranch, A. Dandridge, and C. K. Kirkendall. Suppression of double rayleigh scattering-induced excess noise in remotely interrogated fiber-optic interferometric sensors. *IEEE Photon. Technol. Lett.*, 15:1582, 2003.

[153] The LSC. Enhancement of the astrophysical reach of a gravitational wave observatory using squeezed states of light. Unpublished Manuscript.

[154] M. Frede, B. Schulz, R. Wilhelm, P. Kwee, F. Seifert, B. Willke, and D. Kracht. Fundamental mode, single-frequency laser amplifier for gravitational wave detectors. *Opt. Exp.*, 15:459, 2007.

[155] R. L. Savage Jr, P. J. King, and S. U. Seel. A highly stabilized 10-watt Nd:YAG laser for the laser interferometer gravitational-wave observatory (LIGO). *Laser Phys.*, 8:679, 1998.

[156] S. Dwyer. Summary of loss measurements for h1 squeezing test. *LIGO-T1200023-v1 (Unpublished)*, 2012.

[157] The LSC. Faraday isolator specifications for Advanced LIGO. *Open access LIGO document LIGO-T050226-00-D*, 2005.

[158] K. McKenzie, M. B. Gray, P. K. Lam, and D. E. McClelland. Nonlinear phase matching locking via optical readout. *Opt. Exp.*, 14:11256, 2005.